Ullmann dehalogenation of dibromoferrocene for the formation of surface-confined molecular rotors

Lee Ryan Atkinson

BSc (Phys)

Submitted in fulfilment of the requirements for the degree of

Master of Philosophy

School of Chemistry and Physics

Science and Engineering Faculty

Queensland University of Technology

2021

There is and always will be more to learn…

Abstract

Research into nanodevices and molecular machines has been a field of great interest and promise for many years. Molecular machines promise precisely controlled complex engineering systems on the nanoscale, like those found in biological systems. To produce these molecular machines, stable, controllable, localisable nanodevices, or "parts" need to be studied and developed first. Surface science in an Ultra-High Vacuum (UHV) provides a wide range of analysis and control techniques for studying the mechanics of localisable nanodevices.

One such potential nanodevice is a ferrocene-based nanorotor, that this work aims to produce for future use in nanoscale manipulation among other applications. This molecule was the first synthesised metallocene and consists of two cyclopentadienyl rings with an iron(II) atom sandwiched between them. The iron core has partial double covalent bonds to each carbon atom. Each aromatic ring has a rotational degree of freedom about a common axis through the iron core and can be functionalised with various moieties. These functionalisations affect surface interaction and molecular assembly allowing some level of control over the resulting structure. If the common axis of ferrocene is parallel with the adsorbing surface it is a horizontal adsorption and if the axis is perpendicular it is vertically adsorbed.

The Ullmann reaction is a well-studied method of dehalogenation and aryl-aryl coupling via metal-aided catalysis. The aim is to use the first half of the Ullmann reaction, Ullmann dehalogenation, to form ferrocene organometallic coordination complexes. The reason for this is to attain an orientation of the ferrocene moiety that maintains its rotational degree of freedom. To do this dibromoferrocene (DBF) must only dehalogenate once maintaining a distance between a halogenated ring and the surface in a vertical orientation. DBF was deposited via vapor deposition in UHV onto clean Ag(111) and Au(111) single crystal substrates.

Investigation and characterisation of the depositions was performed with in situ x-ray photoelectron spectroscopy (XPS) and scanning tunnelling microscopy (STM). Near edge x-ray adsorption fine structure (NEXAFS) was also performed on the samples at the Australian Synchrotron facility. XPS of surface deposited DBF suggested the expected dehalogenation event had occurred on Ag(111) and Au(111). 50% of bromine was dehalogenated upon deposition on Ag(111), and it was found that over a ~30 minute period the majority of the bromine moieties had undergone dehalogenation. This suggests full dehalogenation of the

ferrocene moieties and surface interaction with both aromatic rings. This was confirmed by NEXAFS, which revealed the ferrocene moiety to be horizontally oriented with both aromatic rings interacting with the surface. The STM images of this surface showed large well-ordered linear "corn row" structures of ferrocene. XPS of deposition onto Au(111) produced an initial dehalogenation of 36.5% of bromines and over time any unreacted DBF was found to desorb. NEXAFS suggested almost vertically oriented ferrocene which would further support that only a single dehalogenation even has occurred. STM images were challenging to produce and molecular resolution was not achieved. On Au(111) it is unknown exactly what structure the adsorbed DBF formed, but the upright ferrocene moiety still leaves the potential for the intended oligomerisation to have occurred.

DFT simulations of gas-phase ferrocene and dibromoferrocene were performed to investigate the rotational barrier map of ferrocene and the effect of bromine functionalisation on the barrier. The B3LYP functional was used with 3-21G and 6-31G basis sets and showed the expected mapped structure for ferrocene. However, neither basis set produced barriers in agreement with published results. The results found for DBF showed a significant difference in the mapped barrier compared to ferrocene, although the barrier did not agree with published results. DFT calculations for ferrocene on Ag(111) adsorption geometry were performed using the Born-Oppenheimer Molecular Dynamics functional and Plane-Wave basis set. The two runs, one for a vertically adsorbed molecule and one horizontally adsorbed, were energetically within 0.1 eV of each other suggesting no favourability between vertical and horizontal adsorption. This is a positive outcome for the possibility of vertically oriented ferrocene for maintaining rotational freedom.

Table of Contents

Table of Contents

List of Figures

List of Table

List of Equations

List of Abbreviations

UHV	Ultra-high vacuum
DBF	1'1-dibromoferrocene
XPS	X-ray photoelectron spectroscopy
STM	Scanning Tunnelling Microscopy
NEXAFS	Near edge x-ray adsorption fine structure
DFT	Density functional theory
JTE	Jahn–Teller effect
FCC	Face-centred cubic
HCP	Hexagonal closest packed
1D	One dimensional
k_B	Boltzmann constant
Cp	Cyclopentadienyl
3D	Three dimensional
2D	Two dimensional
FFT	Fast Fourier transform
E_K	Kinetic energy
E_B	Binding energy
XANES	X-ray absorption near edge structure
B3LYP	Becke, 3-parameter, Lee–Yang–Parr
QE	Quantum Espresso
EC	Exchange-correlation

Statement of Original Authorship

The work contained in this thesis has not been previously submitted to meet requirements for an award at this or any other higher education institution. To the best of my knowledge and belief, the thesis contains no material previously published or written by another person except where due reference is made.

Signature: QUT Verified Signature

Date: 20th of January 2021

Acknowledgements

I want to thank everyone in QUT's surface science group for supporting me throughout my research and continually pushing me to learn more. The expertise and experience of my supervisory team, Dr Jennifer MacLeod, Dr Josh Lipton-Duffin and Dr Ting Liao was invaluable. This thesis and the experience I have gained through these 18 months would not have been possible without their continued support.

I am grateful for the opportunities and guidance Dr Jennifer MacLeod had provided me with in these formative stages of my career as a researcher. She has always been vigorously interested in my work and the work of the surface science group. I would like to thank her for her eternal patience with me and all the time she put in to helping me with this thesis.

I would also like to appreciate Dr Josh Lipton-Duffin for his assistance in the lab and the guidance he has provided in lab and XPS analysis. His experience with instrumentation and the many ways they can go wrong, as well as how to manage these practical issues was great skill. I will never forget the frustration of having to trouble shoot why the vacuum was dirty or determining if a bolt was sized in imperial or metric, attempting to get the thermocouple to work, etc.

I would like to thank and acknowledge other who have supported this project outside of my supervisory team, such as lab support and training from Vishakya Jayalatharachchi, data analysis support from Steven Best, coding assistance from Alex Barnier and all the others that have helped along the way.

I would like to thank QUT and its Central Analytical Research Facility for providing the facilities and instrumentation required to perform this research project.

I would like to thank my fantastic and loving parents Shane and Susan, for their continued support throughout my education and for setting me up for the career and bright path I follow in life.

Finally, I am grateful for my partner Gabrielle Ward, for her love and support and for her fantastic self. I am excited to see where our paths lead together and enjoy the time we have.

Chapter 1: Introduction

1.1 Background

Localisable, addressable, and repeatable molecular motion of individual molecules is a foundation for larger molecular machinery[1-3]. Molecular machines are systems of nanodevices that can act on their surroundings in a way, predetermined by their design, to produce a desired nanoscopic mechanochemical result. These molecular machines could be combined to create nanoscale "factories" like those found in biological systems[4], for macro-molecular manipulation. The function of such structures could include production of precision nanoscale electronics or living structures with light activated molecular machines that can repair cracks and broken parts. While there are still many challenges to overcome there have also been huge advancements in this field over the past two decades alone[5,6]. The potential benefits of such technologies demand research into a variety of different nanodevices. The first major challenge for new molecular machinery is the formation of new robust controllable nanodevices. Nanodevices are molecules capable of mechanical motion such as molecular rotors, or mechanical work such as molecular motors[7]. Molecular machinery has been successfully produced in the past from nanodevices such as rotaxane[2], and there are surely many more to discover.

Nanodevices have previously been studied in solution and on surface with the interactions and dynamics in these two phases found to be profoundly different[8]. For practical use in surface-based applications, addressing the controllability and stability of surface bound nanodevices is required. Techniques such as Scanning Tunnelling Microscopy (STM) allow for visualisation and control of atomic level structures. However, the control they offer for their size and complexity is limited to positioning individual atoms and molecules. Molecular machines could be engineered for this purpose specifically and thus be more precise, robust, or potentially provide a more advanced method of achieving the same outcomes. Potential control methods are light or thermal activation, during which the stability of the machine on the surface during activation is a key challenge for maintaining the repeatability and control. These machines could be a step towards increasing the accessibility to the powerful field of atomic level engineering. The advancement of this novel area of research is the motivation for this research and its pursuit of nanodevices.

1.2 Context

Molecules with the ability to change in a reversible way, mechanically or chemically, are a type of nanodevice called molecular switches. Getting molecules to act mechanically, such as overcoming rotational barriers in solution, is relatively easy and can be achieved by photonic or thermal activation.[7,9,11] However, this only applies to molecules where the activation energy to internal rotation, (for example, in ferrocene, rotation of the Cp ring around the central Fe core or more generally, rotation about a bond within a molecule) is not so high that the intramolecular covalent bonds would dissociate. On surface, the challenge is to maintain mechanical freedom while also being bound to a solid. The adsorption energy between the molecule and surface must be stronger than the rotational activation energy to allow for useful internal mechanical motion while maintaining surface adsorption. This mechanical motion can be anything from conformational change[11] to chiral switching/isomerisation[7].

Molecular rotors are nanodevices that are like molecular switches except molecular rotors are devices can rotate a full 2π radians and can be reversible or unidirectional 'rachets'. For molecular rotors there are two "parts" of the molecular system, analogous to the common electric motor: the stator (the stationary part of the molecule or the substrate itself) and the rotor. For the surface confined molecule to have a rotor with an intact degree of freedom it must not be interacting with the surface such a way that the rotor is more strongly bound to the surface than the stator. It is prudent to note here that the surface can also be the stator in some cases[12].
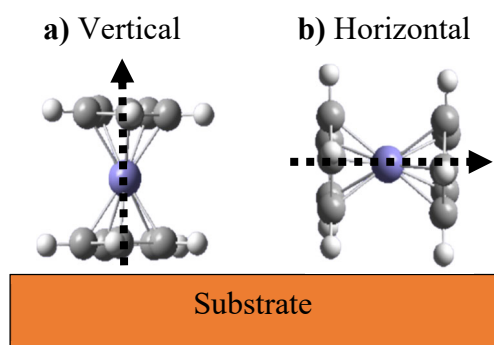
Figure 1: adsorption geometry denoting a) Vertical orientation and b) Horizontal orientation of a ferrocene molecule on surface
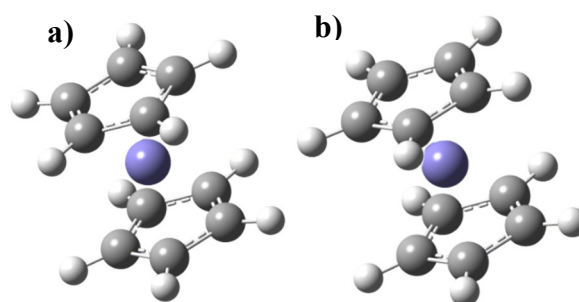
Figure 2: a) staggered ferrocene conformation and b) eclipsed ferrocene conformation

Working towards the creation of such molecular rotors is the primary goal of this work. One such interesting molecule with great potential as a molecular rotor is ferrocene. Its geometry is defined from the reference frame of the surface, about a common axis that passes through

the centre of both aromatic rings and the iron coordination centre (Fig. 1). Ferrocene has two configurations that are the basis of its rotational motion, staggered and eclipsed (Fig. 2).

1.3 Purposes

Surface deposition of a potential rotary nanodevice molecule, ferrocene, in ultra-high vacuum (UHV) has been done before, but without the specific goal of maintaining the rotational degree of freedom. STM imagery from these studies shows the self-assembly of the molecules does not provide an orientation suitable for nanodevices[13-15]. Therefore, investigating chemisorption methods like the Ullmann reaction, such that we can exploit on-surface bond cleavage and stabilisation, could provide a method of engineering favourable adsorption geometries.

Forming surface-bound nanodevices is a necessary step towards forming future molecular machines. The core aims of this work relate to exploration of methods for forming potential nanodevices and characterisation of formed products. These include:

1. Density functional theory investigation into the rotational barriers and adsorption geometry of ferrocene and dibromoferrocene.
2. Investigate the use of Ullmann dehalogenation to control the orientation of dibromoferrocene on various surfaces.
3. Investigation of the molecular orientation to determine if the rotational degree of freedom is maintained.
4. Determining other potential applications of the surface system that has been formed.

1.4 Significance

Nanodevices such as switches can be used to detect photons within an energy range, where a photon will cause the molecule to switch to a higher energy state[16,17]. When combined with charge transfer devices these can produce light sensors. They can also be used as controllable catalysts in reactions as the molecules active sites get moved to less advantageous positions.

Molecular rotors have been shown to be capable of manipulating micro scale objects[7]. However, most molecular machines have been utilising charge transfer and chiral switching molecules. Molecular rotors for molecular machines have not yet had the same volume of research that switches, and other devices have had. The potential of molecular rotors has therefore not been fully explored and surface localizability of a controllable rotor could go a long way to providing a platform for further study. A molecular rotor with a continuous

system of chiral states could allow 'stepping' through multiple isomorphic states or reactivities in a molecular machine. Current systems using molecular switches can switch between multiple separate states but stochiometric change must be made after the final state is reached[4,18].

1.5 Thesis Outline

This thesis is structured to complete a Master by monograph, and it made up of six chapters.

This chapter has introduced and outlined the concept of nanodevices, their fundamental purpose, the need for unique addressability of surface science and the wider scope of ramifications of advancement in the understanding of nanodevices.

Chapter 2 is a literature review containing a historical background into surface science, various types of nanodevice, a description of spintronics and the Ullmann reaction.

Chapter 3 covers the research design and methodology used in this thesis.

Chapter 4 contains a DFT study into the structure rotational barriers and adsorption geometry of ferrocene and dibromoferrocene and XPS results of as received dibromoferrocene powder.

Chapter 5 contains a study of dibromoferrocene deposition onto silver and gold 111 surfaces.

Chapter 6 summarises and connects the conclusions derived from each report and the overarching achievement of this thesis.

1.6 References

1   Jeon, W. S. *et al.* Molecular loop lock: a redox-driven molecular machine based on a host-stabilized charge-transfer complex. *Angew Chem Int Ed Engl* **44**, 87-91, doi:10.1002/anie.200461806 (2004).

2   Badjic, J. D. *et al.* Operating molecular elevators. *J Am Chem Soc* **128**, 1489-1499, doi:10.1021/ja0543954 (2006).

3   Vicario, J., Walko, M., Meetsma, A. & Feringa, B. L. Fine tuning of the rotary motion by structural modification in light-driven unidirectional molecular motors. *J Am Chem Soc* **128**, 5127-5135, doi:10.1021/ja058303m (2006).

4   Aubin-Tam, M. E., Olivares, A. O., Sauer, R. T., Baker, T. A. & Lang, M. J. Single-molecule protein unfolding and translocation by an ATP-fueled proteolytic machine. *Cell* **145**, 257-267, doi:10.1016/j.cell.2011.03.036 (2011).

5   Browne, W. R. & Feringa, B. L. Making molecular machines work. *Nat Nanotechnol* **1**, 25-35, doi:10.1038/nnano.2006.45 (2006).

6   Aprahamian, I. The Future of Molecular Machines. *ACS Cent Sci* **6**, 347-358, doi:10.1021/acscentsci.0c00064 (2020).

7   Kottas, G. S., Clarke, L. I., Horinek, D. & Michl, J. Artificial molecular rotors. *Chem Rev* **105**, 1281-1376, doi:10.1021/cr0300993 (2005).

8   Kay, E. R., Leigh, D. A. & Zerbetto, F. Synthetic molecular motors and mechanical machines. *Angew Chem Int Ed Engl* **46**, 72-191, doi:10.1002/anie.200504313 (2007).

9   Neilson, B. M. & Bielawski, C. W. Photoswitchable organocatalysis: using light to modulate the catalytic activities of N-heterocyclic carbenes. *J Am Chem Soc* **134**, 12693-12699, doi:10.1021/ja304067k (2012).

10   Estey, P., Bubar, A., Decken, A., Calhoun, L. & Eisler, S. Synthesis and photochemical isomerization of a propeller-shaped molecular switch. *Chem Eur J* **19**, 16204-16208, doi:10.1002/chem.201302879 (2013).

11   Ruther, R. E., Cui, Q. & Hamers, R. J. Conformational disorder enhances electron transfer through alkyl monolayers: ferrocene on conductive diamond. *J Am Chem Soc* **135**, 5751-5761, doi:10.1021/ja312680p (2013).

12   Tierney, H. L. et al. Experimental demonstration of a single-molecule electric motor. *Nat Nanotechnol* **6**, 625-629, doi:10.1038/nnano.2011.142 (2011).

13   Berger, J. *et al.* Study of Ferrocene Dicarboxylic Acid on Substrates of Varying Chemical Activity. *J Phys Chem C* **120**, 21955-21961, doi:10.1021/acs.jpcc.6b05978 (2016).

14   Wasio, N. A. *et al.* Self-assembly of hydrogen-bonded two-dimensional quasicrystals. *Nature* **507**, 86-89, doi:10.1038/nature12993 (2014).

15   Ormaza, M. *et al.* Assembly of Ferrocene Molecules on Metal Surfaces Revisited. *J Phys Chem Lett* **6**, 395-400, doi:10.1021/jz5026118 (2015).

16   de Silva, A. P. & Magri, D. C. Optical Sensing and Switching with Designed Molecules. *CHIMIA Int J Chem* **59**, 218-221, doi:10.2533/000942905777676579 (2005).

17   Yang, Y., Hughes, R. P. & Aprahamian, I. Near-infrared light activated azo-BF2 switches. *J Am Chem Soc* **136**, 13190-13193, doi:10.1021/ja508125n (2014).

18   Ceroni, P., Credi, A., Venturi, M. & Balzani, V. Light-powered molecular devices and machines. *Photochem Photobiol Sci* **9**, 1561-1573, doi:10.1039/c0pp00233j (2010).

Chapter 2: Literature Review

2.1 Historical background

The discipline of condensed matter physics has led to many technological advancements in electronics, devices and manufacturing methods that are the foundation of modern society. As devices such as the transistor, invented back in 1947[1], have trended towards the nanoscale, the physical science involved at the interface of a surface on the nanoscopic level has become more of a significant factor. Surface science is the study chemical, structural and electronic properties at the interface of two materials. How these materials naturally assemble due to electrostatic interactions, thermal excitation, electron orbitals and density of states are of great interest as they all effect emergent properties in various ways. These two materials are often a single crystal substrate and a deposited molecule. The nanoscopic structure of the absorbed molecule and the way they assemble on surfaces directs the resultant material properties. Producing new material combinations requires the consideration of what the end goal is and what the emergent properties might be. This is because there are so many different combinations of surface and molecule that there must be some level of reasoning as to what combination will possibly produce a desired outcome.

Desired products in surface science can be anything from useful electronic[2,3] or physical properties[4-6], to interesting molecular assemblies[7-9]. Desired outcomes include the understanding of fundamental physico-chemical processes and interactions. In this work the desired physical property is that ferrocene maintains its rotational degree of freedom[10]. Building up from previous knowledge, much work has been done regarding the motion of molecules in the past and the control of biological molecular rotors, along with the formation of synthetic molecular devices[11,12].

Biological systems, however, are different as they are solution based yet have a significant number of nanodevices such as proteins that can precisely control the formation of molecular structures to build DNA or other biological structures[13]. Replication of such complex structures could potentially be a great tool for the health and manufacturing industries. Controllable prototypical devices are desired as tools to assist in the realisation of such designs. While such devices in solution are good for chemical and property analysis, surface deposition is required for addressability for nanodevices to integrate with existing device architecture[14,15].

Research on controlled mechanical motion of nanodevices was started in the 1990s and has been steadily progressing ever since[16]. From large rotaxane based structures to single molecule rotors, the area of nanotechnology has led to the focus of producing better, more specialised materials and structures on the nanoscale. Present day surface science focuses on emerging technologies such as organic frameworks[17], molecular assemblies[4,7,18] and nanodevices[19,20]. Forming these structures requires consideration of the thermodynamic processes, electronic interactions, and chemical reactions that are involved. Due to the processes that must be considered, there is a limit to the level of direct control that surface science possesses at the nanoscale. Surface science limits these reactions to a single 2D interface/plane, localising the products to where they can be addressable, guiding molecule-molecule interactions that otherwise would be more 3D.

2.2 Nano devices

Nanodevices that can be precisely controlled or that are predictable could be designed to manipulate molecules on the nanoscale into desired structures without the reliance on spontaneous processes[13]. Nanodevices that can perform a predictable motion have been made in previous works. Such devices are molecular propellers[21], molecular rotors[22] and molecular switches[23].

Molecular rotors can rotate 2π radians around a single covalent bond. Past work on a light-driven molecular rotor, made of sterically overcrowded symmetric biphenanthrylidene, shows the level of control possible in nanodevices[22]. This helical molecular rotor is photoisomerizable containing four stable isomers between a C=C bond (Fig. 3). It has been shown that this molecule can rotate 2π radians in solution with a combination of photon activation and heating. When interacting with a photon of ≥280 nm it rotates from cis-trans and trans-cis positions and when heated to 60 °C it returns to the global minima positions[14]. This molecular rotor has many researched derivatives that allow for varied shapes and characteristics, such as rotational speed variations up to a factor of 10^8 from one design to another with rotational speeds controllable by applied electric currents[22].
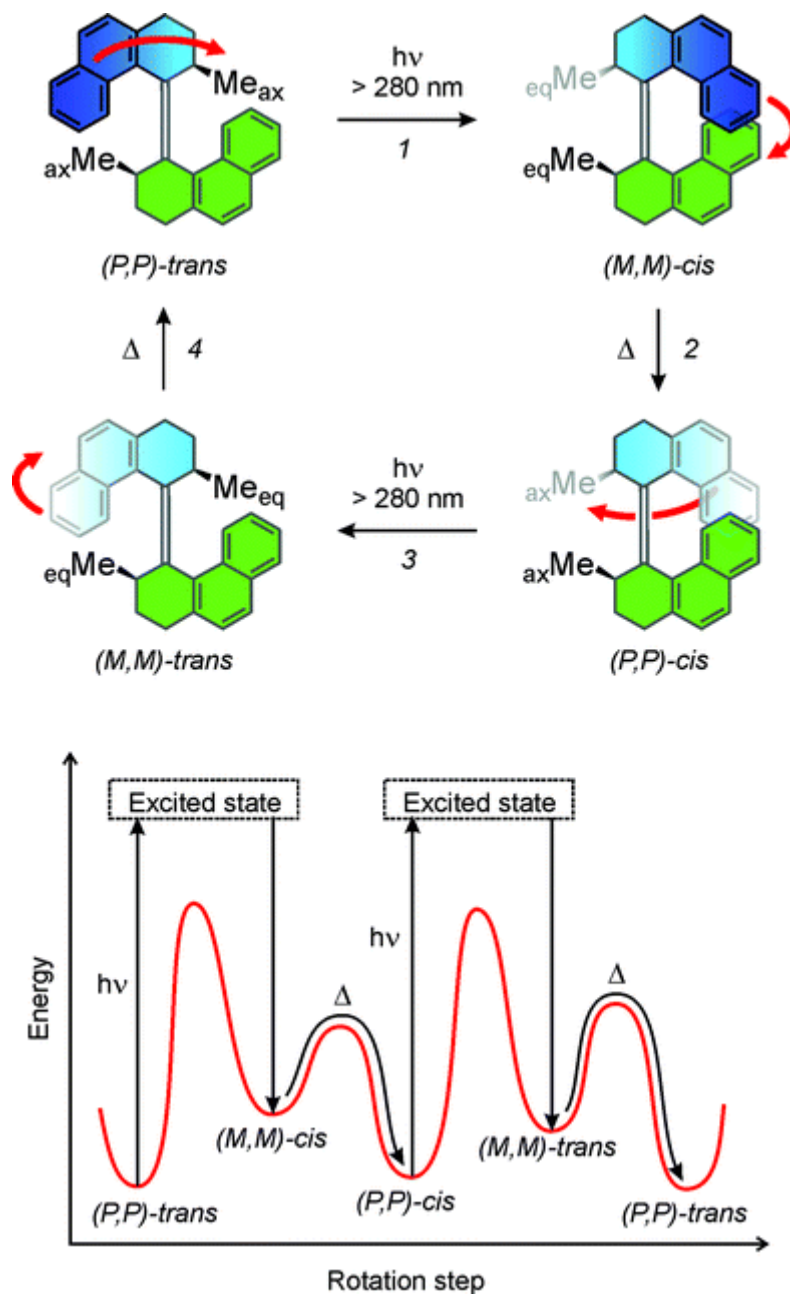
Figure 3: Photochemically activated unidirectional rotation in a biphenanthrylidene species. The mechanism consists of four steps; each light-driven, energetically uphill process is followed by a thermal, energetically downhill process. *Used with permission of Royal Society of Chemistry, from Ceroni, P., Credi, A., Venturi, M. & Balzani, V. Light-powered molecular devices and machines. Photochem Photobiol Sci **9**, 1561-1573, doi:10.1039/c0pp00233j (2010); permission conveyed through Copyright Clearance Center, Inc.*

The electronic speed control is due to the push-pull effect on the C=C bond by the amino and carbonyl groups. Ultimately the work found that rotational speed is controllable with the use of different substituents. Derivatives of this molecule have been tethered to liquid crystal gold nanoparticles and used to induce rotation of a glass rod within the liquid[15].

Molecular switches are molecules that undergo isomerisation, changing bonds or bond angles[21,24,25]. Past work on molecular switches shows the large variability in form and function of the molecular switch[21,23]. Molecular switches have been used as controllable catalysts[26], where the switching action changes the catalytic nature of the molecule, which offers a way of controlling the speed of the catalysed reaction. 4,5-dithienylimidazolium salt (Fig. 4) is an example of a photochemically activated molecular switch that has been used to change the catalytic strength of N-heterocyclic carbenes[26].
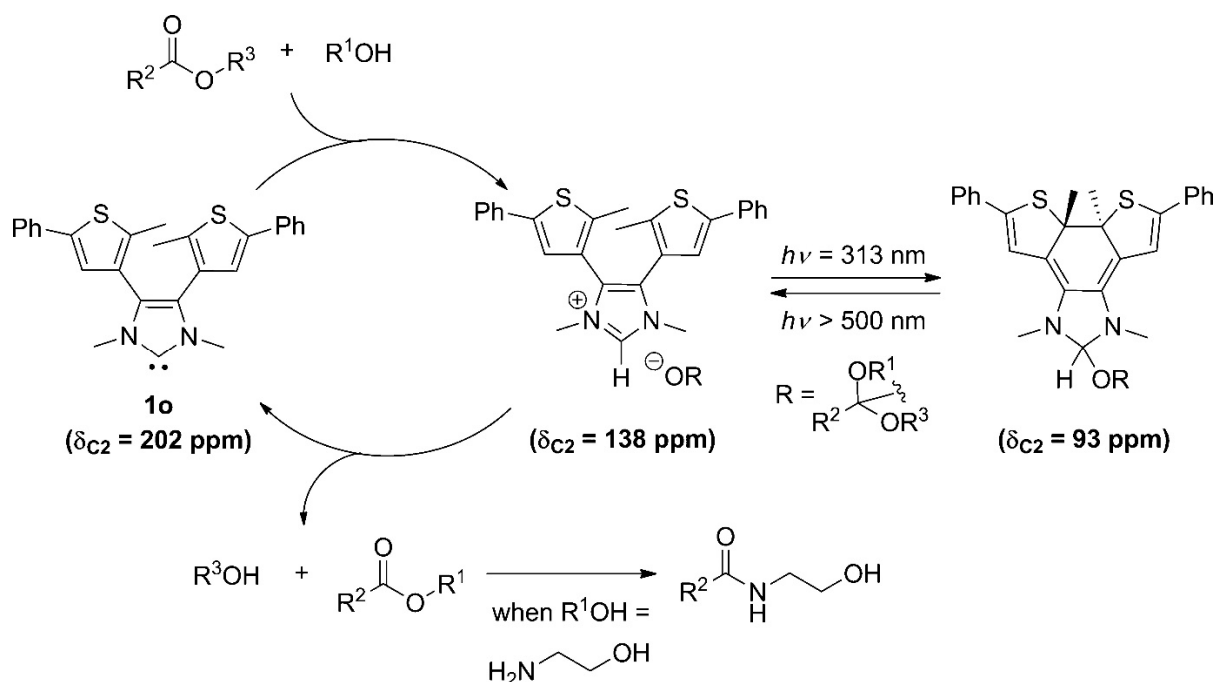
Figure 4: Mechanism of Photoswitchable N-Heterocyclic Carbenes Catalyzed Condensation Reactions. *Reprinted (adapted) with permission from Neilson, B. M. & Bielawski, C. W. Photoswitchable organocatalysis: using light to modulate the catalytic activities of N-heterocyclic carbenes. J Am Chem Soc **134**, 12693-12699, doi:10.1021/ja304067k (2012). Copyright 2012 American Chemical Society.*

Another type of molecular switch is a multi-stable molecular switch that has more than one stable molecular state but is not reversable (Fig. 5). A propeller-like molecule with phenyl group "blades" has been formed that switches incrementally with exposure to 365 nm light[23].
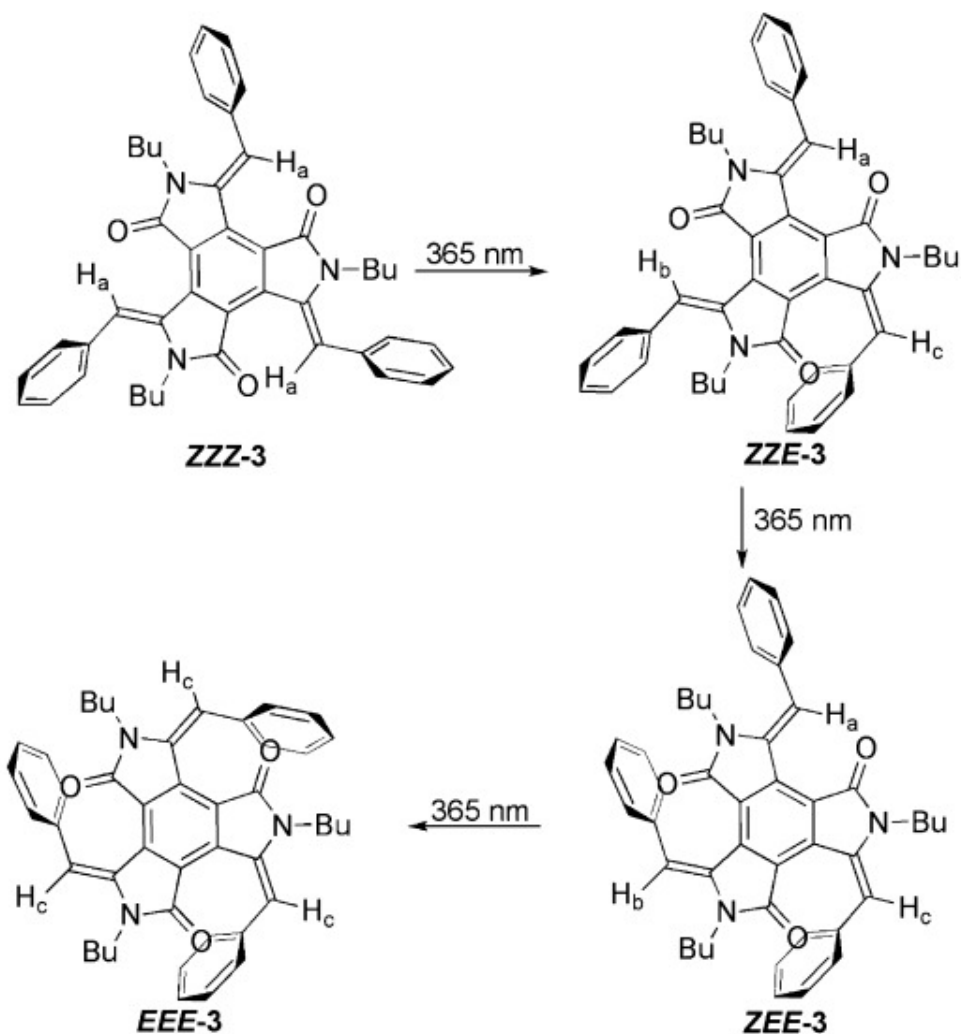
Figure 5: multi point molecular switch. *Used with permission of John Wiley and Sons, from Estey, P., Bubar, A., Decken, A., Calhoun, L. & Eisler, S. Synthesis and photochemical isomerization of a propeller-shaped molecular switch. Chemistry 19, 16204-16208, doi:10.1002/chem.201302879 (2013).*

Molecular motors and molecular switches have also been shown to have applications in medicine and sensing[27]. They have also been theorised to have potential in data applications such as high-density data storage and as logic gates[25].

2.3 Molecular machines and atomic level manipulation

Molecular machines with multiple moving part have been produced in the past[28,29], however whereas atomic manipulation via large instruments such as STMs has been shown before[30,31], atomic manipulation via direct manipulation by a synthetic molecular machine with multiple moving parts has not yet been achieved. A few molecular machines have been realised in recent times that act as locks[32], rotors[13], elevators[28,29] and shuttles[16] for electric charge. One of the first molecular machines was a pair of mechanically interlocked molecules, a molecular system known as a catenane[33]. While catenanes had no immediate uses, the

concept was a basis for many other research pathways for molecular machines. Such molecular machines derived from the catenane concept have been used to mimic the complex tasks found in biomolecular machines[29,34]. Recently most developments in molecular machines have been based on the rotaxane molecular machine[16,28,29,32], the successor to catenane[35].

2.4 Ferrocene

Ferrocene (bis(η^5-cyclopentadienyl)iron) has the potential for use as a molecular rotor due to having a rotational degree of freedom. Ferrocene was discovered in 1951[36] and possesses interesting electric, redox properties, as well as being uncharacteristically stable for an organometallic structure[36,37]. Past research with ferrocene and ferrocene functionalisations
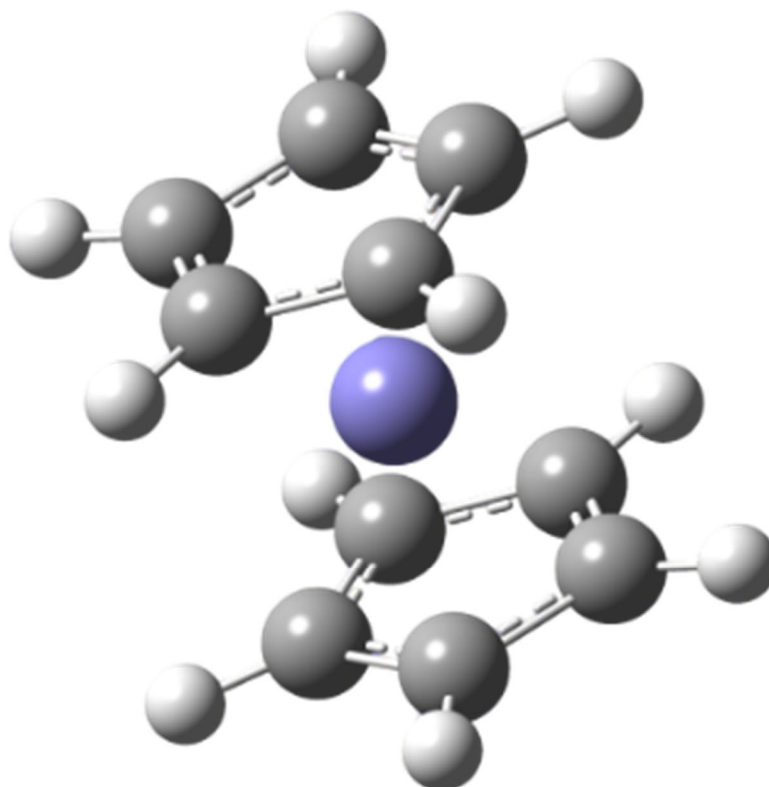
Figure 6: Ferrocene

focussed on catalysis[38], prototypical surface assemblies[9,39,40], electron transfer materials[20,41], electronics[3,42] and sensing[43,44], nanotube formation[18,45] and much more[46,47].

Ferrocene (Fig. 6) is diamagnetic and has a dipole moment of 0.05 D despite being a symmetric molecule, making it slightly magnetic. It has a redox potential of -0.59 V and the effective number of electrons interacting with the iron core is 36[36]. Ferrocene is also Jahn–

Teller effect (JTE) inactive, meaning it has spatially degenerate ground states[37]. Ferrocene's ligand structure allows for full 2π rotation in omnidirectionally with 2 major stable conformations, eclipsed where the aromatic rings are aligned and staggered. Its stabilisation of carbocations opens the opportunity for many functionalised derivatives[47] allowing for any desired changes in functionalisation. Electron correlation effects have been found to be more significant in the central Fe(II) than the surrounding carbon atoms[37]. This makes sense due to the large number of electrons interacting with the Fe(II) core between the aromatic rings.
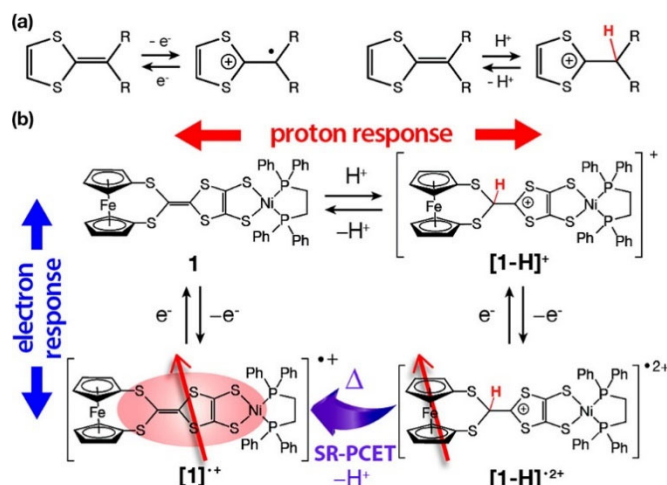
Figure 7: Charge transfer via reversable proton response to exterior heating. Reprinted (adapted) with permission from Tanushi, A., Kusamoto, T., Hattori, Y., Takada, K. & Nishihara, H. Spin-reconstructed proton-coupled electron transfer in a ferrocene-nickeladithiolene hybrid. J Am Chem Soc 137, 6448-6451, doi:10.1021/jacs.5b02118 (2015). Copyright 2015 American Chemical Society.

Past work on ferrocene has been in the form of novel charge transfer devices and electrochemical sensors[44]. It was found in making a ferrocene-nickeladithiolene hybrid multi-stimuli response system (Fig. 7), that most of the electron spin density was indeed localised around the Fe atom in the ferrocene[41]. When externally stimulated the system responded by electron transfer and de/protonation. The significant correlation effects and electron spin density found localised around the Fe core are what makes ferrocene a possible building block for molecular wires carrying spin-polarised currents. In combination with the rotational degree of freedom, ferrocene is a strong contender for nanodevices[40] such as molecular rotors[48], logic gates[49] and charge transfer devices. Ferrocene also has potential in devices that provide mechanical interaction like molecular gears[50] for use in molecular machines and spintronics[39].

2.5 The Ullmann reaction

The Ullmann reaction was first described by Fritz Ullmann in 1901; in this reaction, catalytic activation of an aryl halide in a colloid of copper powder in sulphuric acid led to the

formation of C-C bonding through aryl-aryl coupling[51]. Ullmann dehalogenation and coupling reactions are a simple and powerful method of forming organometallic and organic nanostructures on metallic surfaces[52]. Ullman dehalogenation occurs when a halocarbon dissociates through interaction with a metallic catalyst (noble metals) and forms a covalent bond with a metallic surface adatom (C-Metal). To complete the Ullmann reaction the dehalogenated C-M bond must form a C-C bond. This can occur directly after halogen dissociation skipping the C-M stage all together. But if C-M bonds have been formed, C-C bonding occurs when the metal adatom has two organometallic bonds simultaneously (C-M-C) and there is enough energy to facilitate breaking the C-M bonds. The cleaved off halogen can then chemisorb or desorb from the surface.

Most surface science is performed on single crystal substrates of specific crystallographic orientations. A single crystal is a high purity substrate of a single element that has a continuous crystal lattice in all directions, breaking only on the substrate surfaces. Surface reactivity as well as halocarbon bond strength are the significant factors in dehalogenation and assembly geometry of deposited molecules. The single-crystal element and its crystallographic orientation are the most significant factors in selecting a surface for an Ullmann reaction to occur. The single-crystal element is usually one of Cu, Ag or Au, as their reactivity, the strength to dislocate an electron in a covalent bond, is within the average range of the halocarbon bond strength of C-Cl (3.4 eV), C-Br (2.9 eV) and C-I (2.3 eV)[4,52]. The surface reactivity can also be fine-tuned by selecting different crystallographic orientations, changing the atomic corrugation of the surface depending on the type of crystal structure that the element forms (FCC, HCP, etc.). For example, more atomically corrugated surfaces, like (110), are more reactive than isotropic densely packed (111) surfaces[52]. Atomic corrugation can also act as a template for assembly of 1D molecular chains.

Recent work with on surface Ullmann reaction observed the first steps of the Ullmann reaction (Fig. 8), via adatom mediated structural transformation of bromoarene monolayers[53].
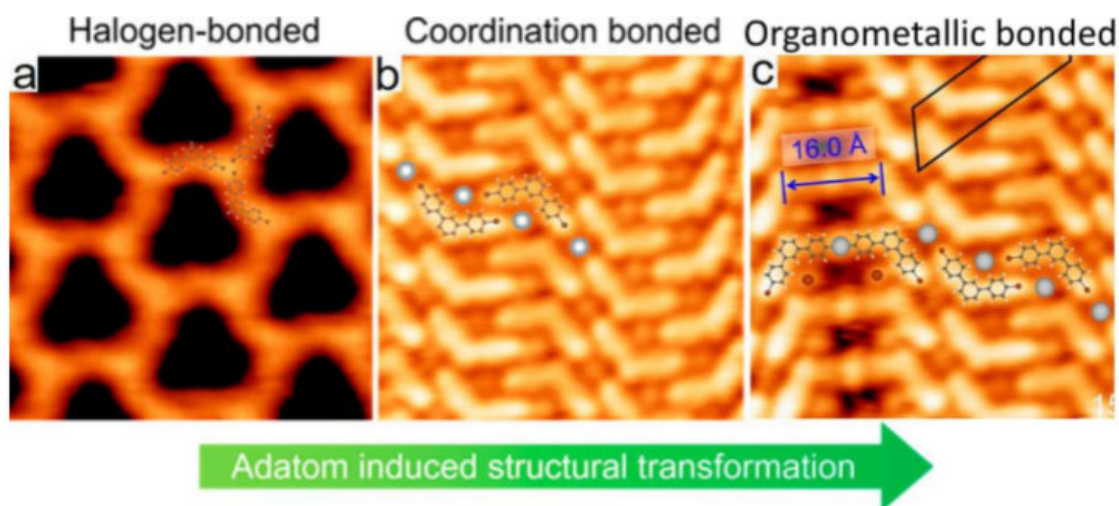
Figure 8: Thermally induced steps of the Ullmann reaction process. *Reprinted (adapted) with permission from Fan, Q. et al. Surface Adatom Mediated Structural Transformation in Bromoarene Monolayers: Precursor Phases in Surface Ullmann Reaction. ACS Nano 12, 2267-2274, doi:10.1021/acsnano.7b06787 (2018). Copyright 2018 American Chemical Society*

The structural transformation occurs with increasing annealing temperatures demonstrating the possible level of control over the Ullmann reaction. Other works also highlighted the effect of reactivity on the dehalogenation event[4,54] and the crystallographic orientations influence on the surface coordination[6].

2.6 Surface adsorption of ferrocene derivatives

Past depositions of ferrocene derivatives onto various surfaces has been well studied with a focus on noble metal substrates. Sublimation deposition is the most common form of deposition method for ferrocene derivatives. Depositions include ferrocene onto Cu(111) and (100)[55], ferrocene onto Au(111)[56], ferrocene-dithiol onto Si(111) - Ag $\sqrt{3} \times \sqrt{3}$[57], ferroceneacetic and ferrocenedicarboxylic acid onto Au(111)-on-mica[58], ferrocenedicarboxylic acid onto Ag(111), Cu(110) and Cu_3N/Cu(110)[59], mercaptoalkylferrocenes onto Ag(111)[60] and many more.

Ferrocene on Cu(111) and (100) forms well-ordered self-assembled monolayers, comprising of both horizontally and vertically oriented ferrocene in the assemblies. Ferrocene was deposited at room temperature via dosing line sublimation onto Cu(111) and (100) at <100 K and adsorption rate was 1.2 mL/min and then cooled to 4.5 K for the STM imagery (Fig. 9).
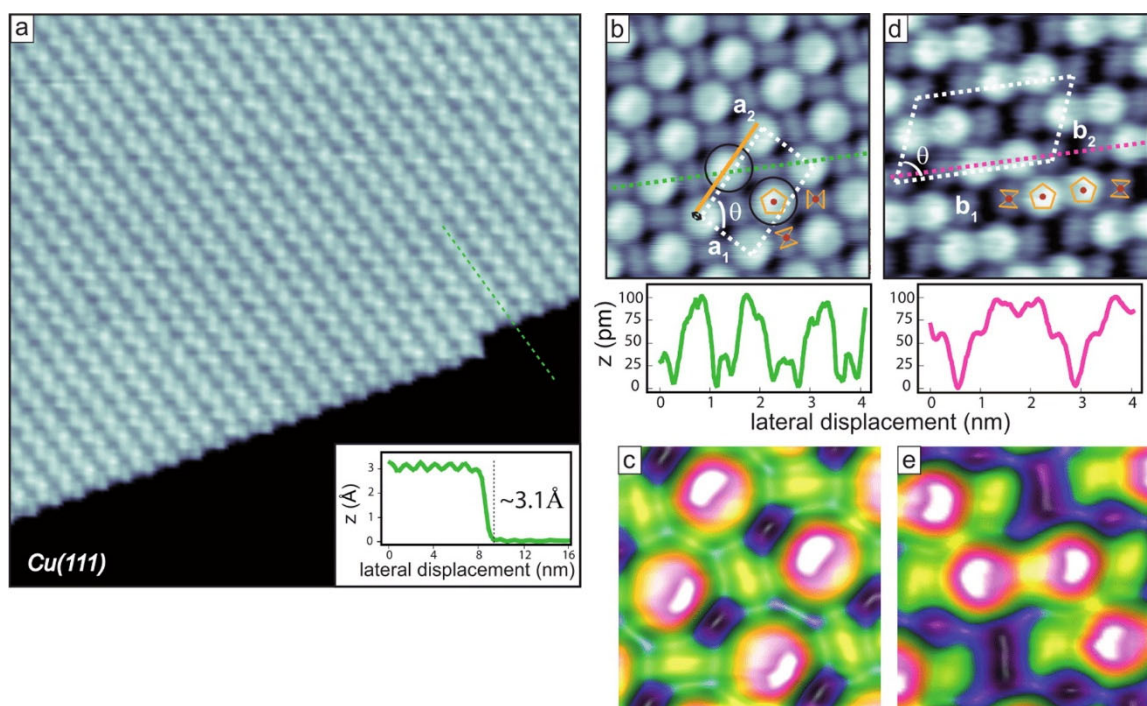
Figure 9: (a) STM image of 0.6 monolayer FeCp2 deposited on Cu(111) (+1 V, 0.5 nA). Inset: Height profile of the molecular monolayer. Two different configurations are observed on Cu(111): (b) compact (−1 V, 0.5 nA) and (d) zigzag (+0.1 V, 0.2 nA). The unit cells (white dashed lines) composed of vertical and horizontal molecules, as well as the line profiles of both arrangements, are shown in each image. (b–d) Close-up view of the two configurations, highlighting the asymmetry of the rings in the vertical molecules. Image sizes: (a) 30 × 30 nm^2, (b–d) 4 × 4 nm^2, (c–e) 2 × 2 nm^2. *Reprinted (adapted) with permission from Ormaza, M. et al. Assembly of Ferrocene Molecules on Metal Surfaces Revisited. J Phys Chem Lett* **6**, *395-400, doi:10.1021/jz5026118 (2015). Copyright 2015 American Chemical Society.*

Ferrocene on Au(111) is shown to adsorb dissociatively at low temperatures (below 250 K) forming a two-layer structure[56]. The ferrocenes were deposited via dosing line sublimation at RT, onto cooled Au(111) with STM performed at 5 K. Braun et.al. states that ferrocene will desorb above 250 K from an Au surface. The structures are two-layer with the top layer forming ringlike assemblies from pairs of Cp rings and the bottom layer forms a threefold symmetry from ferrocene and Cp-Fe complexes (Fig. 10).
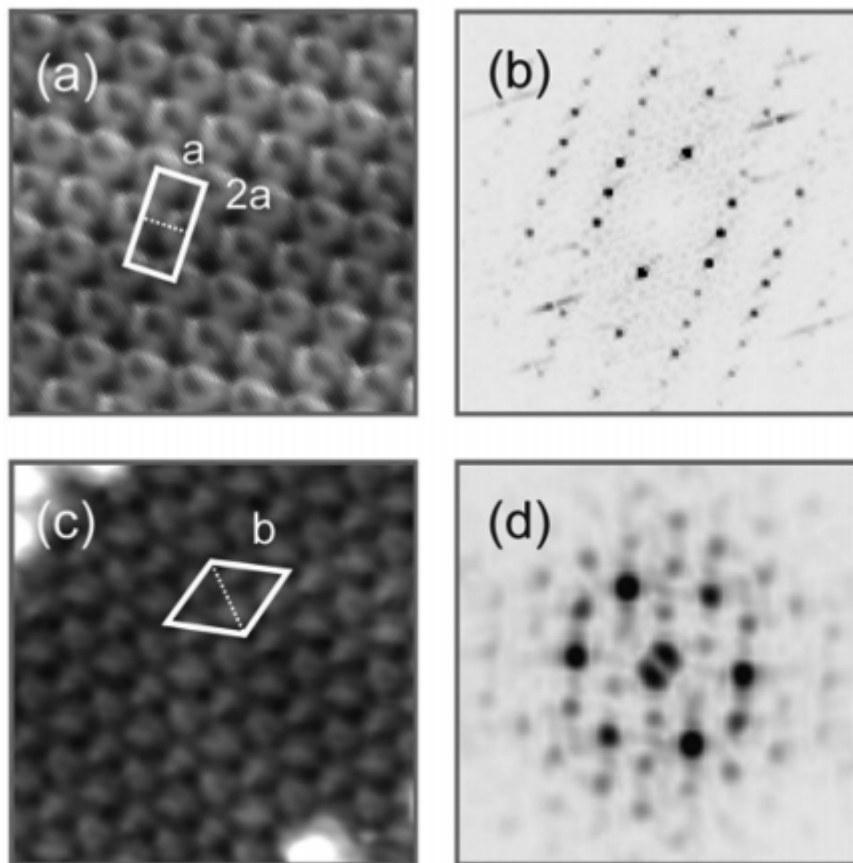
Figure 10: (a) Image showing an area from domain A (62 Å×62 Å, 11.2 GΩ, U=−1.12 V). The cyclopentadienyl rings form tilted rows with a rectangular unit cell (a=8.7 Å) while (c) the first layer has a rhombic unit cell (b=12.4 Å). (b) and (d) show the respective powerspectra (5.1 Å−1×5.1 Å−1) of (a) and (c). *Reprinted "FIG. 2" with permission from Braun, K. F., Iancu, V., Pertaya, N., Rieder, K. H. & Hla, S. W. Decompositional incommensurate growth of ferrocene molecules on a Au(111) surface. Phys Rev Lett 96, 246102, doi:10.1103/PhysRevLett.96.246102 (2006). Copyright 2006 by the American Physical Society.*

Ferrocene-dithiol on Si(111) - Ag $\sqrt{3} \times \sqrt{3}$ was found to deprotonate the thiol groups on interaction with Ag groups at room temperature. The adsorbed ferrocene was adsorbed horizontally after deprotonation of both thiol groups (Fig. 11)[57]. The ferrocene-dithiol was deposited via evaporation at 500 K and adsorption was slow at 0.01 mL/min. Mass spectrometry picked up other hydrocarbon species suggesting thermal defragmentation from the 500 K evaporation.
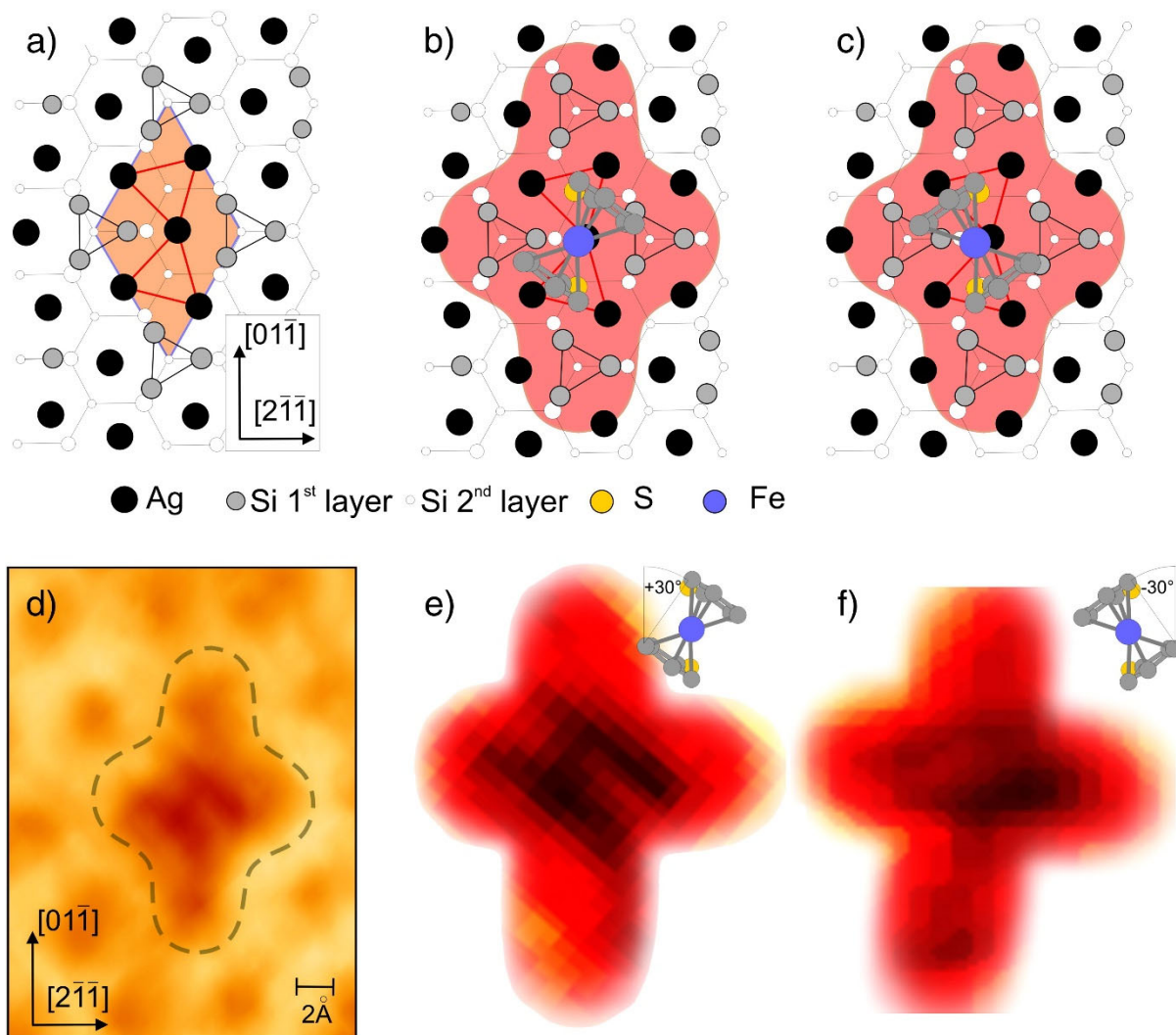
Figure 11: Structure models (a–c) and STM images (+ 3 V, 0.25 nA, 300 K) (d–f) before (a) and after adsorption of FDT (b–f) on the Ag√3 × √3 structure. The Ag-trimers in the HCT model are marked by red lines. The cross structure visible in d)–f) are schematically shown in b) and c) as well. After subtraction of the background in d) two different orientations of the ferrocene with respect to the unit cell of the √3 × √3 are found (e, f). *Reprinted from Tegenkamp, C., Schmeidel, J. & Pfnür, H. Chemisorption of ferrocene on Si(111)– Ag: Frustrated conformational flexibility. Surface Science **605**, 267-271, doi:10.1016/j.susc.2010.10.027 (2011). Copyright 2011, with permission from Elsevier.*

Ferroceneacetic and ferrocenedicarboxylic acid onto Au(111)-on-mica was deposited via pulsed solenoid valve at room temperature saturating the surface. Ferroceneacetic was seen to from rows of dimers and ferrocenedicarboxylic formed quasicrystalline pentamers (Fig. 12)[58]. Both structures contained a combination of vertically and horizontally adsorbed ferrocene.
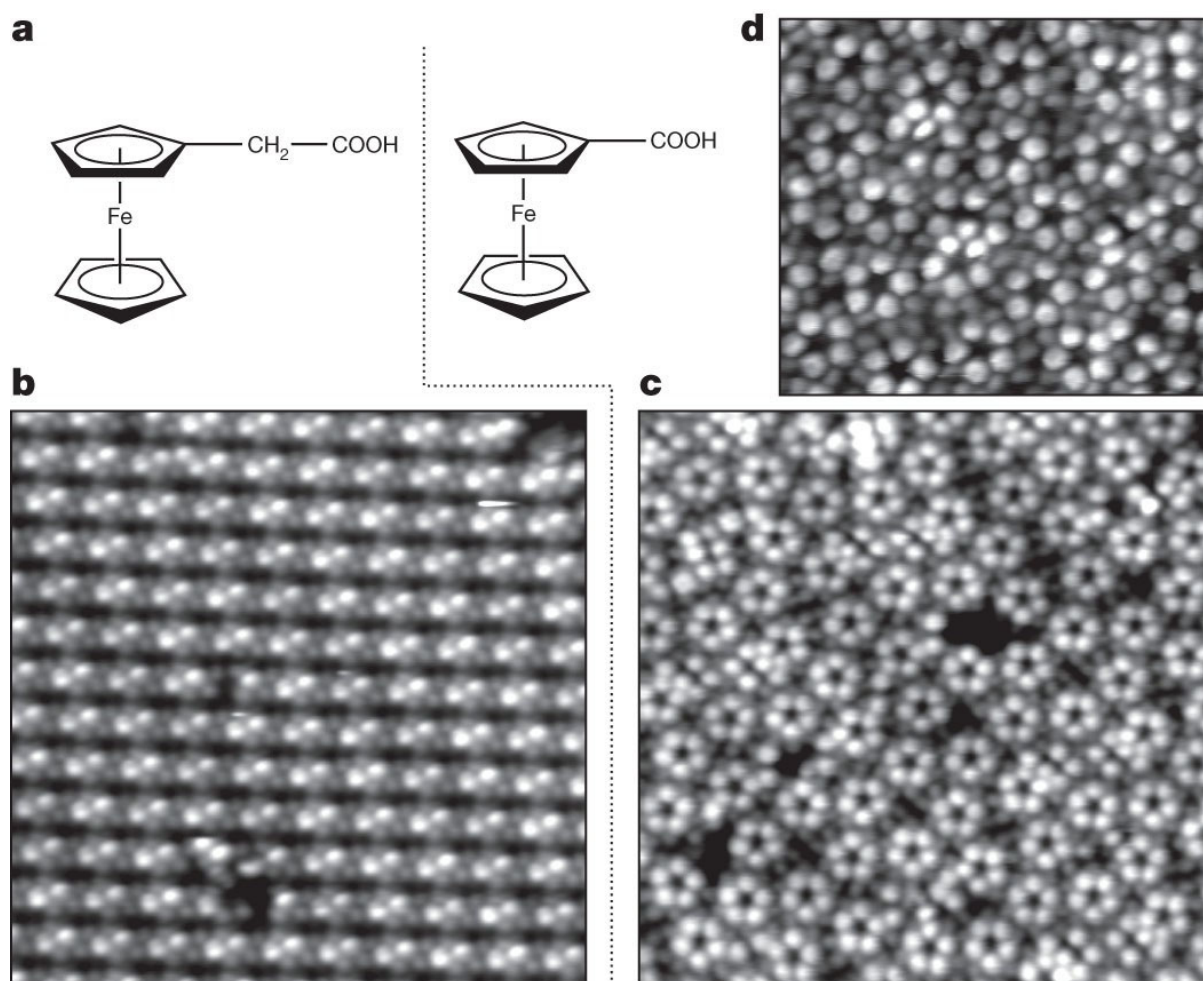
Figure 12: a, Structure of FcCH2COOH and FcCOOH acid. b, c, Rows of dimers are observed for FcCH2COOH (b), whereas the structure of FcCOOH (c) is dominated by pentamers; both images are 205 Å × 205 Å. d, Higher-resolution, 110 Å × 100 Å image showing submolecular structure in the FcCOOH Cp rings; dimmer features packed between pentamers also appear more clearly in this image. *Reprinted by permission from Springer Nature, Wasio, N. A. et al. Self-assembly of hydrogen-bonded two-dimensional quasicrystals. Nature* **507***, 86-89, doi:10.1038/nature12993 (2014). Copyright Springer Nature 2014.*

Functionalized derivatives of ferrocene and the substrate as well as deposition technique can all have a significant impact on the resulting structures.

2.7 Chapter Summary

Nanodevice research is an exciting field of research that challenges fundamental understandings of physico-chemical interactions for the formation of molecular machines. Research in this field has the potential to revolutionise how nanotechnology is produced, our control over the nanoscale as well as the foundations of electronics.

Many machines formed from rotaxane and rotaxane variants show how a single robust controllable nanodevice can lead to several molecular machines and innovative structures.

Ferrocene has the potential add to this toolkit as a significant contributor to future innovation in the field of molecular machines and spintronics.

Ullmann dehalogenation is a predictable method of forming surface bound systems and polymers. Utilising this method of surface coupling should assist in simplifying the analysis of the results. The Ullmann reactions that occur in this work should match expected stoichiometry from pervious works allowing a semi-predictable outcome. If the stoichiometry does not match what is predicted, then the well documented reaction process should prove useful in guiding this research.

The desired outcome in this work is the realisation of a novel surface-confined ferrocene based molecular rotors. Surface-confined molecular rotors formed from ferrocene have not been demonstrated previously. Previous works have shown that motion control via light activation of gold nanoparticle surface bound molecular rotors is possible[15]. This work will assist in paving the way for future surface-bound nanodevices for use in molecular machines.

2.7 References

1   Ross, I. M. The invention of the transistor. *Proc IEEE* **86**, 7-28, doi:10.1109/5.658752 (1998).

2   Caridad, J. M. *et al.* A Graphene-Edge Ferroelectric Molecular Switch. *Nano Lett* **18**, 4675-4683, doi:10.1021/acs.nanolett.8b00797 (2018).

3   Tarafder, K., Surendranath, Y., Olshansky, J. H., Alivisatos, A. P. & Wang, L. W. Hole transfer dynamics from a CdSe/CdS quantum rod to a tethered ferrocene derivative. *J Am Chem Soc* **136**, 5121-5131, doi:10.1021/ja500936n (2014).

4   Cirera, B. *et al.* Efficient Lanthanide Catalyzed Debromination and Oligomeric Length-Controlled Ullmann Coupling of Aryl Halides. *J Phys Chem C* **121**, 8033-8041, doi:10.1021/acs.jpcc.7b02172 (2017).

5   Yi, M., Xu, B.-X., Müller, R. & Gross, D. Strain-mediated magnetoelectric effect for the electric-field control of magnetic states in nanomagnets. *Acta Mechanica* **230**, 1247-1256, doi:10.1007/s00707-017-2029-7 (2017).

6   Zint, S. *et al.* Imaging Successive Intermediate States of the On-Surface Ullmann Reaction on Cu(111): Role of the Metal Coordination. *ACS Nano* **11**, 4183-4190, doi:10.1021/acsnano.7b01109 (2017).

7   Baviloliaei, M. S. & Diekhoner, L. Molecular self-assembly at nanometer scale modulated surfaces: trimesic acid on Ag(111), Cu(111) and Ag/Cu(111). *Phys Chem Chem Phys* **16**, 11265-11269, doi:10.1039/c4cp01429d (2014).

8   Lipton-Duffin, J., Abyazisani, M. & MacLeod, J. Periodic and nonperiodic chiral self-assembled networks from 1,3,5-benzenetricarboxylic acid on Ag(111). *Chem Commun (Camb)* **54**, 8316-8319, doi:10.1039/c8cc04380a (2018).

9   Wasio, N. A. *et al.* Self-assembly of hydrogen-bonded two-dimensional quasicrystals. *Nature* **507**, 86-89, doi:10.1038/nature12993 (2014).

10   Sorriso, S. Energy barrier to internal rotation in some ferrocene derivatives from dielectric measurements. *J Organomet Chem* **179**, 205-213, doi:10.1016/s0022-328x(00)95223-9 (1979).

11   Keith Dunker, A. & Marvin, D. A. A model for membrane transport through α-helical protein pores. *J Theor Biol* **72**, 9-16, doi:10.1016/0022-5193(78)90015-2 (1978).

12   Feynman, R. There's Plenty of Room at the Bottom. American Physical Society. Pasadena, Los Angeles County, California, United States. (1959).

13   Ketterer, P., Willner, E. M. & Dietz, H. Nanoscale rotary apparatus formed from tight-fitting 3D DNA components. *Sci Adv* **2**, e1501209, doi:10.1126/sciadv.1501209 (2016).

14   Ceroni, P., Credi, A., Venturi, M. & Balzani, V. Light-powered molecular devices and machines. *Photochem Photobiol Sci* **9**, 1561-1573, doi:10.1039/c0pp00233j (2010).

15   Boyle, M. M. *et al.* Mechanised materials. *Chem. Sci.* **2**, 204-210, doi:10.1039/c0sc00453g (2011).

16   Anelli, P. L., Spencer, N. & Stoddart, J. F. A molecular shuttle. *J Am Chem Soc* **113**, 5131-5133, doi:10.1021/ja00013a096 (1991).

17   Vaitsis, C., Sourkouni, G. & Argirusis, C. Metal Organic Frameworks (MOFs) and ultrasound: A review. *Ultrason Sonochem*, doi:10.1016/j.ultsonch.2018.11.004 (2018).

18   Hudson, Z. M. & Manners, I. Assembly and disassembly of ferrocene-based nanotubes. *Science* **344**, 482-483, doi:10.1126/science.1254140 (2014).

19   Ghosh, A. & Fischer, P. Controlled propulsion of artificial magnetic nanostructured propellers. *Nano Lett* **9**, 2243-2245, doi:10.1021/nl900186w (2009).

20   Ruther, R. E., Cui, Q. & Hamers, R. J. Conformational disorder enhances electron transfer through alkyl monolayers: ferrocene on conductive diamond. *J Am Chem Soc* **135**, 5751-5761, doi:10.1021/ja312680p (2013).

21   Martinez, A., Guy, L. & Dutasta, J. P. Reversible, solvent-induced chirality switch in atrane structure: control of the unidirectional motion of the molecular propeller. *J Am Chem Soc* **132**, 16733-16734, doi:10.1021/ja102873x (2010).

22   Vicario, J., Walko, M., Meetsma, A. & Feringa, B. L. Fine tuning of the rotary motion by structural modification in light-driven unidirectional molecular motors. *J Am Chem Soc* **128**, 5127-5135, doi:10.1021/ja058303m (2006).

23   Estey, P., Bubar, A., Decken, A., Calhoun, L. & Eisler, S. Synthesis and photochemical isomerization of a propeller-shaped molecular switch. *Chemistry* **19**, 16204-16208, doi:10.1002/chem.201302879 (2013).

24   Mielke, J. *et al.* Molecules with multiple switching units on a Au(111) surface: self-organization and single-molecule manipulation. *J Phys Condens Matter* **24**, 394013, doi:10.1088/0953-8984/24/39/394013 (2012).

25   Zheng, H.-R. *et al.* A multi-stimuli-responsive fluorescence switch based on E–Z isomerization of hydrazone. *RSC Adv* **6**, 41002-41006, doi:10.1039/c6ra01507g (2016).

26   Neilson, B. M. & Bielawski, C. W. Photoswitchable organocatalysis: using light to modulate the catalytic activities of N-heterocyclic carbenes. *J Am Chem Soc* **134**, 12693-12699, doi:10.1021/ja304067k (2012).

27   Yang, Y., Hughes, R. P. & Aprahamian, I. Near-infrared light activated azo-BF2 switches. *J Am Chem Soc* **136**, 13190-13193, doi:10.1021/ja508125n (2014).

28   Badjic, J. D. *et al.* Operating molecular elevators. *J Am Chem Soc* **128**, 1489-1499, doi:10.1021/ja0543954 (2006).

29   Bruns, C. J. & Stoddart, J. F. Rotaxane-based molecular muscles. *Acc Chem Res* **47**, 2186-2199, doi:10.1021/ar500138u (2014).

30   Rosei, F. *et al.* Organic molecules acting as templates on metal surfaces. *Science* **296**, 328-331, doi:10.1126/science.1069157 (2002).

31   Fuechsle, M. *et al.* A single-atom transistor. *Nat Nanotechnol* **7**, 242-246, doi:10.1038/nnano.2012.21 (2012).

32   Jeon, W. S. *et al.* Molecular loop lock: a redox-driven molecular machine based on a host-stabilized charge-transfer complex. *Angew Chem Int Ed Engl* **44**, 87-91, doi:10.1002/anie.200461806 (2004).

33   Wasserman, E. The Preparation of Interlocking Rings: A Catenane1. *J Am Chem Soc* **82**, 4433-4434, doi:10.1021/ja01501a082 (1960).

34   Meng, Z. *et al.* Stepwise Motion in a Multivalent [2](3)Catenane. *J Am Chem Soc* **137**, 9739-9745, doi:10.1021/jacs.5b05758 (2015).

35   Li, Z., Liu, W., Wu, J., Liu, S. H. & Yin, J. Synthesis of [2]catenanes by template-directed clipping approach. *J Org Chem* **77**, 7129-7135, doi:10.1021/jo3012804 (2012).

36   Wilkinson, G., Rosenblum, M., Whiting, M. C. & Woodward, R. B. The Structure of Iron Bis-Cyclopentadienyl. *J Am Chem Soc* **74**, 2125-2126, doi:10.1021/ja01128a527 (1952).

37   Islam, S. & Wang, F. The d-electrons of Fe in ferrocene: the excess orbital energy spectrum (EOES). *RSC Adv* **5**, 11933-11941, doi:10.1039/c4ra14506b (2015).

38   Foo, K., Sella, E., Thome, I., Eastgate, M. D. & Baran, P. S. A mild, ferrocene-catalyzed C-H imidation of (hetero)arenes. *J Am Chem Soc* **136**, 5279-5282, doi:10.1021/ja501879c (2014).

39   Ormaza, M. *et al.* Assembly of Ferrocene Molecules on Metal Surfaces Revisited. *J Phys Chem Lett* **6**, 395-400, doi:10.1021/jz5026118 (2015).

40   Berger, J. *et al.* Study of Ferrocene Dicarboxylic Acid on Substrates of Varying Chemical Activity. *J Phys Chem C* **120**, 21955-21961, doi:10.1021/acs.jpcc.6b05978 (2016).

41   Tanushi, A., Kusamoto, T., Hattori, Y., Takada, K. & Nishihara, H. Spin-reconstructed proton-coupled electron transfer in a ferrocene-nickeladithiolene hybrid. *J Am Chem Soc* **137**, 6448-6451, doi:10.1021/jacs.5b02118 (2015).

42   Zhu, H. & Li, Q. Novel Molecular Non-Volatile Memory: Application of Redox-Active Molecules. *Appl Sci* **6**, doi:10.3390/app6010007 (2015).

43   Liu, H.-H., Huang, X.-J., Gu, B. & Choi, Y.-K. Alternative route to reconstitute an electrical contact of enzyme on a single-walled carbon nanotube–ferrocene hybrid. *J Electroanal Chem* **621**, 38-42, doi:10.1016/j.jelechem.2008.04.020 (2008).

44   Cao, Q.-Y., Zhang, J. F., Ren, W. X., Choi, K. & Kim, J. S. Ferrocene-based novel electrochemical In3+ sensor. *Tetrahedron Lett* **52**, 4464-4467, doi:10.1016/j.tetlet.2011.06.060 (2011).

45   Labulo, A. H., Ngidi, N. P. D., Omondi, B. & Nyamori, V. O. Physicochemical properties of nitrogen-doped carbon nanotubes from metallocenes and ferrocenyl imidazolium compounds. *J Organomet Chem* **868**, 66-75, doi:10.1016/j.jorganchem.2018.04.033 (2018).

46   Meyer, J., Bredow, T., Tegenkamp, C. & Pfnur, H. Thiol and thiolate bond formation of ferrocene-1,1-dithiol to a Ag(111) surface. *J Chem Phys* **125**, 194705, doi:10.1063/1.2387169 (2006).

47   Gomez Arrayas, R., Adrio, J. & Carretero, J. C. Recent applications of chiral ferrocene ligands in asymmetric catalysis. *Angew Chem Int Ed Engl* **45**, 7674-7715, doi:10.1002/anie.200602482 (2006).

48   Scottwell, S. O. *et al.* Chemically and electrochemically induced expansion and contraction of a ferrocene rotor. *Chem Commun (Camb)* **51**, 8161-8164, doi:10.1039/c5cc01973g (2015).

49   Shao, J.-Y., Cui, B.-B., Tang, J.-H. & Zhong, Y.-W. Resistive memory switching of transition-metal complexes controlled by ligand design. *Coord Chem Rev* **393**, 21-36, doi:10.1016/j.ccr.2019.05.010 (2019).

50   Zhao, R. *et al.* Interlocking Molecular Gear Chains Built on Surfaces. *J Phys Chem Lett* **9**, 2611-2619, doi:10.1021/acs.jpclett.8b00676 (2018).

51   Ullmann, F. & Bielecki, J. Ueber Synthesen in der Biphenylreihe. *Ber Dtsch Chem Ges* **34**, 2174-2185, doi:10.1002/cber.190103402141 (1901).

52   Lackinger, M. Surface-assisted Ullmann coupling. *Chem Commun (Camb)* **53**, 7872-7885, doi:10.1039/c7cc03402d (2017).

53   Fan, Q. *et al.* Surface Adatom Mediated Structural Transformation in Bromoarene Monolayers: Precursor Phases in Surface Ullmann Reaction. *ACS Nano* **12**, 2267-2274, doi:10.1021/acsnano.7b06787 (2018).

54   Wang, W., Shi, X., Wang, S., Van Hove, M. A. & Lin, N. Single-molecule resolution of an organometallic intermediate in a surface-supported Ullmann coupling reaction. *J Am Chem Soc* **133**, 13264-13267, doi:10.1021/ja204956b (2011)

55   Ormaza, M. et al. Assembly of Ferrocene Molecules on Metal Surfaces Revisited. *J Phys Chem Lett* **6**, 395-400, doi:10.1021/jz5026118 (2015).

56   Braun, K. F., Iancu, V., Pertaya, N., Rieder, K. H. & Hla, S. W. Decompositional incommensurate growth of ferrocene molecules on a Au(111) surface. *Phys Rev Lett* **96**, 246102, doi:10.1103/PhysRevLett.96.246102 (2006).

57   Tegenkamp, C., Schmeidel, J. & Pfnür, H. Chemisorption of ferrocene on Si(111)–Ag: Frustrated conformational flexibility. *Surf Sci* **605**, 267-271, doi:10.1016/j.susc.2010.10.027 (2011).

58   Wasio, N. A. et al. Self-assembly of hydrogen-bonded two-dimensional quasicrystals. *Nature* **507**, 86-89, doi:10.1038/nature12993 (2014).

59   Berger, J. et al. Study of Ferrocene Dicarboxylic Acid on Substrates of Varying Chemical Activity. *J Phys Chem C* **120**, 21955-21961, doi:10.1021/acs.jpcc.6b05978 (2016).

60   Muller-Meskamp, L., Karthauser, S., Waser, R., Homberger, M. & Simon, U. Striped phase of mercaptoalkylferrocenes on Au(111) with a potential for nanoscale surface patterning. *Langmuir* **24**, 4577-4580, doi:10.1021/la703504m (2008).

Chapter 3: Research Design

3.1 Surface Theory

3.1.1 Experimental Reasoning

Consider a molecule that functions like a rotor and how it would have this function. σ bonds allow for free rotation about a central bond axis or atom connecting two moieties. The barrier to rotation is dependent on if there are π bonds and other interactions elsewhere in the molecule providing a potential barrier. For a molecule to have rotational degree of freedom all covalent bonds must be stronger than the barrier to rotation. Usually this occurs in single bonds and more rarely occurs in double bonds, this is what makes ferrocene an interesting molecule as a rotor.

Ferrocene's rotation is interesting because it occurs about the central Fe(II) atom, which is bonded to 10 carbon atoms. Its rotational freedom is attributed to the partial covalent bonding between the carbons and iron. The barrier to rotation in gas-phase should be ~0.04 eV[1-3], this is above k_BT at room temperature (0.025 eV) which should mean thermal activation occurs at 460 K (187 °C) or via photonic activation of an equivalent energy. When surface-confined, it is likely to increase the barrier to rotation for the molecule depending on the adsorption geometry. To maintain a reasonable energy barrier, one of the cyclopentadienyl (Cp) rings must not interact with the substrate leaving it free to rotate. Therefore, the ferrocene must be in a vertical orientation. The orientation of ferrocene molecules for this work is defined in chapter 1 (Fig. 1). The surface interacting cyclopentadienyl must interact in such a way that it is bound more strongly than 0.04 eV.

Most surface deposited ferrocene structures form combinations of horizontal and vertical ferrocene moities.[4-8] A possible way to maximise the number of vertically stable ferrocene moieties would be to increase the number of interactions of the surface interacting cyclopentadienyl. This work aims to achieve this by forming organometallic oligomers of ferrocene via Ullmann dehalogenation.

The extensive study and simplification of the Ullmann dehalogenation process helps ease the analysis of the bonding stoichiometry and structures formed. The halogenated ferrocene chosen for this work was 1,1'-dibromoferrocene (DBF) (Fig. 13) for use in the Ullmann reaction. The hope is that DBF will undergo a single dehalogenation event with a surface adatom and orient itself vertically with respect to the surface. STM images of the deposited DBF may be able to confirm the orientation of the molecule by observing circular features for vertical orientation or line-like features for horizontal molecule.[4-6,9] The potential effect of the bromines on the rotational barrier and symmetry of the ferrocene moiety is also consideration and will be addressed using DFT calculations. The inclusion of bromines changes ferrocenes five-fold rotational symmetry with two repeatable staggered-eclipsed conformation into a one-fold symmetric molecule. The point of reference for DBF conformation will be where both bromines are eclipsed referred to as "symmetrically eclipsed".
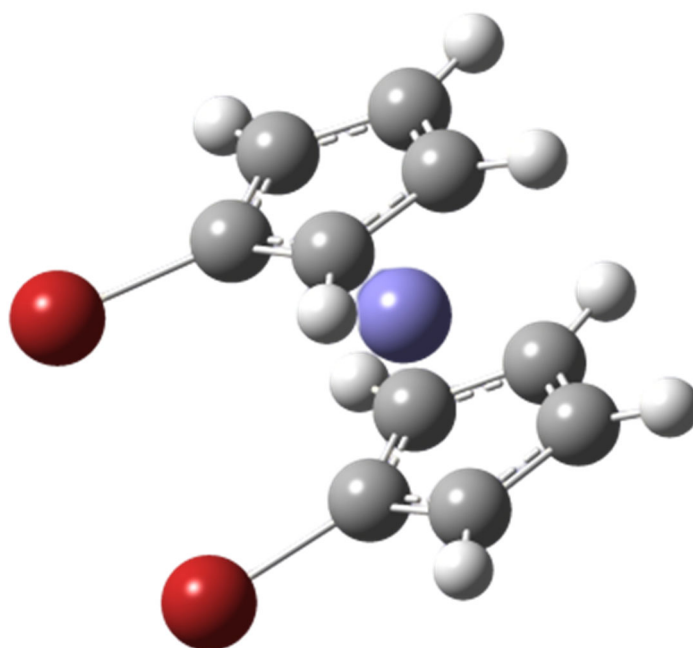
Figure 13: 1,1'-dibromoferrocene in its symmetrically eclipsed conformation

 Preliminary testing of room temperature DBF powder in the Kratos SUPRA UHV XPS system found that DBF is volatile under UHV conditions, allowing the deposition of DBF using dosing line sublimation at room temperature, common to ferrocene-based molecules (See section 2.6). While this deposition technique is simple it may not provide the desired molecular geometry upon adsorption. It is possible that deposition methods may alter the energetics of the incident molecules and could influence the final surface structure.

Density functional theory (DFT) calculations allow the simulation of molecular mechanics, to determine the total energy of a system, molecular bond lengths, adsorption geometry and much more. DFT was used to assist in confirmation of initial assumptions about the potential of ferrocene as molecular rotor. The barrier to rotation for gas-phase ferrocene and dibromoferrocene will be calculated and validated against previous work on ferrocene's rotational barrier. Calculations of surface deposited ferrocene will also be simulated to determine potential adsorption geometries, the potential of vertically oriented ferrocene and the effect of surface adsorption on ferrocene's rotational barrier.

3.1.2 Substrate

In surface science some common materials used as single crystal substrates are copper, silver and gold.[10-15] These materials are all noble metals, a select few materials that all have a full d-shell. What makes copper, silver, and gold significant as substrates is the single unpaired s-shell electron they each possess, leaving a gap for only one electron to pair with[16], a single covalent bond. Gold and silver's $5s^1$ and $6s^1$ orbitals both undergo relativistic orbit contraction. However, gold's $6s^1$ orbital distance is contracted significantly more towards the 5d than silvers $5s^1$ orbital, leading to greatly reduced reactivity[17]. Silver and copper make good catalysts, and gold a useful relatively inert surface. Copper's 1.5 eV higher Fermi energy and smaller relativistic effects make it significantly more reactive, meaning it can sometimes cause deposited organic molecules to dissociate.

Surface reactivity is also affected by the crystallographic orientation of the substrate. Crystallographic orientations (crystallographic planes) are described by the Miller indices of a single crystal (Fig. 14), where each facet presents a different atomic pattern with a different atomic coordination number. These patterns affect the surfaces energetics where the surface tension and reactivity change depending on the atomic coordination.

(111)   (100)   (110)
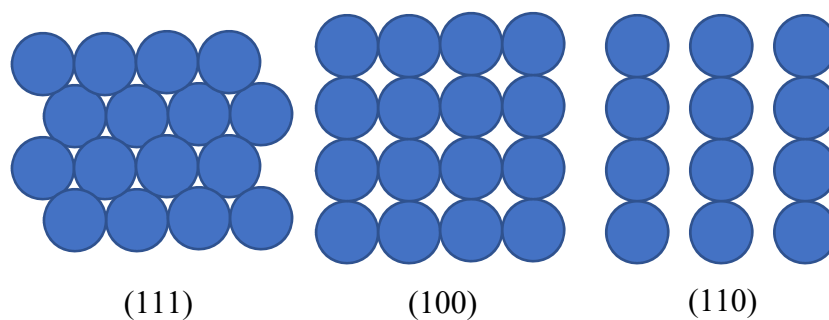
Figure 14: The three primary cubic crystallographic planes

The close packed structure of the (111) plane has the highest coordinated atoms with twelve equidistant neighbours in 3D space, six in 2D space and nine considering a surface atom. Of the low-index facets, it has the highest packing constant, three-fold symmetry and the lowest reactivity. The most reactive facet and the least coordinated is the (110) plane with the (100) plane falling in-between. Using different planes is a good way to finely control the surface to obtain a desired reactivity of the material[18]. These orientations also sterically affect the geometry of adsorbed molecules. Step edges and adatoms that have lower coordination due to the reduction in nearest neighbours also significantly increase the reactivity of the surface [19-22].

3.2 Characterisation and Analysis Techniques

3.2.1 Scanning Tunnelling Microscopy

The probabilistic effect of quantum tunnelling, where electrons can pass through a potential barrier, can be used to image surfaces on the atomic scale in scanning tunnelling microscopy. This technology is highly useful as it allows the direct observation of surface structure that can show the physical changes that occur after some form of processing, i.e. molecular deposition, or annealing.

An STM has a metallic tip that ideally comes down to a single atom point. This tip is brought very close to a surface with picometer control from a piezoelectric scanner. A bias voltage (V) is placed between the metallic tip and the sample providing energy to electrons that will then tunnel to the sample from the tip or vice versa depending on the polarity of the voltage. This tunnelling will induce a current (I) that is recorded as a function of the tip's vertical and horizontal position (Fig. 15). The STM system will then attempt to keep either a constant vertical position or a constant tunnelling current, depending on the operating mode.
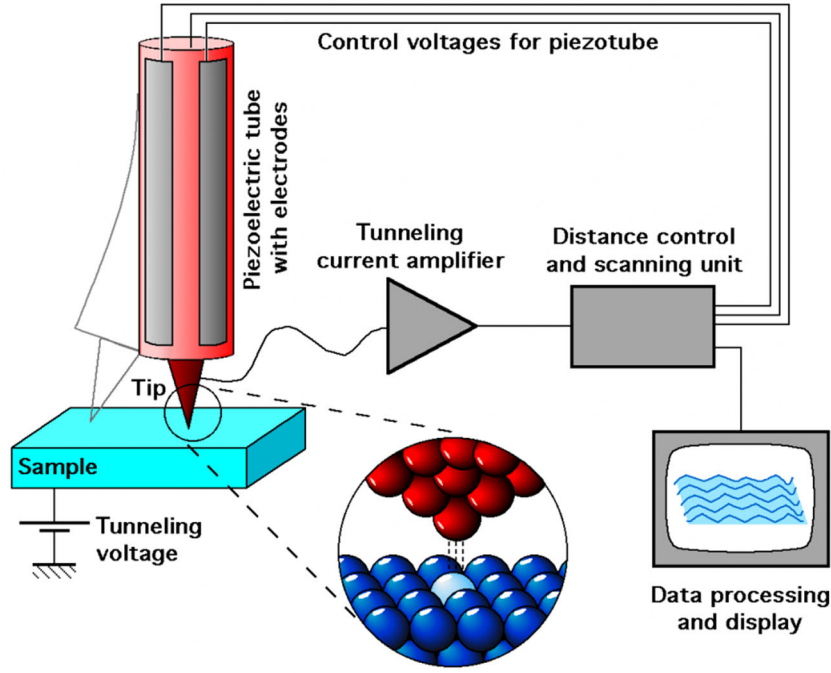
Figure 15: Diagram by Michael Schmid, TU Wien, showing the main equipment and process involved in producing an image via STM. Tip position and current are recorded as individual lines that are then stacked to produce images. *Figure by Michael Schmid, TU Wien (2011), licensed under CC BY-SA 2.0 AT (https://creativecommons.org/licenses/by-sa/2.0/)* [23]

Quantum tunnelling is a direct effect of the wave-like nature of electrons and therefore must be contextualised with the use of wave equations. The bias voltage is a function of the tunnelling probability, I, given by equation 1 with the assumptions that the tunnelling matrix, M, that describes the effect of distance between the tip and surface, remains constant

$$I = \frac{4\pi e}{\hbar} \int_{-\infty}^{\infty} [f(E_F - eV + \epsilon) - f(E_F + \epsilon)] \times \rho_A(E_F - eV + \epsilon)\rho_B(E_F + \epsilon)|M|^2 d\epsilon, \qquad (1)$$

where $f(E)$ is the Fermi distribution function, E_F is the Fermi energy of the material, V is the bias voltage, ϵ is the electron energy, $\rho_A(E)$ and $\rho_B(E)$ are the density of states for the surface (A) and the tip (B). When $k_B T$ less than the energy resolution of the measurement and assuming negligible change to the matrix element ($|M|$) in the energy interval of interest, the tunnelling current, equation 1, depends only on the density of states of the surface and tip.[24]

In constant current mode, the tunnelling current is set within the range of 10 nA to 10 pA and is kept constant by the control system varying the distance of the tip from the surface. This vertical change as the tip scans horizontally is recorded and plotted. These line plots get stacked to produce an image of the surface. Finding the right bias voltage, current set point

and feedback while managing vibrational noise is challenging, but when successful the output images are very useful. However, STM images are also quite challenging to analyse requiring, supplementary data from additional instrumentation, image analysis tools and an experienced operator. These images can be used to directly measure atomic distances and find periodicities in the structure (Fig. 16).
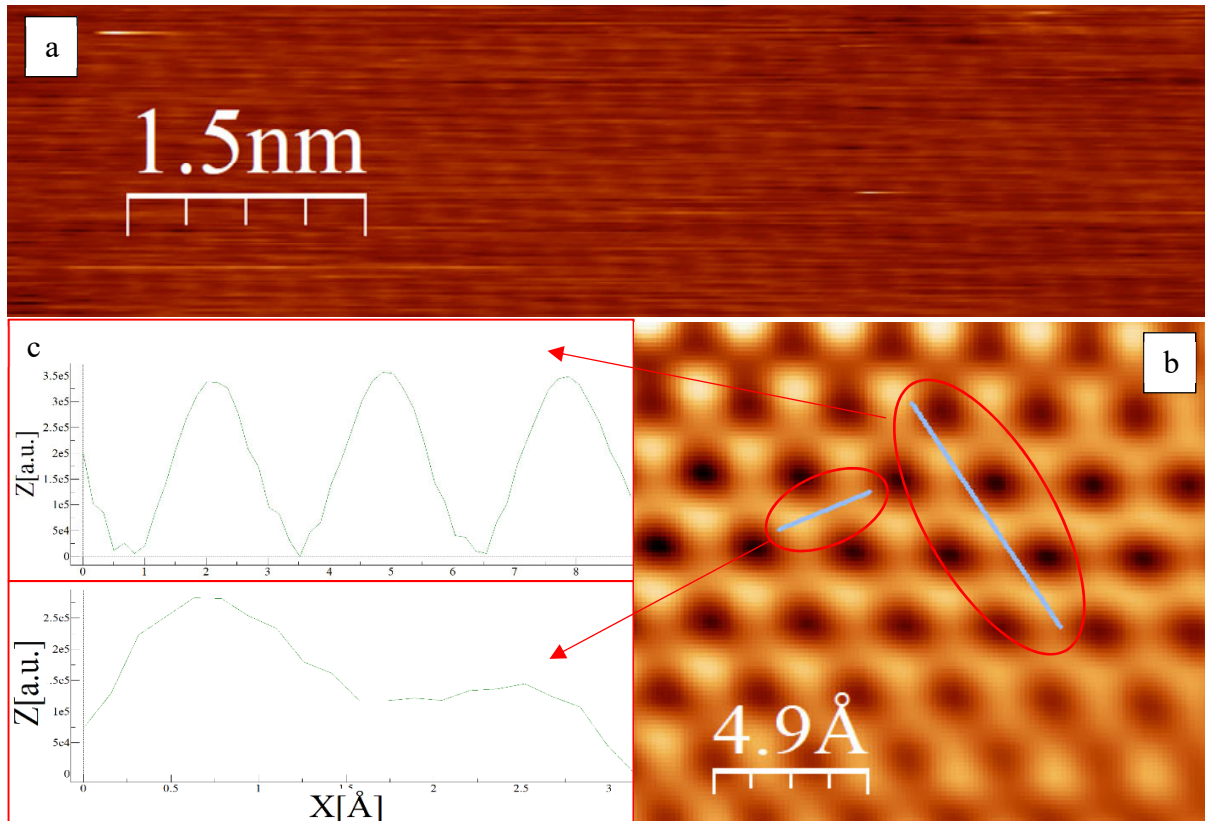
Figure 16: a) An example of an STM image of clean Ag(111), b) an FFT filtered version of 'a', used to measure c) atomic distances between top layer atoms and height differences between the top layer and the layer below.

3.2.2 X-ray Photoelectron Spectroscopy

The adsorption of photons and subsequent release of electrons from a material, known as the photoelectric effect, can be used to determine the binding energy (E_B) of an electron. The electron binding energy depends on many factors such as the orbital state occupied by the electron, the effective nuclear charge, the electronegativity of surrounding elements, and bonds formed with the surrounding atoms. Therefore, determining the electron binding energy for a given core level can provide great insights to a materials bonding stoichiometry. When a known photon energy (E_P) is incident on a surface any electrons released to vacuum will have a total kinetic energy (E_K) that can be recorded with a detector. The difference between photon energy and total kinetic energy describes how much energy was required for that electron to escape to vacuum. When an electron is given more energy than its binding

energy it first becomes a free electron. The work function (φ) of a material is the energy required to excite a free electron from the Fermi level to vacuum. This system of energies, the photoelectric effect, can be described as

$$E_P - E_K = \varphi + E_B. \quad (2)$$

The recorded electron counts, E_K and equation 2 are then used to create a spectrum of counts vs. E_B that shows characteristic peaks for each element at certain E_B relating to the core levels. As mentioned above electron binding energies are sensitive, chemical shifting and therefore so are the characteristic peaks. As such we can deconvolute the recorded peaks, with respect to the peaks expected to be found from predicted reactions and known bonding, determining the surface stoichiometry of deposited molecules.

In photoelectron spectroscopy both monochromatic and chromatic x-ray sources can be used. In each case, the photon energy is dependent on the source emitter material. The usual types of emitter (anode) material used to produce X-ray radiation are magnesium and aluminium. The anode material is significant for non-monochromated sources because of the spread of photon energies released, from ~0.01 nm to ~0.1 nm, due to the Bremsstrahlung effect and the characteristic K_α and K_β peaks. These can influence the recorded spectra, with Bremsstrahlung X-rays increasing background electron counts and causing secondary orbital peaks that can overlap with a desired peak. However, QUT's Omicron UHV system can switch between either an Al or Mg anode source (Fig. 17). This functionality enables the identification of Auger peaks that have a constant E_K in XPS.
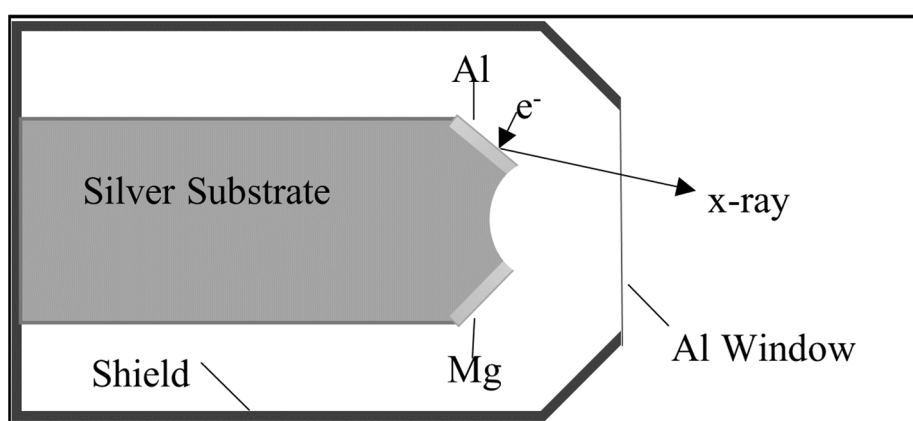
Figure 17: Twin anode chromatic X-ray source. The electrons come from filaments above the Al and Mg surfaces, and the shield is grounded.

Monochromated x-rays do not have this issue with the spread of photon energies as only one characteristic peak is incident on the sample. Monochromatic sources are also more precisely targeted due to being refracted and not simply columnated. This allows the irradiation of

specific points on a sample, as opposed to the wide beam of x-rays you get from a non-monochromatic source. However, they are limited to a single fixed source, commonly aluminium, and are much bulkier instruments.

To chemically characterise the deposition of DBF onto Ag(111), XPS was performed immediately after deposition with Al Kα source (1486.87 eV) with 4 mA emission current, 15kV charged anode, 50 eV pass energy and -1 eV step size for survey spectra and 15 mA emission current, 20 eV pass energy and -0.1 eV step size for high resolution spectra.

3.2.3 Near edge x-ray absorption fine structure

Near edge x-ray absorption fine structure (NEXAFS) is a powerful synchrotron technique for characterising the unoccupied molecular orbitals of a surface-deposited molecule. Polarised monochromatic x-ray radiation is incident on a surface of interest. The x-rays excite core orbital electrons that transition into unoccupied π, σ and Rydberg orbitals. Upon relaxation photons, electrons and inelastic electrons are released.[25,26] The released photons are then detected and plotted against their recorded energy (Fig. 18).
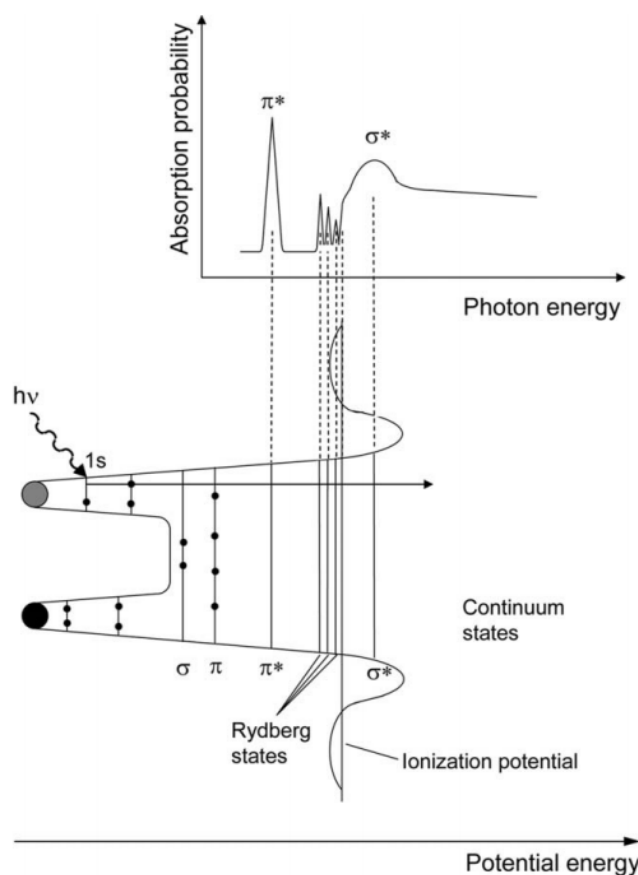
Figure 18: Visualisation of the general XANES mechanism. *Used with permission of Royal Society of Chemistry, from Hahner, G. Near edge X-ray absorption fine structure spectroscopy as a tool to probe*

Using polarised synchrotron radiation and the NEXAFS technique, molecular adsorption orientations can be determined by varying the angle of x-ray incidence. Due to quantum mechanical effects electron orbitals have shapes that are directional. This means the highest excited state available to an electron in a certain orbital is also directional[26]. π* and σ* orbitals are ideally perpendicular to one another in a molecule. By aligning the electric field of the polarised x-rays' angle of incidence parallel to a π* or σ* orbital, there is more opportunity for electron interactions with the electric field. The larger number of relaxing electrons will therefore produce more photon peak when the X-ray beam is perpendicular to the orbital, and less intense when parallel to it (Fig. 19).
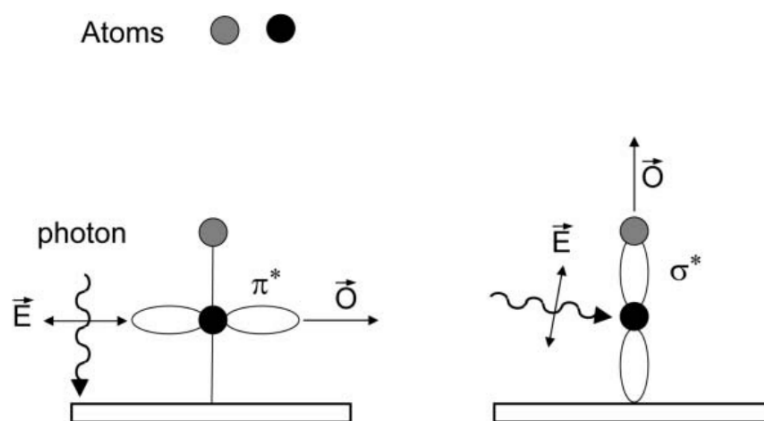
Figure 19: Visualisation of the NEXAFS technique with polarised x-rays perpendicular to, or similarly E-field parallel to, visualised orbitals. *Used with permission of Royal Society of Chemistry, from Hahner, G. Near edge X-ray absorption fine structure spectroscopy as a tool to probe electronic and structural properties of thin organic films and liquids. Chem Soc Rev 35, 1244-1255, doi:10.1039/b509853j (2006); permission conveyed through Copyright Clearance Center, Inc.*

The transition intensity from a 1s initial state to a final state, dependent on the orientation of linearly polarised incident light, can be described as

$$I \propto \left| e \langle \Psi_f | \mathbf{P} | \Psi_i \rangle \right|^2 \propto |e\mathbf{O}|^2 \propto \cos^2 \delta. \qquad (3)$$

Where signal intensity (I) is proportional to the square of the magnitude of the average momentum ($\mathbf{P}$) of the initial and final wave function (Ψ_i) and (Ψ_f) respectively, is proportional to the square of the magnitude of the final orbital state ($\mathbf{O}$) is proportional to the cosine squared of the angle of incidence[26].

For a substrate symmetry of threefold or higher, at an incidence angle (θ) or planar rotation (α) of 54.7° to the surface norm, with a perfectly polarised X-ray beam, the measured signal intensity distribution for both a planar orbital and vector orbital becomes independent of the molecular orientation.

$$I_{Vector}^{\parallel} = \frac{1}{3}\left[1 + \frac{1}{2}(3cos^2\theta - 1)(3cos^2\alpha - 1)\right] \qquad (4)$$

$$I_{Planar}^{\parallel} = \frac{2}{3}\left[1 - \frac{1}{4}(3cos^2\theta - 1)(3cos^2\gamma - 1)\right] \qquad (5)$$

This also means that if there is no change in signal intensity distribution with changing angle of incidence, the molecular orientation will be found to be 54.7° to the surface norm. This is known as the "magic angle", where molecular orientation and its intensity distribution are indistinguishable from random molecular orientation[27].

3.3 Density Functional Theory

Density functional theory is a computational framework for solving Schrodinger's equation for a many body system via various exchange-correlation approximations. These simulations can describe the intramolecular energies and distances, the electronic band structure of a material and the density of states for a given molecule. Using this method, it is possible to determine things such as the activation energy of a rotational degree of freedom. It is also possible to approximate adsorption sites of a surface interacting molecule, then compare the total energy of the different sites. Using these techniques can assist in the rationalisation of an experimental data, as well as the prediction of other currently unknown phases.

DFT uses functionals of atomic electron densities to determine interatomic electron energetics as an approximation of solving the time-independent Schrödinger equation for each electron functional. However, achieving a solution for this is not a simple task as the functional for exchange-correlation (EC) is not known[28]. This is because while the exchange energy can be exactly determined computationally, the correlation energy is the effect of the proximity of all electrons on each other simultaneously. If the exact position of one electron is calculated its motion would become unknown and no longer allow the exact calculation of the position of electrons within its proximity. To solve this issue DFT uses various approximations for EC that have been formulated, each with their advantages and drawbacks. The large number (>200) of functionals available provides a challenge when choosing which to use. For complex molecules semi-empirical functionals are required due to non-empirical

forms only fitting simpler systems. The approximation used in this work to investigate the rotational barrier of ferrocene and dibromoferrocene was the B3LYP hybrid functional, see section 4.2 for more details.

This work uses DFT to find the optimised structures of gas-phase ferrocene and dibromoferrocene. These optimised structures were then used to generate isomers rotated in 6-degree increments for single point energy calculations. The resulting potential map can then be used to determine the global maximum and minimum barrier to rotation. These calculations were performed in Gaussian09[29]. DFT calculations require large amounts of computational power, such that supercomputers are a requirement. QUT's supercomputer cluster "Lyra" was used to run the Gaussian software package.

To find the rotational potential barrier (E_B) of ferrocene, the total molecular energy of an initial optimised structure (E_0) is subtracted from the total molecular energy of the same structure with a rotated aromatic ring (E_R). $E_B = E_R - E_0$, this evaluation describes a barrier at a known rotation. For ferrocene, the angle between molecularly equal isomers is 72-degrees due to the cyclopentadienyl rings. This means the barrier to rotation for each 72-degree rotation in a 360-degree rotation should be equal. For dibromoferrocene the added halogens decrease the symmetry of the isomers, where a 180-degree map will be required to form a full 360-degree map. This should assist in determining the requirements for rotational activation for ferrocene and dibromoferrocene.

This work also uses the Quantum Espresso (QE) system to determine surface adsorption geometries of ferrocene. Previously optimised ferrocene and Ag(111) atomic coordinates were combined in QE, using the Born-Oppenheimer Molecular Dynamics functional in the PWscf package and Plane-Wave basis set. Ferrocene was placed in a vertical and a horizontal orientation with an arbitrary starting position in the centre of the surface. These geometry optimisations were then intended to be expanded on and used to rationalise and support experimental results from STM images.

3.4 References

1   Sorriso, S. Energy barrier to internal rotation in some ferrocene derivatives from dielectric measurements. *J Organomet Chem* **179**, 205-213, doi:10.1016/s0022-328x(00)95223-9 (1979).

2   Phillips, L. *et al.* The molecular structure, equilibrium conformation and barrier to internal rotation in decachloroferrocene, Fe(eta-C(5)Cl(5))(2), determined by gas electron diffraction. *Dalton Trans* **39**, 4631-4635, doi:10.1039/c001366h (2010).

3   Almenningen, A. *et al.* The molecular structure of decamethylferrocene studied by gas phase electron diffraction. Determination of equilibrium conformation and barrier to internal rotation of the ligand rings. *J Organomet Chem* **173**, 293-299, doi:10.1016/s0022-328x(00)84784-1 (1979).

4   Berger, J. *et al.* Study of Ferrocene Dicarboxylic Acid on Substrates of Varying Chemical Activity. *J Phys Chem C* **120**, 21955-21961, doi:10.1021/acs.jpcc.6b05978 (2016).

5   Ormaza, M. *et al.* Assembly of Ferrocene Molecules on Metal Surfaces Revisited. *J Phys Chem Lett* **6**, 395-400, doi:10.1021/jz5026118 (2015).

6   Wasio, N. A. *et al.* Self-assembly of hydrogen-bonded two-dimensional quasicrystals. *Nature* **507**, 86-89, doi:10.1038/nature12993 (2014).

7   Müller-Meskamp, L. *et al.* Molecular structure of ferrocenethiol islands embedded into alkanethiol self-assembled monolayers by UHV-STM. *physica status solidi (a)* **203**, 1448-1452, doi:10.1002/pssa.200566148 (2006).

8   El Garah, M. *et al.* Molecular design driving tetraporphyrin self-assembly on graphite: a joint STM, electrochemical and computational study. *Nanoscale* **8**, 13678-13686, doi:10.1039/c6nr03424a (2016).

9   Tegenkamp, C., Schmeidel, J. & Pfnür, H. Chemisorption of ferrocene on Si(111)– Ag: Frustrated conformational flexibility. *Surf Sci* **605**, 267-271, doi:10.1016/j.susc.2010.10.027 (2011).

10   Lischka, M. *et al.* Competitive Metal Coordination of Hexaaminotriphenylene on Cu(111) by Intrinsic Copper Versus Extrinsic Nickel Adatoms. *Chem* **25**, 1975-1983, doi:10.1002/chem.201803908 (2019).

11   Shao, J.-Y., Cui, B.-B., Tang, J.-H. & Zhong, Y.-W. Resistive memory switching of transition-metal complexes controlled by ligand design. *Coord Chem Rev* **393**, 21-36, doi:10.1016/j.ccr.2019.05.010 (2019).

12   Rodriguez, L. M. *et al.* Building two-dimensional metal-organic networks with tin. *Chem Commun (Camb)* **55**, 345-348, doi:10.1039/c8cc08280d (2019).

13   Lovat, G. *et al.* Determination of the structure and geometry of N-heterocyclic carbenes on Au(111) using high-resolution spectroscopy. *Chem Sci* **10**, 930-935, doi:10.1039/c8sc03502d (2019).

14   Zhao, R. *et al.* Interlocking Molecular Gear Chains Built on Surfaces. *J Phys Chem Lett* **9**, 2611-2619, doi:10.1021/acs.jpclett.8b00676 (2018).

15   Lipton-Duffin, J., Abyazisani, M. & MacLeod, J. Periodic and nonperiodic chiral self-assembled networks from 1,3,5-benzenetricarboxylic acid on Ag(111). *Chem Commun (Camb)* **54**, 8316-8319, doi:10.1039/c8cc04380a (2018).

16   Reimers, J. R., Ford, M. J., Halder, A., Ulstrup, J. & Hush, N. S. Gold surfaces and nanoparticles are protected by Au(0)-thiyl species and are destroyed when Au(I)-thiolates form. *Proc Natl Acad Sci U S A* **113**, E1424-1433, doi:10.1073/pnas.1600472113 (2016).

17   Pyykko, P. & Desclaux, J. P. Relativity and the periodic system of elements. *Acc. Chem. Res.* 12, 276-281, doi: 10.1021/ar50140a002 (1979).

18   Peljhan, S. & Kokalj, A. DFT study of gas-phase adsorption of benzotriazole on Cu(111), Cu(100), Cu(110), and low coordinated defects thereon. *Phys Chem Chem Phys* **13**, 20408-20417, doi:10.1039/c1cp21873e (2011).

19   Zhao, Z., Chen, Z., Zhang, X. & Lu, G. Generalized Surface Coordination Number as an Activity Descriptor for CO2 Reduction on Cu Surfaces. J *Phys Chem C* **120**, 28125-28130, doi:10.1021/acs.jpcc.6b10155 (2016).

20   Pedio, M., Cepek, C. & Felici, R. Organic molecules on noble metal surfaces: the role of the interface. *Noble Metals, Yen-Hsun Su, IntechOpen*, doi:10.5772/34551 (2012).

21   Kiskinova, M. Surface Structure and Reactivity: Reactions on Face-Centered Cubic (110) Metal Surfaces Involving Adatom-Induced Reconstructions. *Chem Rev* **96**, 1431-1448, doi:10.1021/cr950226y (1996).

22   Lin, R. *et al.* Quantitative Study of Charge Carrier Dynamics in Well-Defined WO3 Nanowires and Nanosheets: Insight into the Crystal Facet Effect in Photocatalysis. *J Am Chem Soc* **140**, 9078-9082, doi:10.1021/jacs.8b05293 (2018).

23   Schmid, M. *The Scanning Tunneling Microscope*, <http://www.iap.tuwien.ac.at/www/surface/stm_gallery/stm_schematic> (2011).

24   Chen, C. J. *Introduction to Scanning Tunneling Microscopy*. (2007).

25   Lenhart, J. L. *et al.* X-ray absorption spectroscopy to probe surface composition and surface deprotection in photoresist films. *Langmuir* **21**, 4007-4015, doi:10.1021/la047160z (2005).

26   Hahner, G. Near edge X-ray absorption fine structure spectroscopy as a tool to probe electronic and structural properties of thin organic films and liquids. *Chem Soc Rev* **35**, 1244-1255, doi:10.1039/b509853j (2006).

27   Stöhr, J. *NEXAFS Spectroscopy.* (1992).

28   Precechtelova, J., Bahmann, H., Kaupp, M. & Ernzerhof, M. Communication: A non-empirical correlation factor model for the exchange-correlation energy. *J Chem Phys* **141**, 111102, doi:10.1063/1.4896057 (2014).

29   Frisch, M. J., Trucks, G. W., Schlegel, H. B., Scuseria, G. E., Robb, M. A., Cheeseman, J. R., Scalmani, G., Barone, V., Petersson, G. A.. Nakatsuji, H., Li, X., Caricato, M., Marenich, A. V., Bloino, J., Janesko, B. G., Gomperts, R., Mennucci, B., Hratchian, H. P., Ortiz, J. V., Izmaylov, A. F., Sonnenberg, J. L., Williams, Ding, F., Lipparini, F., Egidi, F., Goings, J., Peng, B., Petrone, A., Henderson, T., Ranasinghe, D., Zakrzewski, V. G., Gao, J., Rega, N., Zheng, G., Liang, W., Hada, M., Ehara, M., Toyota, K., Fukuda, R., Hasegawa, J., Ishida, M., Nakajima, T., Honda, Y., Kitao, O., Nakai, H., Vreven, T., Throssell, K., Montgomery Jr., J. A., Peralta, J. E., Ogliaro, F., Bearpark, M. J., Heyd, J. J., Brothers, E. N., Kudin, K. N., Staroverov, V. N., Keith, T. A., Kobayashi, R., Normand, J., Raghavachari, K., Rendell, A. P., Burant, J. C., Iyengar, S. S., Tomasi, J., Cossi, M., Millam, J. M., Klene, M., Adamo, C., Cammi, R., Ochterski, J. W., Martin, R. L., Morokuma, K., Farkas, O., Foresman, J. B., Fox, D. J. Gaussian 16 Rev. B.01. (2016).

30   Giannozzi, P. et al. QUANTUM ESPRESSO: a modular and open-source software project for quantum simulations of materials. J Phys Condens Matter 21, 395502, doi:10.1088/0953-8984/21/39/395502 (2009).

Chapter 4: Gas-phase DFT of ferrocene and dibromoferrocene rotational barriers and XPS characterisation of dibromoferrocene powder

4.1 Introduction

The properties of ferrocene and dibromoferocene this chapter investigates are the barrier to rotation in the internal degree of freedom, physical geometry, molecular bonds of DBF through the XPS of unreacted powder, and surface geometry of ferrocene on Ag(111). Barriers to rotation and structural optimisations determined by DFT were tabulated and compared to published results where possible. The same analysis was done on dibromoferrocene along with XPS analysis of unreacted powdered DBF. The DFT data calculated in this chapter on ferrocene and dibromoferocene, as well as the XPS spectra of powdered dibromoferrocene, are compiled to assist in the analysis of surface deposited DBF.

4.2 Methods

Gas-phase optimisations were performed using the Gaussian09 software[1] and GaussView visualiser to perform DFT optimisations of ferrocene and dibromoferrocene using the B3LYP functional and 3-21G basis set. The B3LYP hybrid functional was used as it is currently one of, if not the most, widely used and accepted functionals stemming from work done in highly cited papers[2] and because it includes a computed exchange correlation, which has been shown in other works as required to achieve good agreement with ferrocenes experimental results[3]. B3LYP offers an effective compromise between computation speed and the inclusion of a computed exchange term[4]. The split valance 3-21G and polarised 6-31G(d,p)[5] basis sets were chosen for two independent optimisation runs. Initially, 3-21G was used for simplicity's sake with the assumption that the DBF and ferrocene orbitals do not change shape. Then the 6-31G(d,p) basis set was chosen due to the Fe(II) core's strong electronic interactions with the surrounding carbon rings. Optimisations were stopped with gradients smaller than 0.0155 eV/Å because this is Gaussian's default convergence criterion based on standard benchmarking.

To calculate the rotational barrier, the single point energies for ferrocene and dibromoferrocene were calculated from an initial geometry optimised model. One of the single cyclopentadienyl rings was rotated 360° for ferrocene and dibromoferrocene in 6° increments. These were used to determine the barrier to rotation as well as visualise the rotational energy barrier landscape by plotting out the difference in total energy as a function of rotated angle. These calculations were also performed in Gaussian09 using GaussView to

set up the jobs, rotations were then performed by applying a rotational matrix to the job file coordinates. The optimised distances, energy barriers and dipole moments are tabulated below and have been compared to those found in the literature.

Surface adsorption geometry calculations were performed using the Quantum Espresso system[6] using the Born-Oppenheimer Molecular Dynamics functional in the PWscf package with the Plane-Wave basis set. Initial calculations were done with a staggered conformation ferrocene placed in a vertical and horizontal orientation in an arbitrary starting position centred on a top later silver molecule. Geometry optimisations were intended to act as support for ferrocene as a surface confined nanorotors as well as rationalise and support experimental results from STM images.

XPS was performed in the Kratos SUPRA UHV XPS system with a base pressure of $\sim 10^{-8}$ mbar using a monochromated Al source (1486.87 eV). As-received DBF powder was prepared under atmosphere by placing a small amount onto carbon tape. Dibromoferrocene was found to be volatile under UHV conditions at room temperature, so the powder sample was chilled during XPS. High resolution spectra of C 1s (300 – 270 eV), Fe 2p (740 – 695 eV) and Br 3p (205 – 165 eV) peaks were produced with a total X-ray exposure time of 20 minutes, 0.1 eV step size and 20 eV pass energy, then analysed using the CasaXPS analysis software[7]. This was intended to determine the stoichiometry of the as-received DBF and provide a baseline for comparison with deposition experiments.

4.3 Results and Discussion

4.3.1 Gas-Phase DFT of ferrocene and dibromoferrocene

The potential barrier maps produced for ferrocene and dibromoferrocene using 3-21G and 6-31G(d,p) (Fig. 20), suggest that ferrocene has a barrier of 0.028/0.015 eV and dibromoferrocene 0.053/0.044 eV respectively. The dibromoferrocene maps both clearly illustrate how the functionalisation of ferrocene can significantly affect the rotational barrier. Surface confined ferrocene would no doubt also have a higher rotational barrier assuming these maps are accurate. Interestingly the functionalisation of both Cp rings appears to form a potential well in the symmetrically eclipsed conformation where the halogens are eclipsed with one another. This is despite the expectation that the halogens should repel one another and is contrary to past works with halogen functionalised ferrocene, that show an expected peak when eclipsed and trough when staggered mirroring the map of ferrocene[8]. The inclusion of orbital polarisation and 3 additional gaussian functions in 6-31G(d,p) appears to

draw out two more symmetrical local minima positions that do roughly match a minima in the ferrocene barrier. This may suggest that the bromines may be interacting with the delocalised states of the carbon rings increasing the molecular stability.

The rotational barriers (Fig. 20) were produced by taking the raw data total energy data of ferrocene or DBF (Fig 21) and subtracting the smallest total energy from the total energy of each separate 6° rotation of the same molecule. This energy difference is the energy barrier for the molecule to reach that conformational position.
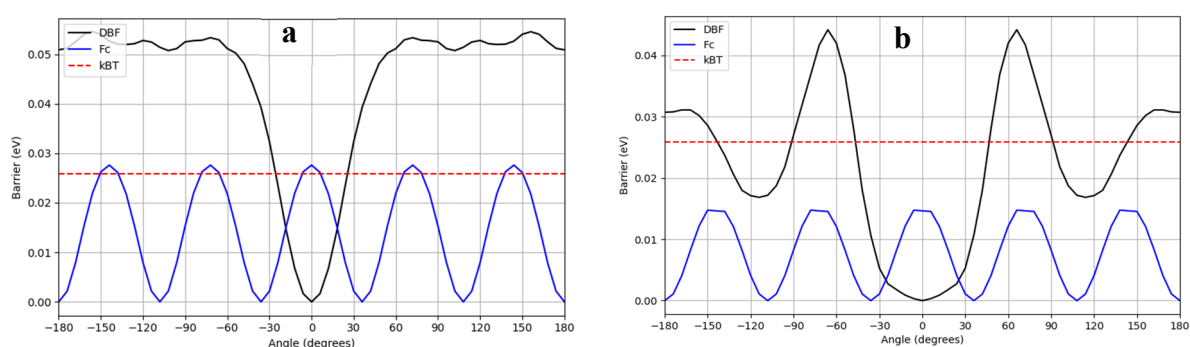
Figure 20: Rotational potential barrier maps of ferrocene (eclipsed) at 0° and dibromoferrocene (symmetrically eclipsed) at 0°, rotated 180°, using basis sets a) 3-21G b) 6-31G (d,p)

The rotational barrier found for ferrocene with the 6-31G(d,p) basis set (0.015 eV) is significantly lower than published experimental rotational barrier results 0.03954 - 0.04336 eV[8,9]. While the rotational barrier found using the smaller 3-21G basis set (0.028 eV) was still lower than published results it is surprising that the smaller basis produced results closer to the expected values[8], however the opposite is true for DBF.

The heart of DFT is the electron density functional[10]

$$E[\rho] = \int v(r)\rho(r)dr + J(\rho) + T_s(\rho) + E_{XC}(\rho), \tag{6}$$

where $E[\rho]$ is the total molecular energy with respect to the electron density ρ, $\int v(r)\rho(r)dr$ is the Coulombic repulsion between electrons-nuclei and electrons-density, $J(\rho)$ is the Coulombic energy relating to the internal repulsion in the electron density itself, $T_s(\rho)$ is an approximated electronic kinetic energy term and $E_{XC}(\rho)$ is the electron exchange-correlation functional that in this work, using the B3LYP functional, is a computed term.

Transition metal compounds are already a significant challenge to model in DFT due to their large number of mobile electrons, and their stronger bonds which scale the error in electron correlation[11]. With ferrocene being a uniquely stable organometallic structure with strong Fe(II) organometallic interactions, the internal electron density repulsion $J(\rho)$ may be

overestimating the energy in the staggered conformation, as the B3LYP functional does not provide dispersion correction. Another explanation could be the B3LYP functional exchange interaction. This can be seen in the raw data from the calculations where molecular energy varies less between conformations for the Fc, with a bigger basis set. In the dibromoferrocene map, this leads to the appearance of another significant minimum position at 114°.

Ferrocene's stable states are found on average to be staggered[12], where the staggered state is the global minimum for ferrocene and the eclipsed conformation is the global maximum (Fig. 20-21). This has been confirmed in both potential maps produced in this work, so it is likely that the shape of the potential barriers are correct. Ferrocene can also be metastable in the eclipsed formations. The barrier of partially dibrominated dibromoferrocene may be similar to the dibromoferrocene barrier, although perhaps lower due to the reduced angular momentum from lack of a bromine mass. However, the Br-Br interaction that is assumed to cause the significant energy well in dibromoferrocene may be replaced by a potentially larger steric barrier caused by electrostatic forces of Br interacting with the undercoordinated C atom.

As mentioned previously ferrocene's rotational barrier contrasts with dibromoferrocene's which has its global minima in its symmetrically eclipsed conformation (Fig. 20-21). Both barriers were higher than the published experimental result for the barrier (Table 1). Past work shows that the rotational barrier for ferrocene should be higher than dibromoferrocene. Based on this and the underestimation of the $J(\rho)$ component, the basis sets used do not produce energetically accurate models of the ferrocene moiety. Smaller basis sets that do not include electron correlation cannot get to an appropriate level of agreement with experimental results either, due to the significant stabilisation from attractive dispersion interactions. It the therefore surprising when considering the smaller 3-21G basis set for ferrocene that does not include orbital polarisation managed to compute a rotational barrier of 0.02761 eV, closer to the experimental results than the 6-31G(d,p) set.

Table 1: Molecule Specifications of ferrocene and dibromoferrocene at global positions.

Molecule Orientation	B3LYP	Ferrocene Global Minima	Ferrocene Global Maxima	DBF Global Minima	DBF Global Maxima
	3-21G	0.0037	0.0004	3.3583	2.8354

Dipole moment (Debye)	6-31G (d,p)	0.0012	0.0001	4.1372	3.5014
Ring-to-ring distance (nm)	3-21G	0.334		0.321-0.391	0.333-0.355
	6-31G (d,p)	0.33		0.327-0.334	0.328-0.331
Ring diameter (nm)	3-21G	0.233		0.230	
	6-31G (d,p)	0.233		0.230	
Rotational barrier (eV) (this work)	3-21G	0.02761		0.05333	
	6-31G (d,p)	0.01529		0.04415	
Rotational barrier (eV) (published)	experimental	0.03954 - 0.04336 (Ref. 8,9)		0.03686 (Ref. 13)	
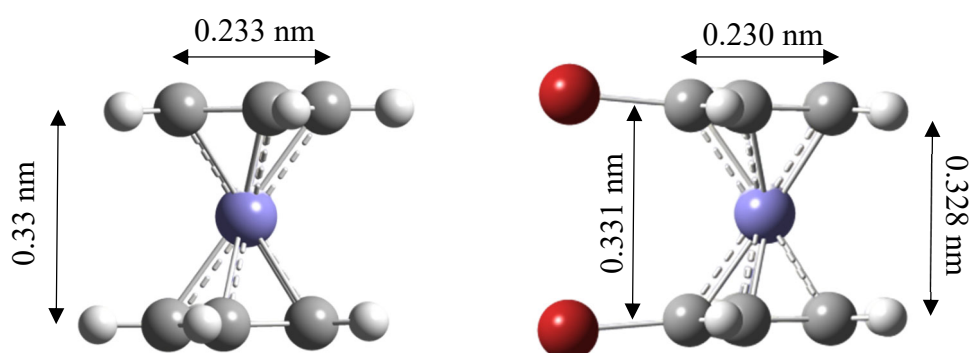
Figure 21: Visualisation of Ferrocene (staggered conformation) and DBF (symmetrically eclipsed conformation) measurements, produced using GuassView

Based on the experimental value for rotational activation energy of both ferrocene and dibromoferrocene, the barriers are greater than the ambient energy, k_BT (0.02586 eV) at room temperature (~300 K). To thermally activate ferrocene would require ~10 K of heating above room temp (310 K) and dibromoferrocene would need at least ~100 K of heating above room temp (400 K). Photonic activation should also be possible with infrared photons, suggesting that both molecules will be rotationally active under most conditions.

4.3.2 DFT of surface adsorbed ferrocene geometry

DFT optimisation and energy calculations of ferrocene and dibrominated dibromoferrocene on surface are useful for determining adsorption sites. For vertically adsorbed ferrocene the
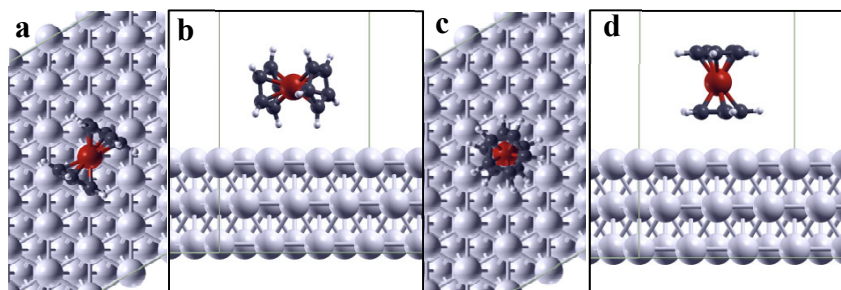
Figure 22: Ferrocene on 3 layer thick frozen Ag(111) surface, visualisations of horizontal ferrocene (a) top down and (b) side on and vertical ferrocene (c) top down and (d) side on.
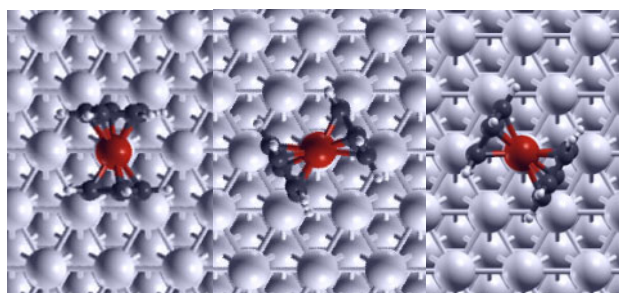
Figure 23: Geometrically symmetric horizontal adsorptions of ferrocene

rotational activation energy can also be found to see what effect surface adsorption has with respect to the gas-phase counterparts. Adsorption calculations of vertical and horizontal ferrocene on Ag(111) resulted in minimal change in geometry (Fig. 22) from the initial position. Both orientations of ferrocene are centred with a single surface layer silver atom. The energy difference between horizontal and vertical orientation is negligible at 0.1 eV with the vertical orientation being the higher energy orientation. This suggests that there is no favourability between vertical and horizontal absorption geometries from an energetics point of view. This confirms that ferrocene can remain vertically adsorbed on an Ag(111) surface at room temperature.

Consider that the 111-surface has a 3-fold high -symmetry and when rotated 60° is geometrically identical. Horizontally adsorbed ferrocene therefore forms at least 3 geometrically identical adsorption geometries (Fig. 23) based on the calculated high-symmetry adsorption geometry (Fig. 22 a).

However, insufficient results were produced to gain any further insights into other adsorption geometries or to analyse the effect of adsorption on ferrocene's rotational barrier. Therefore,

it is unknown if ferrocene has a 111 low-symmetry adsorption geometry. To determine if there are more adsorption geometries of ferrocene on Ag(111) various starting positions are needed to see which starting positions lead to the same final geometry. Multiple single point energy calculations using the geometry optimisations presented in this chapter needed to map the effect of surface adsorption on ferrocene's rotational barrier.

4.3.3 XPS of as-received DBF

Determining the stoichiometry of as-received DBF is an important baseline for the analysis of surface reacted DBF. Survey spectrum XPS of DBF powder on carbon tape shows the expected concentration ratio of Fe:Br, 1:2 and a higher than molecular concentration of carbon potentially due to the carbon tape or advantageous carbon due to sample preparation in atmosphere. single contributions to the Fe 2p and Br 3p peaks, and two expected
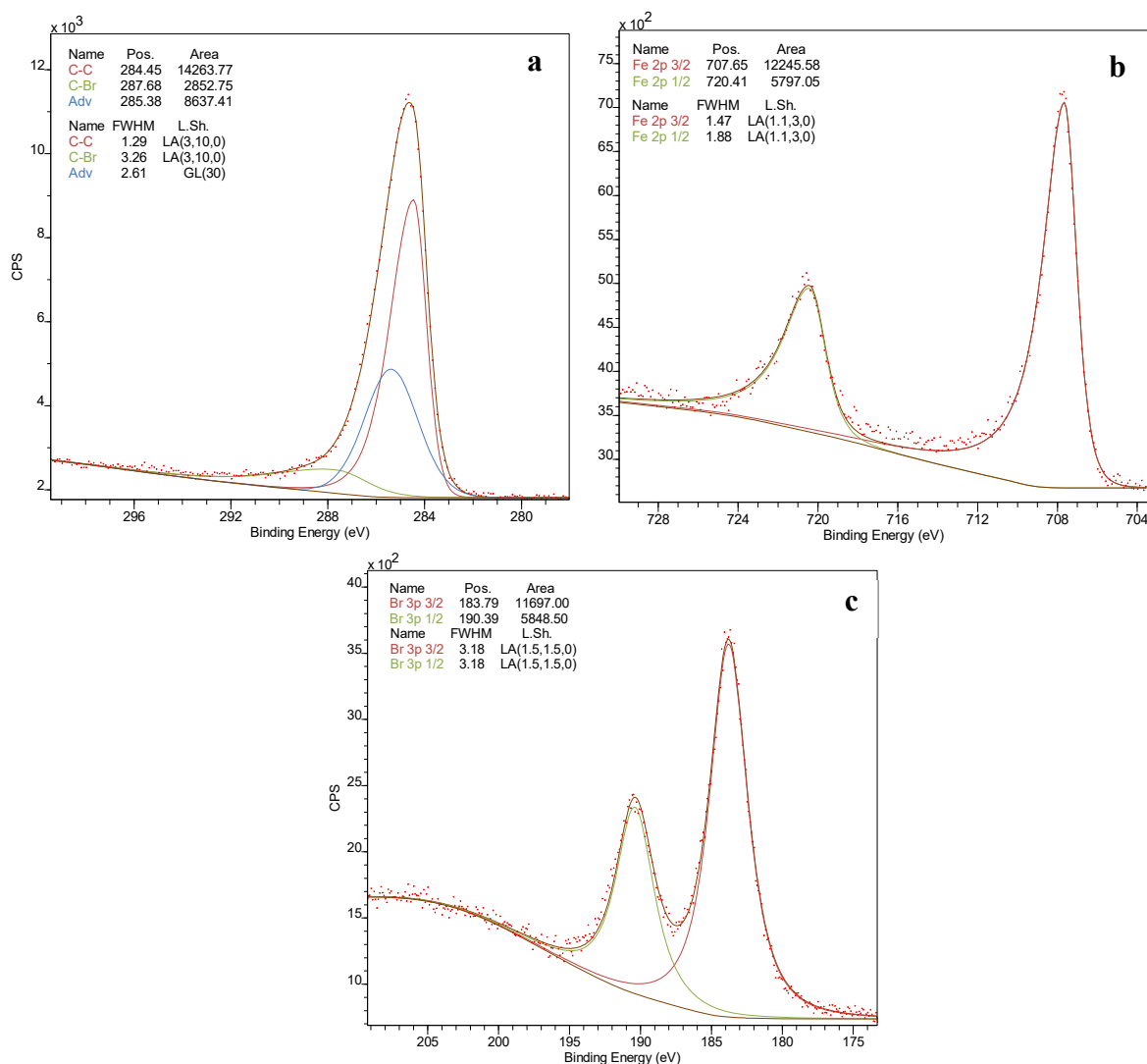
Figure 24: Powdered DBF XPS gathered with the Kratos Supra on a chilled sample bar on carbon tape surface over 18 minutes. The core levels are a) C 1s b) Fe 2p c) Br 3p.

components to the C 1s as well as a third component of advantageous carbon. The peak positions for C 1s and Fe 2p 3/2 are in good agreement with the expected position from past work for ferrocene at 284.45 eV and 707.65 eV respectively[13], with expected C-Br contribution around 287.68 eV with a ratio of 1:5, Br-C to molecular carbon. The powder DBF appears to be molecularly intact with the Br 3p 3/2 peak position at 183.79 eV which if intact is a Br-C bond component. The large FWHM in the Br 3p suggests some form of chemical change as bromine only has one potential coordination and all other peaks have a much lower FWHM, suggesting a chemical change.

4.4 Chapter Summary

The DFT-calculated rotational barrier for ferrocene was below the published values. The accuracy of the calculated barrier increased as the basis set size was reduced, and orbital polarisation was ignored. This was counter to the published literature that expects worse accuracy as the basis set decreases in size. The calculated rotational barrier for dibromoferrocene was above published values. The accuracy of the calculated barrier increased as the basis set size was increased, and orbital polarisation was included. The cause of the inaccuracy in both structures is potentially from overestimation of the $J(\rho)$ component in the energy functional used in DFT due to ferrocenes uniquely stable structure from Cp ring interactions. In hindsight, the use of a functional including dispersion corrections would have been a wise choice due to the significant improvement dispersion corrections provide[14], likely fixing the inaccuracy cause by the $J(\rho)$ component. The split-valence basis sets used in these calculations may also be a cause of error as the smallest basis set was found to be most accurate. However, with the number of functional and basis set options available, finding the right combination that produces the most accurate result is, and should be, a thesis in and of itself.

However, the potential barrier maps produced for ferrocene appear to agree with the literature for expected stable states. This gives confidence that the map of dibromoferrocene rotational potentials is also representative of the real barrier. Based on the literature ferrocene with a rotational barrier of ~0.04 eV and dibromoferrocene with a rotational barrier of ~0.035 eV, are not rotationally active at room temperature (0.02586 eV) unless also interacting with incident photons of infrared and above.

Vertically adsorbed ferrocene on Ag(111) has the potential to remain vertical as seen in Figure 22, the optimisation on Ag(111). However, due to the lack of calculations performed,

the two optimisations of surface adsorbed ferrocene presented in this chapter provide little insight into potential adsorption geometries and the effect of surface adsorption on the molecule. A detailed analysis consisting of multiple initial geometries, single point energy calculations of vertical ferrocene to determine the rotational barrier and various functionalisations, including deprotonated and dibrominated ferrocene, is desirable.

It was found that the Br-C bond in the Br 3p 3/2 peak had a BE of 183.79 eV and the Fe 2p 3/2 peak for intact DBF is consistent with other literature at 707.65 eV[13]. The fits presented are speculative with plenty of room for other potential fits. Nonetheless, the confirmed peak energies the Fe 2p peak and Br-C bonds in DBF are useful baselines for future analyses of Ag(111) and Au(111) surface deposited DBF XPS.

4.5 References

1   Frisch, M. J., Trucks, G. W., Schlegel, H. B., Scuseria, G. E., Robb, M. A., Cheeseman, J. R., Scalmani, G., Barone, V., Petersson, G. A.. Nakatsuji, H., Li, X., Caricato, M., Marenich, A. V., Bloino, J., Janesko, B. G., Gomperts, R., Mennucci, B., Hratchian, H. P., Ortiz, J. V., Izmaylov, A. F., Sonnenberg, J. L., Williams, Ding, F., Lipparini, F., Egidi, F., Goings, J., Peng, B., Petrone, A., Henderson, T., Ranasinghe, D., Zakrzewski, V. G., Gao, J., Rega, N., Zheng, G., Liang, W., Hada, M., Ehara, M., Toyota, K., Fukuda, R., Hasegawa, J., Ishida, M., Nakajima, T., Honda, Y., Kitao, O., Nakai, H., Vreven, T., Throssell, K., Montgomery Jr., J. A., Peralta, J. E., Ogliaro, F., Bearpark, M. J., Heyd, J. J., Brothers, E. N., Kudin, K. N., Staroverov, V. N., Keith, T. A., Kobayashi, R., Normand, J., Raghavachari, K., Rendell, A. P., Burant, J. C., Iyengar, S. S., Tomasi, J., Cossi, M., Millam, J. M., Klene, M., Adamo, C., Cammi, R., Ochterski, J. W., Martin, R. L., Morokuma, K., Farkas, O., Foresman, J. B., Fox, D. J. Gaussian 16 Rev. B.01. (2016).

2   Van Noorden, R., Maher, B. & Nuzzo, R. The top 100 papers. *Nature* **514**, 550-553, doi:10.1038/514550a (2014).

3   Park, C. & Almlöf, J. The electronic and molecular structure of ferrocene. *J Chem Phys* **95**, 1829-1833, doi:10.1063/1.461031 (1991).

4   Becke, A. D. A new inhomogeneity parameter in density-functional theory. *J Chem Phys* **109**, 2092-2098, doi:10.1063/1.476722 (1998).

5   Meyer, J., Bredow, T., Tegenkamp, C. & Pfnur, H. Thiol and thiolate bond formation of ferrocene-1,1-dithiol to a Ag(111) surface. *J Chem Phys* **125**, 194705, doi:10.1063/1.2387169 (2006).

6   Giannozzi, P. *et al.* QUANTUM ESPRESSO: a modular and open-source software project for quantum simulations of materials. *J Phys Condens Matter* **21**, 395502, doi:10.1088/0953-8984/21/39/395502 (2009).

7   Neal Fairley, A. C. *The Casa Cookbook: Recipes for XPS Data Processing, Pt. 1.* (2005).

8   Phillips, L. *et al.* The molecular structure, equilibrium conformation and barrier to internal rotation in decachloroferrocene, Fe(eta-C(5)Cl(5))(2), determined by gas electron diffraction. *Dalton Trans* **39**, 4631-4635, doi:10.1039/c001366h (2010).

9   Almenningen, A. *et al.* The molecular structure of decamethylferrocene studied by gas phase electron diffraction. Determination of equilibrium conformation and barrier to internal rotation of the ligand rings. *J Organomet Chem* **173**, 293-299, doi:10.1016/s0022-328x(00)84784-1 (1979).

10   Harvey, J. N. On the accuracy of density functional theory in transition metal chemistry. *Annu Rep Sect "C": Phys Chem* **102**, doi:10.1039/b419105f (2006).

11   Kepp, K. P. Trends in Strong Chemical Bonding in C2, CN, CN(-), CO, N2, NO, NO(+), and O2. *J Phys Chem A* **121**, 9092-9098, doi:10.1021/acs.jpca.7b08201 (2017).

12   Appel, M., Frick, B., Spehr, T. L. & Stuhn, B. Molecular ring rotation in solid ferrocene revisited. *J Chem Phys* **142**, 114503, doi:10.1063/1.4915067 (2015).

13   Barber, M., Connor, J. A., Derrick, L. M. R., Hall, M. B. & Hillier, I. H. High energy photoelectron spectroscopy of transition metal complexes. Part 2.—Metallocenes. *J. Chem. Soc., Faraday Trans. 2* **69**, 559-562, doi:10.1039/f29736900559 (1973).

14   Mardirossian, N. & Head-Gordon, M. Thirty years of density functional theory in computational chemistry: an overview and extensive assessment of 200 density functionals. *Mol. Phys.* 115, 2315-2372, doi:10.1080/00268976.2017.1333644 (2017).

Chapter 5: Characterisation of Ullmann dehalogenated dibromoferrocene on Ag111 and Au111

5.1 Introduction

Molecular machines are of great interest for the potential of nanoscale manipulation and charge transfer technologies. However, localizability and predictability pose problems that must be solved to enable the controllability and use of molecular machines. Ferrocene has potential as a molecular rotor due to its rotational degree of freedom, which could be used in molecular machinery. Deposition of ferrocene onto a surface is the first sage of achieving localizability. The first issue that arises is maintaining ferrocene's mechanical degree of freedom while forming strong bonds with the surface.

The aim of this work is to produce ferrocene-adatom oligomers to stabilise vertically adsorbed ferrocene by increasing the total number of surface interactions. Ullmann dehalogenation could achieve ferrocene coordination around a metallic adatom coordination centre. A halogenated ferrocene molecule is necessary to take advantage of Ullmann dehalogenation, therefore dibromoferrocene was chosen as the molecular precursor. The metallic surfaces most frequently used in Ullmann reactions are noble metals such as gold, silver, and copper.[1] These surfaces are catalytic and can drive the Ullmann reaction. This work used dosing line sublimation deposition at room temperature.

This work's aim was to produce coordination organometallic bonded ferrocene-adatom oligomers to achieve localisable controllable ferrocene. This will expand the number of viable parts available for use in molecular machines. This work also aims to probe the properties of deposited DBF structures.

5.2 Methods

Experiments were carried out in an Omicron UHV system with a base pressure of $\sim 10^{-8}$ mbar. Surfaces were cleaned by Ar^+ sputtering (1 keV) for 5 minutes and e-beam annealing at 700 K for 5 minutes. XPS and STM were performed on the clean surface to verify cleanliness and order. Once the surface had cooled to approximately room temperature (~300 K) deposition of dibromoferrocene was performed via dosing line sublimation at room temperature.

Non-monochromated magnesium source XPS was used to produce a survey spectrum, C1s, Fe2p and Br3p high resolution peaks for analysis of stoichiometric trends but was not relied

on for absolute concentrations. This work looks at only the 3/2 Fe 2p peaks because the Ag 3s peak is contained within the 1/2 Fe 2p. Various deposition times and systems were tested to determine at what point the surface became saturated and understand the surface chemistry. These included depositions for 60 and 30 minutes on clean surfaces; consecutive 10, 20, 30 and 60 minute depositions without cleaning and XPS done in between each deposition; 60 minute deposition onto preheated (375 K) Ag(111). Ullmann reaction speed and the number of reactions was tested for by performing XPS after leaving the surface overnight. Annealing of the surface after deposition was also performed up to 675 K. Deposition onto Au(111) was performed and XPS spectra taken using an Al source. This was followed by Ar^+ sputtering and annealing, a fresh deposition of DBF, and followed immediately after by STM imaging.

STM imaging was performed overnight on surfaces with different deposition times and previous treatments. Surfaces that were imaged include; Clean Ag(111) and Au(111); 60 minutes deposition on Au(111), then immediate STM; 60 minutes deposition and 20 minutes of X-ray incidence on Ag(111) and Au(111); finally, 60 minutes deposition, 20 minutes of X-ray incidence and annealing on Ag(111). The clean Ag(111) was used for STM calibration by comparing the expected nearest neighbour distance of silver (0.288 nm). Distance and size measurements were performed using the profile and FFT tools provided by the WSxM package[2]. Angular measurements were performed using ImageJ software package[3].

NEXAFS was also performed at the Australian Synchrotron facility on DFB deposited Ag(111) and Au(111) surfaces. DBF was deposited onto clean Au(111) and Ag(111) in QUT's Omicon UHV system and air transferred to the Australian Synchrotron. Upon deposition NEXAFS was then performed with polarised X-rays at varying incidence angles of 20, 40, 55, 70 and 90°. The spectra were analysed using the QANT software package[4], and double normalised against incoming photon flux collected from a gold mesh in the path of the beam with a photodiode signal to account for spurious I0 signals from carbon contamination on the mesh.

5.3 Results and Discussion

5.3.1 Deposition onto Ag(111)

5.3.1.1 XPS of room temperature deposition

 Three consecutive depositions of DBF were performed (30, 60 and 120 minutes) via dosing line, with XPS performed between cycles, were performed with a one-hour gap left between

each deposition. The area of the Fe 2p spectra increased with each deposition describing the continued adsorption of DBF. As deposition time increased the uptake of DBF slowed shown by the change in Fe 2p/Ag 3d peak area (Fig. 21). This suggests that the surface was potentially nearing a monolayer thickness of

Figure 26: Fe 2p/Ag 3d XPS peak area for consecutive depositions

DBF as the uptake rate of molecule is proportional to the available surface area.

The area of the Br 3p/Ag 3d contributions followed a more asymptotic trend than the Fe 2p/Ag 3d area (Fig. 22). The ratio of Br-C bond stoichiometry relative to Br-Ag also increased (Table 2). The uptake of iron, indicative of individual ferrocene molecules, was significantly higher than apparent bromine uptake over the 60-minute deposition. It has also been found previously that bromine readily desorbs from noble metal surfaces[5]. These observations suggest that the surface was still adsorbing DBF and the rate of up take was slightly less than the debromination rate over the 60-minute deposition.
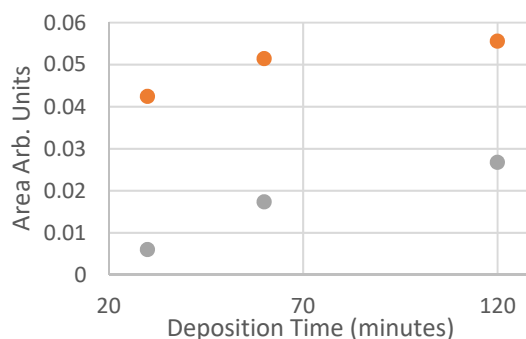
Figure 27: Br 3p/Ag 3d XPS peak area for consecutive depositions, (orange) Br-Ag and (silver) Br-C

Table 2: Ratio of bromine terminated carbon to bromine terminated silver

Deposition time (minutes)	30	60	120
Br-C : Br-Ag	0.14	0.34	0.48

Deposition of DBF was also attempted *via* crucible at around 473 K and the molecule failed to adsorb onto the Ag(111). A similar effect was seen with deposition onto a Ag(111) surface, preheated to 375 K where very little DBF precursor was adsorbed. This suggests that for Ullmann dehalogenation to occur the incident molecule must first be weakly adsorbed for the Br-C bond to be cleaved catalytically. The small amount of ferrocene that is observed on the surface may be the statistically unlikely group that approached the surface in a favourable orientation.

XPS collected over 18 minutes following a 60 minute DBF deposition onto room temperature Ag(111) (Fig. 27) shows two chemical states of Br on the surface. The higher BE

contribution arising from Br-C bonding at 183.77 eV[6,7] is close to the 184 eV peak position found in chapter 4.3.3 (Fig. 24b), however the line shapes are different. The lower BE contribution expected to be arising from dehalogenation and chemisorption of bromine leading to Br-Ag at 181.8 eV[6-8]. The lower BE is because Ag is less electronegative than Br where differences in electronegativity have been shown to affect the relative binding energies significantly[9]. It is also confirmed with observed dehalogenation that the surface-assisted Ullmann reaction is driving chemical change. Three contributions to the C 1s peak are expected if the DBF has undergone dehalogenation: C-C for intact ferrocene Cp rings at 284.5 eV, C-Br for halogenated moiety at 286.1 eV and a C-Ag peak for dehalogenated moiety that appears at 283 eV. Speculatively, the single 3/2 Fe 2p peak suggests that the ferrocene moiety is intact, despite being higher energy than in the chapter 4.3.3 baseline fit, and the Br 3p peak suggests that two-thirds of DBF have been dehalogenated.
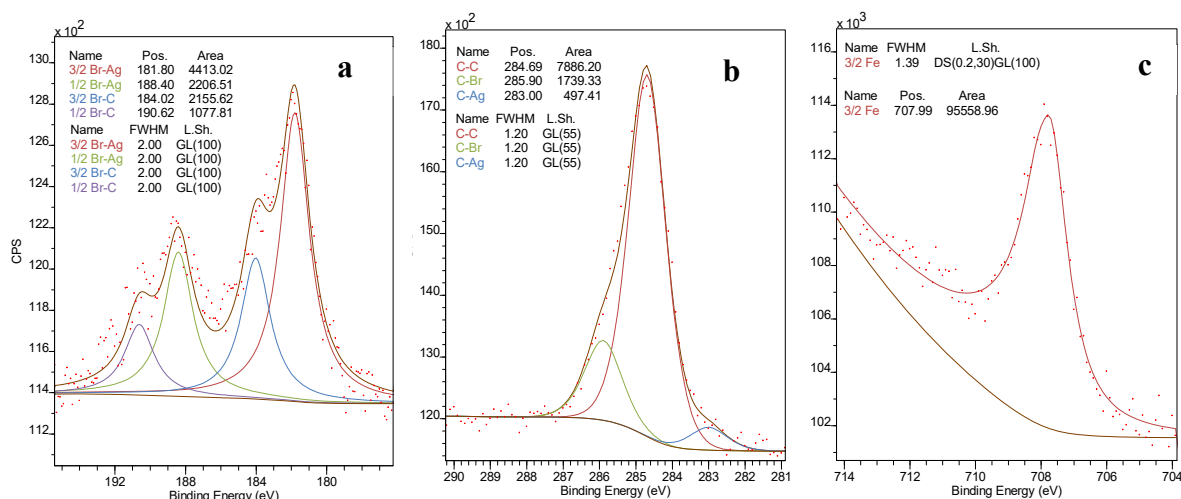
Figure 28: a) Br 3p, b) C 1s and c) Fe 2p XPS of vapor deposited DBF at room temperature over 60 minutes onto clean Ag(111). Beam energy 1253.6 eV pass energy 20 eV, step size -0.1 eV, red squares represent acquired data

The C 1s peak fits the three expected contributions well and suggests that there is only a small amount of surface bonds formed. This is surprising because if two-thirds of the bromines have dehalogenated then the C-Ag contribution would be expected to be two-thirds that of the C-Br contribution but instead the opposite is observed. This suggests that after Ullmann dehalogenation the next step of the Ullman reaction may be occurring, forming C-C bonds releasing the C-Ag atoms. Although the dissociation of C-Ag bonds at room temperature is unlikely and therefore a more likely explanation is the formation of Ag coordination centres from adatoms.
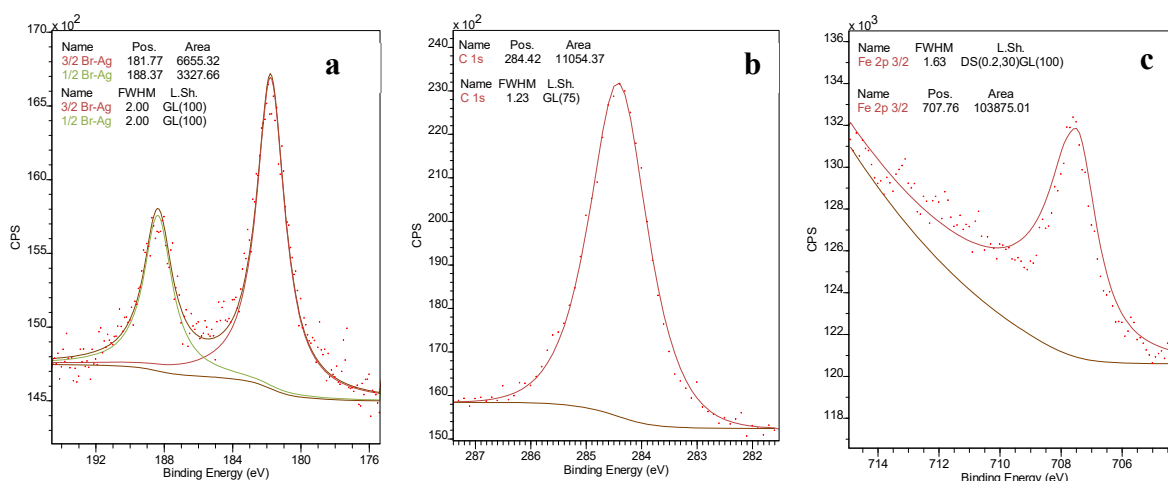
Figure 29: a) Br 3p, b) C 1s and c) Fe 2p XPS of vapor deposited DBF at room temperature over 60 minutes onto clean Ag(111), annealed up to 673 K for 5 minutes. Beam energy 1253.6 eV pass energy 20 eV, step size - 0.1 eV, red squares represent acquired data.

After annealing the sample at 673 K over 5 minutes, the ferrocene moiety appears to have fully dehalogenated, indicated by the singular Br-Ag component (Fig. 28a). The C 1s peak fits only one contributions of C-C suggesting that the molecule has undergone the full Ullmann reaction. Potentially ferrocene dimers or some form of ferrocene polymer has been formed.

On a clean surface a 30-minute deposition was performed with XPS performed as soon as possible following deposition, shows two almost-equal sized contributions to the Br 3p peak (Fig. 29a). This suggests that ~50% of the DBF bromines are debrominated on initial contact with the surface. This sample was the left overnight (>8 hrs) and XPS was performed again. The Br 3p peak (Fig. 29b) showed a shift in contribution from 1:1 Br-C:Br-Ag for the as-deposited surface, to a larger Br-Ag and reduced Br-C contribution in a 1:0.27 ratio. This is like the Br 3p spectrum of longer 60+ minute deposition (Fig. 27a) in which a larger amount of chemisorbed bromine is observed. These observations suggest that the second debromination reaction occurs relatively slowly. Taking ~30 minutes for a majority of the adsorbed and singularly debrominated DBF to debrominate a second time. The resulting ferrocene molecules could be horizontally oriented for the active sites on the aromatic rings where the original Br molecules were to directly interact with the Ag(111) surface. However,

54

dehalogenation via adatoms is also a possibility and could result in (mostly) vertical ferrocene.
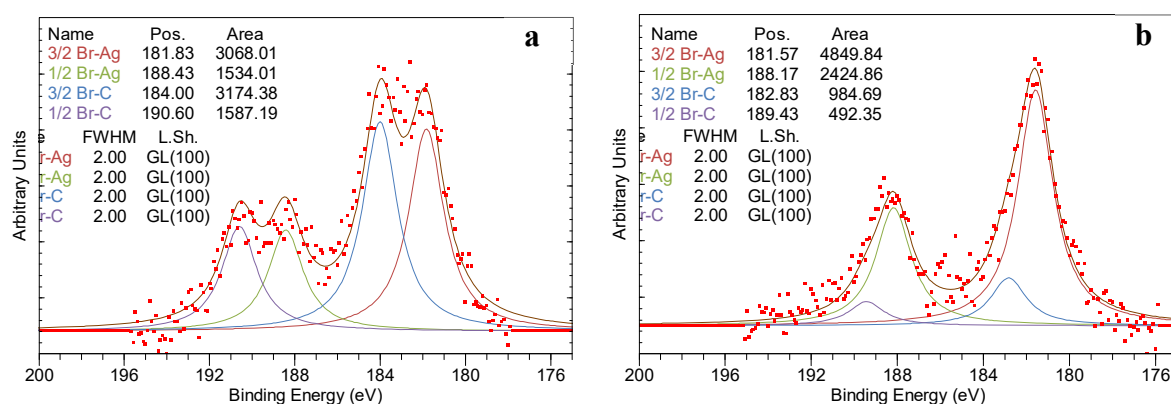
Figure 30: Br 3p XPS; a) immediately after vapor deposition of DBF at room temperature over 30 minutes onto clean Ag(111), b) after being left for 30 minutes without incident x-rays. Beam energy 1253.6 eV, pass energy 20 eV, step size -0.1 eV, red squares represent acquired data.

The cause of hindrance between the first and second debromination could be due to a combination of various barriers. Vertical orientation of the ferrocene moiety, alignment of the bromines hindered by the rotational barrier and interactions such as steric hinderance[1] and π-π stacking from other adsorbed DBF could all be barriers hindering secondary dehalogenation.

5.3.1.2 STM of room temperature deposition

STM images of as-deposited DBF on Ag(111) show large domains (>40 nm) of well-ordered, linear structures (corn-rows) (Fig. 27 b,c). The STM allowed for atomic scale resolution of clean silver and molecular scale resolution of as-deposited ferrocene. A STM image of the annealed sample was produced showing signs of molecular decomposition due to messy carbon amalgamations (Fig. 30).
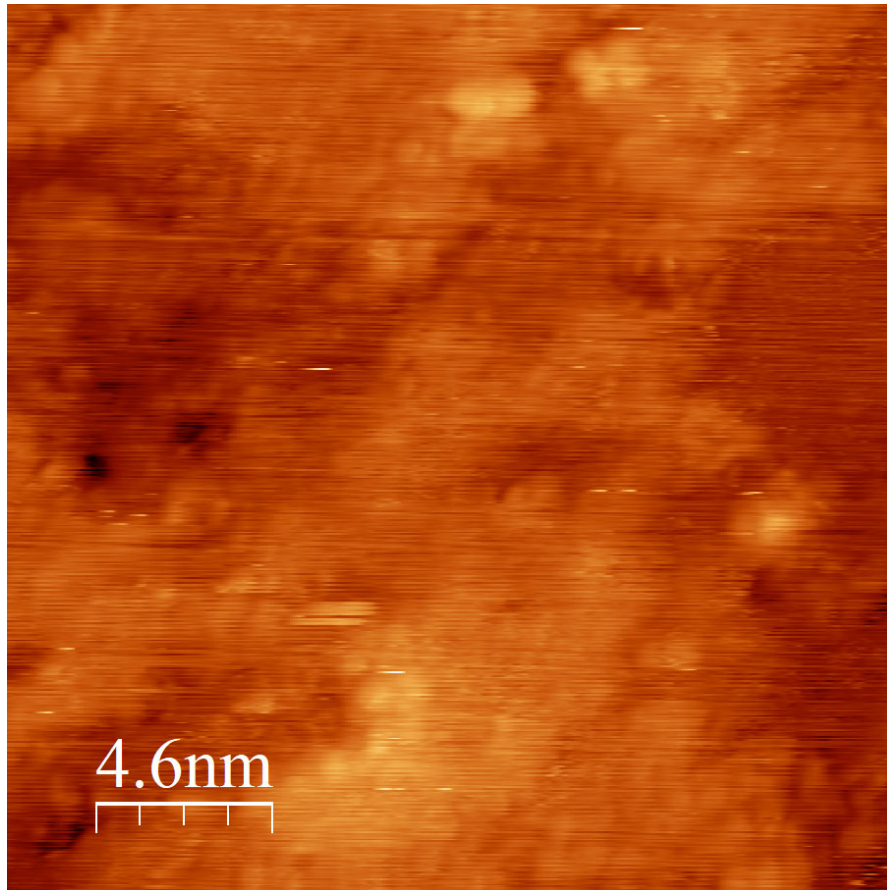
Figure 31: Room temperature STM of DBF on Ag(111) annealed up to 673 K
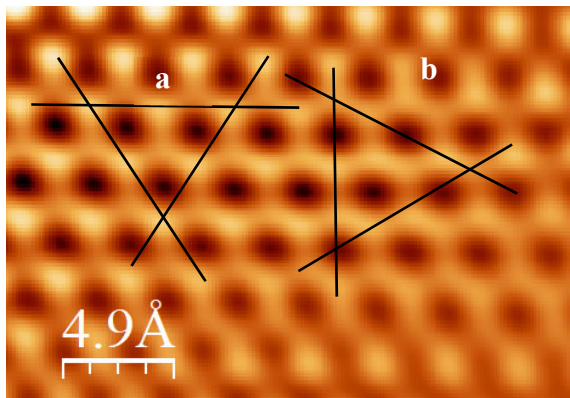
Figure 32: Clean Ag(111) single crystal, lines indicate a) low-symmetry directions, b) high-symmetry directions. Bias voltage -0.01 V, tunnelling current 12.31 nA

STM calibration was performed on an atomic resolution Ag(111) image (Fig. 26). In this image it is possible to see the high contrast first layer atoms and the lower contrast second layer atoms. The uncertainty in the STM measurements was determined by measuring the nearest neighbour distances. This was done by measuring the peak to peak distance of the image profile across the high contrast first layer atoms. The uncertainty in the measurements was determined to be the increment distance between data points/pixels, ±0.02 nm.
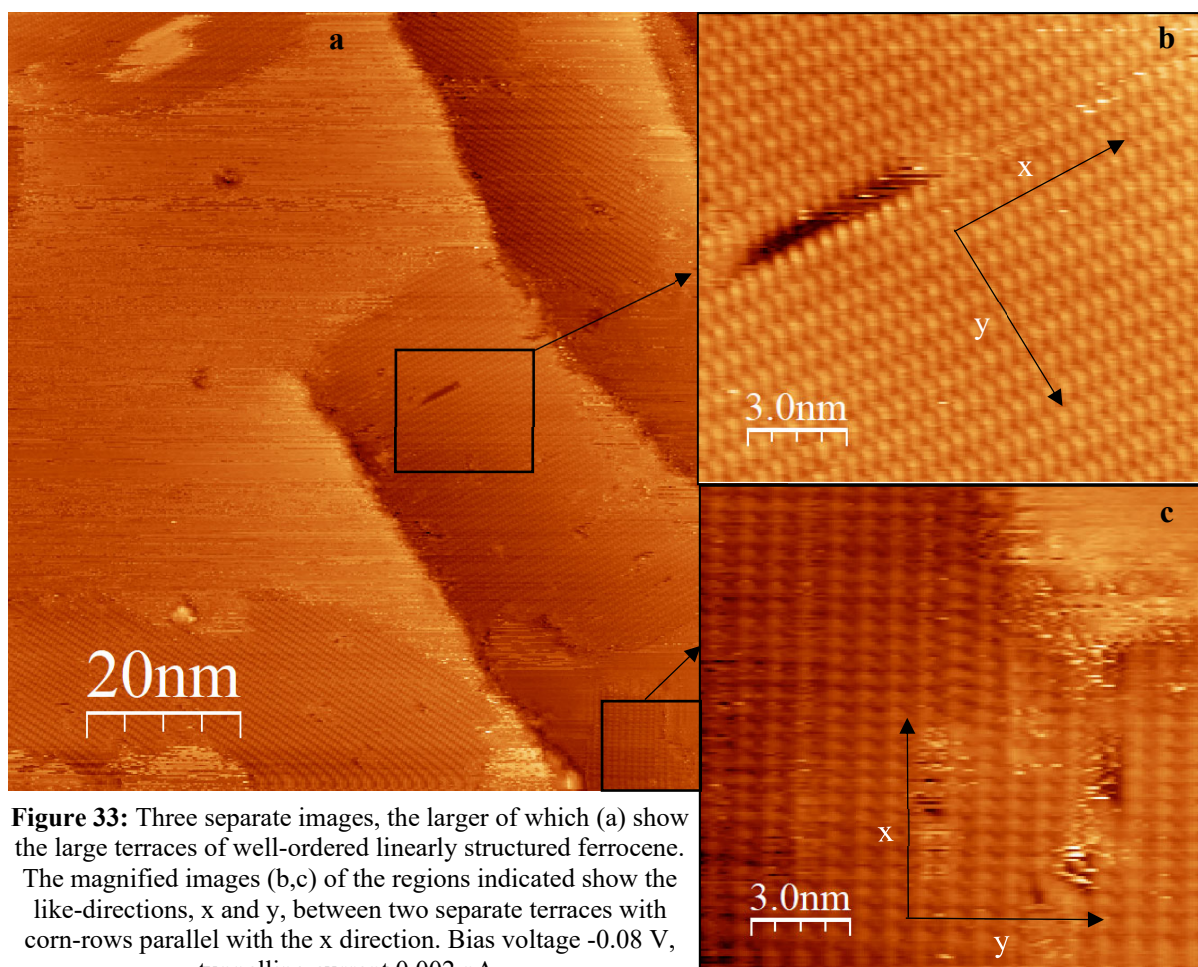
Figure 33: Three separate images, the larger of which (a) show the large terraces of well-ordered linearly structured ferrocene. The magnified images (b,c) of the regions indicated show the like-directions, x and y, between two separate terraces with corn-rows parallel with the x direction. Bias voltage -0.08 V, tunnelling current 0.002 nA.

The well-ordered, linear structures of ferrocene that debromination of DBF produces extend up to and potentially beyond 40 nm (Fig. 27). The linear structures appear to align along the three (111) high-symmetry directions (Fig. 26 b). When measuring the angle between structures' equivalent directions, the angles are 60 and 120° (Fig. 28). If there were 30° between equivalent directions, these would fall outside of the three (111) high-symmetry directions and there would be six lower-symmetry degenerate directions. No images where found where 30-degree angles were measured between equivalent directionalities.

To determine if each individual protrusion is a single molecule, individual protrusions were measured as well as various structural defects (Fig. 29). Features in the x direction were found to be on average 0.33±0.02 nm in size with a 0.25±0.02 nm gap between each feature. Features in the y direction were found to be on average 0.45±0.02 nm in size with a 0.43±0.02 nm gap between each feature. The periodicities for the structures are on average 1.2 nm^{-1} in the x direction and 2 nm^{-1} in the y direction. The smallest defects observed are
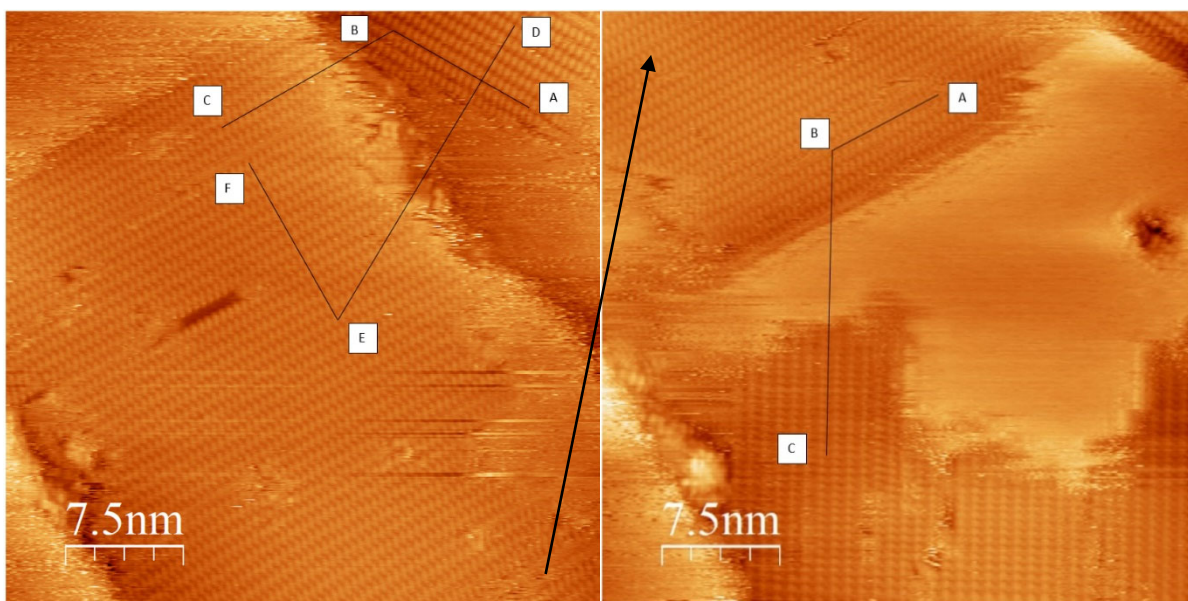
Figure 34: Two joining images of molecular resolution ferrocene with 3 structures in 3 orientations on Ag(111). Angles ABC aligning the like directions between the three separate orientations in both images was measured as 120° and DEF as 60°. Bias voltage -0.08 V, tunnelling current 0.002 nA.

assumed to be individual molecules as there was no indication of molecular breakage in the XPS analysis. The smallest defects identifiable in the STM images appear to be individual protrusions. A single protrusion defect measure to be 0.35±0.02 nm in the x direction and 0.47±0.02 nm in the y direction. With XPS analysis suggesting horizontally oriented ferrocene moieties and DFT measurements of ferrocene in chapter 4, an individual protrusion or defect can fit a single horizontal ferrocene molecule.
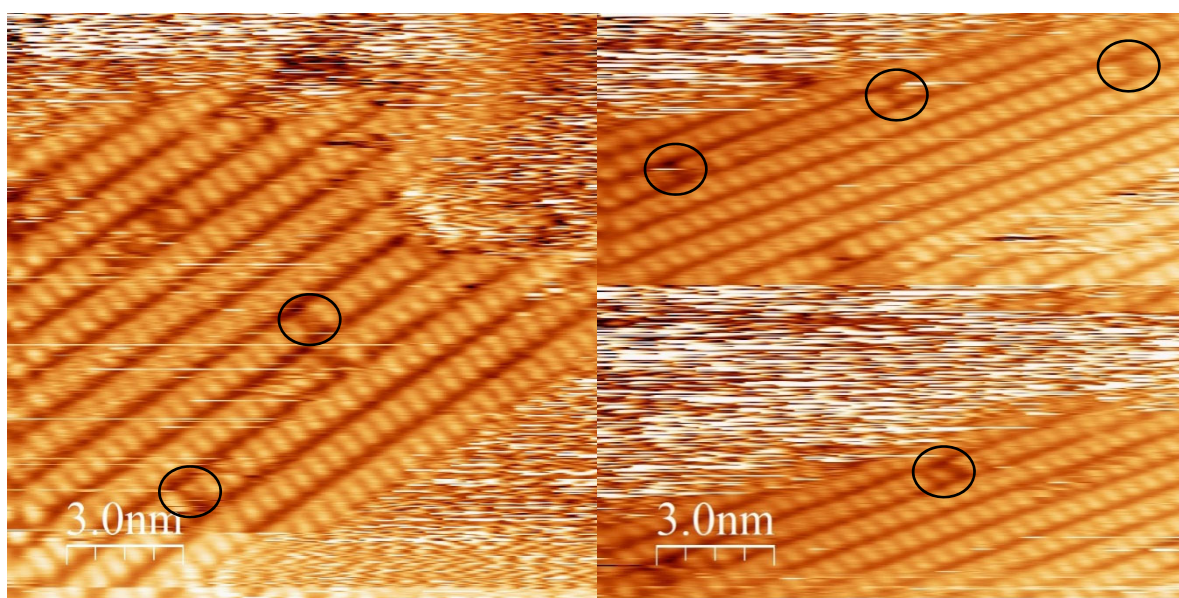
Figure 35 Structural defects in the ferrocene structure indicated by the black circles. Bias voltage -1 V, tunnelling current 0.01 nA

Previous work has shown that horizontal undistorted eclipsed ferrocene forms a line in STM images parallel with the ferrocene orientation[10]. The STM images of horizontal ferrocene gathered in this work appear to from similar lines. As STM images show the LDOS of the imaged molecule the lines produced can be determined to be the hydrogen atoms protruding from the Cp rings. The uniformity of feature and gap size in each axis suggests that the ferrocene moieties are all oriented in the same direction. This would lead to the expectation that π-π stacking is a driving force in the ordering. Bromine from Ullmann dehalogenated molecules have been shown in the past to significantly affect the structure formed by the original moiety[13]. Steric effects are also expected to be a contributor to the ordering of surface structures as has been studied in detail in previous works[1,7,14,15]. The larger gaps between each line could therefore be attributed to steric hindrance from the hydrogen atoms and/or affected by bromine-hydrogen bonding. However, there are several potential orientations the ferrocene could take, with the forces and protrusion measurements in mind. Discerning the orientation of the individual ferrocene molecules is a non-trivial issue because there are no characteristic circle or parallel line shapes as seen in other works[10-12].

There is a large variation in the protrusion shape and contrast from image to image. Some images show lines with a bright spot in the centre, others show a zig-zag pattern with asymmetric contrast. Previous work has shown that asymmetric contrast does not necessarily mean a difference in geometry between the high and low contrast points[16]. This is a complex system explainable only by considering tip condition, surface interactions and bias voltage. This is beyond the scope of this work and should be investigated in future projects.

STM images can indirectly indicate to adatoms as part of the structures. In adatom dehalogenated molecules and adatom-linked organometallic structures a bright spot between dehalogenated moieties, designated as a surface adatom, is often observed[13,14,17]. However, assuming that there are adatom-ferrocene organometallic bonds due to Ullmann dehalogenation these adatoms would be found beneath the ferrocene structures not directly detectable by the STM tip. However, adatom-linked structures often form well-ordered structured from the dehalogenated moieties[13,14] like what is observed in the ferrocene structures.

5.3.1.3 Crystallographic analysis

Because the FT of a lattice is the reciprocal lattice, using an FFT on the STM images produces a reciprocal lattice of the molecular structure (Fig. 30). The vectors of the FFT

reciprocal can then be turned into a matrix. Inverting this matrix produces the lattice constants of the molecular structure, given by

$$\begin{bmatrix} a_i & a_j \\ b_i & b_j \end{bmatrix} = \frac{1}{a_i^* b_j^* - a_j^* b_i^*} \begin{bmatrix} b_j^* & -a_j^* \\ -b_i^* & a_i^* \end{bmatrix}, \tag{7}$$

where a_i^* is the reciprocal lattice constant a^*, in the ith direction (2.003 nm^{-1}) and b_j^* is the reciprocal lattice constant b^* in the jth direction (1.134 nm^{-1}). Constant a^* in the jth direction and b^* in the ith direction are 0 as they are at right angles to a_i^* and b_j^*. This matrix inversion equates the real-space lattice constants a_i, a_j, b_i and b_j of the ferrocene Ag(111) structure. These were found to be $a_i = 0.881$ nm, $a_j = 0$ nm, $b_i = 0$ nm, and $b_j = 0.499$ nm describing an orthorhombic Bravais lattice. From multiple FFTs the same reciprocal lattice constants were observed.
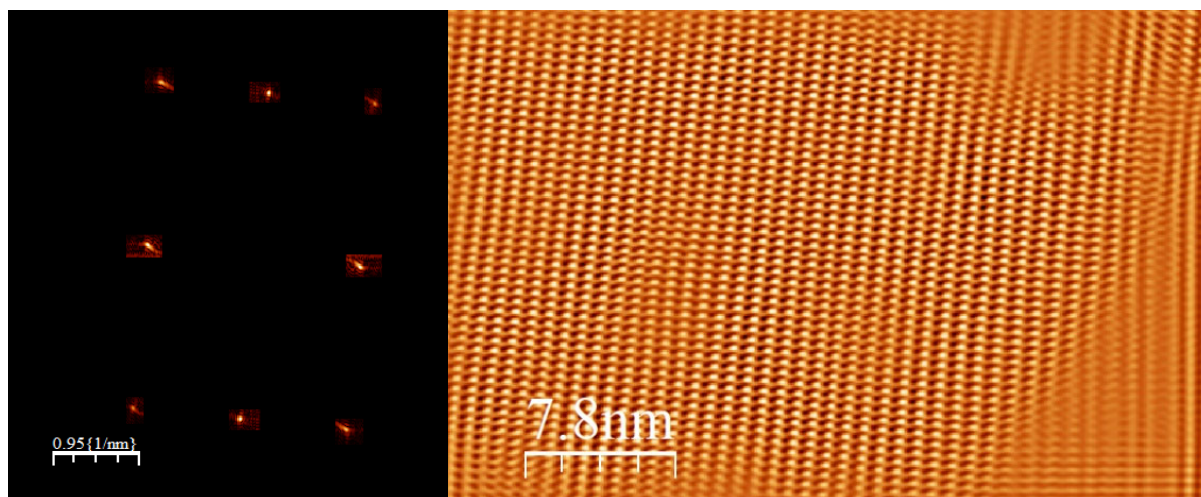
Figure 36 2D-FFT filter of the ferrocene structure.

Directly measuring the real space structures from protrusion to protrusion produced lattice constants of $a \cong 0.9 +- 0.02$ nm and $b \cong 0.5 +- 0.02$ nm, agreeing with the FFT unit cell calculation well. As all structures observed in this work fit this same well-ordered crystal structure with identical lattice constants there is no reason to assume there would be other stationary ferrocene structures on the surface. However, there may be some mobile ferrocene molecules that the STM struggles to image.

5.3.1.4 NEXAFS

NEXAFS results for Ag(111) deposition describe the on surface molecular orientation of ferrocene to be more horizontal than vertical. This is because when looking at the C 1s K-edge adsorption (270- 320 eV)[4] (Fig. 31), stronger photon-orbital coupling with Cp σ*orbitals

($\sim$290+ eV)[18] occurred when the x-ray beam was at 20° to the surface. There was also a decrease in the intensity of photon-orbital coupling in transition peak B, Fig. 31 ($\sim$287-290 eV)[20], from 90 to 20-degree incidence. This suggests that there are more x-ray interactions when perpendicular to the surface.[21] Interestingly, there appeared to be no change in photon-orbital coupling with the 285 eV peak attributed to the C 1s$\rightarrow$ Fe $3d_{(xz,yz)}$/Cp π^* orbital transition[20,22], but this could be due to atmospheric carbon from the air transportation. Angle appears to only effect peak intensity when above 287 eV which may suggest π^* orbital/Rydberg state mixing[19,23] or dichroism. If neither Rydberg state mixing nor dichroism is the cause, then suggest that there is a constant number of Cp π^* orbitals perpendicular to the x-rays at all incidence angles, which would be the expected outcome when ferrocene is neither horizontally nor vertically adsorbed but a mix of both or tilted with respect to the surface normal. This agrees with equation 5 where $I_\nu^{||}$ is the spectra intensity, θ is the x-ray incidence angle and α represents a polar angle with respect to the surface normal[24],

$$I_\nu^{||} = \frac{1}{3}\left[1 + \frac{1}{2}(3\cos^2\theta - 1)(3\cos^2\alpha - 1)\right]. \qquad (8)$$

The above equation gives an angle α of 57.4±0.4° using the spectral features from 287-290 eV (Fig. 31 B). This suggests the resonance intensities are independent of the x-ray incidence θ and therefore there may be a mix of horizontally and vertically adsorbed or semi-vertical ferrocene and potential adventitious carbon contamination.
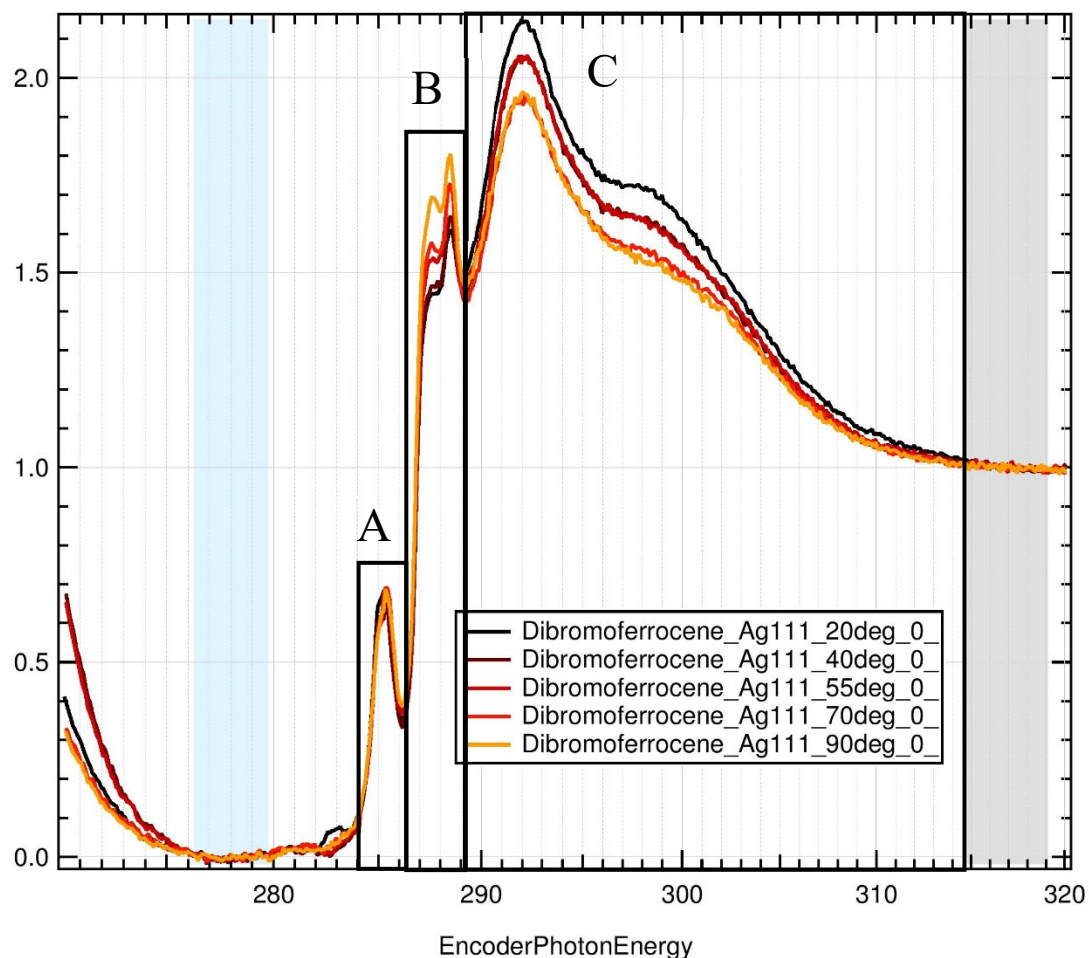
Figure 37 NEXAFS spectra of the carbon K-edge gathered at varying beam incidence from 20-90°. Orbital transitions are labled (Table 3) and the resonance intensity dependence on incidence angle is observed.

Table 3: NEXAFS Carbon K-edge spectra (Fig. 34) peak assignment[20]

Label	Carbon K-edge
A	C 1s→ Fe $3d_{(xz,yz)}$ /Cp π*
B	C 1s→ Fe 3d /Cp π*
C	C 1s→ Fe 3d /Cp σ*

Peak B in the carbon K-edge has only previously been attributed to a C 1s→ Fe 3d /Cp π* transition however there is clearly multiple contributions to the peak. This may be due to the air transfer, leading to the expectation of contamination from oxygen as the cause of the extra contributions.

Interestingly there is a resonance intensity reduction and then increase in the Fe L-edge adsorption spectrum in an unidentified transition peak between 711-713 eV (Fig. 32 C). The intensity change occurs at grazing incidences from 20° to the magic angle ~55-degrees decreasing in intensity before increasing again between 55 and 90°. This appears to occur throughout the spectra suggesting that this may be due to poor normalisation. The two
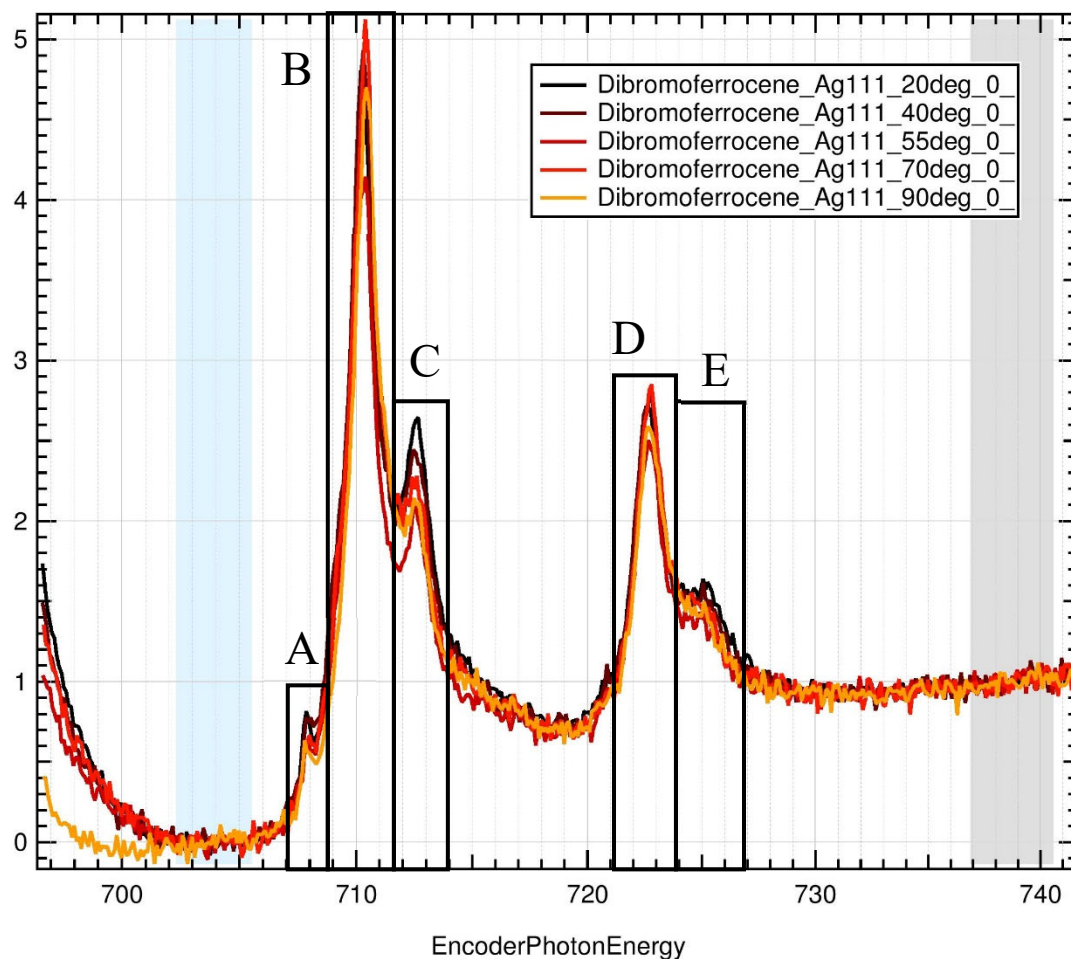

Figure 38 NEXAFS spectra of the iron L-edge gathered at varying beam incidence from 20-90°. Orbital transitions are labelled (Table 4).

unidentified peaks do not fit the expected dual peaks from pervious work[20] as the peak separation is far too large.

Table 4: NEXAFS Iron L-edge spectra (Fig. 32) peak assignment[20]

Label	Iron L-edge
A	Fe $2p_{3/2} \rightarrow$ Fe $3d_{(xz,yz)}$ /Cp π^*
B	Fe $2p_{3/2} \rightarrow$ Fe $3d$ /Cp π^*
C	Unidentified
D	Fe $2p_{1/2} \rightarrow$ Fe $3d$ /Cp π^*
E	Unidentified

5.3.2 Deposition onto Au(111)

5.3.2.1 XPS

XPS shows that DBF deposition onto Au(111) was successful and Ullmann dehalogenation occurred upon deposition (Fig. 33). Either 26.7% of adsorbed DBF doubly dehalogenated or 53.4% of adsorbed DBF singularly dehalogenated with the remaining 73.2 - 46.6% of DBF physisorbed on the surface. Based on the reduction in total Br 3p-C and Fe 2p-C peak area, after leaving the sample for 30 minutes, it appears that a significant amount of the physisorbed DBF desorbed from the surface. Approximately 54.5% of the ferrocene moiety were doubly dehalogenated and the remaining ~45.5% were singularly dehalogenated, assuming very little bromine desorption.
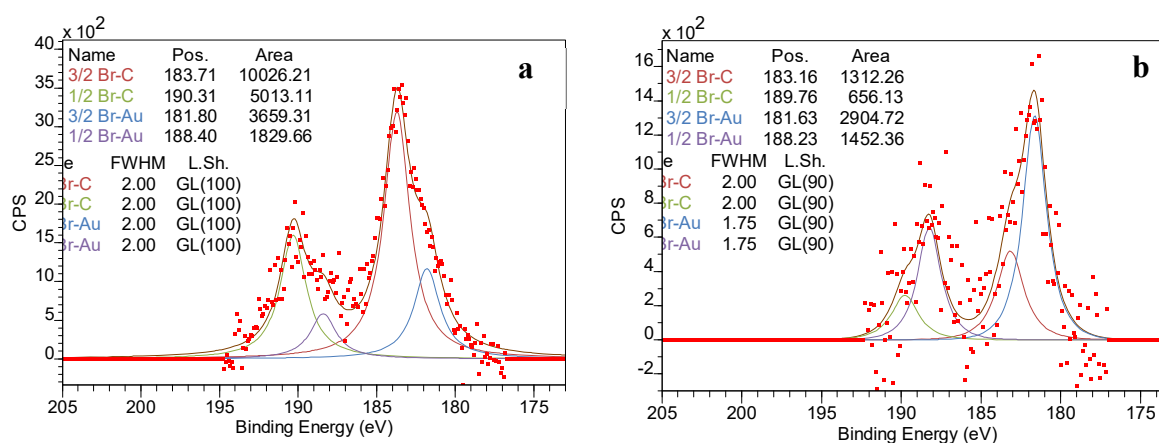
Figure 39 XPS of DBF a) Immediately after 60minutes of deposition, b) 30 minutes later. Beam energy 1253.6 eV, pass energy 20 eV, step size -0.1 eV, red squares represent acquired data.

Figure 33b has a significant amount of noise in the data due to the low number of counts, however the selected speculative peak fits make theoretical sense following the expectation of Ullmann dehalogenation of the bromine from DBF, followed by desorption of surface

64

adsorbed bromine at room temperature. Spectrum of initial dehalogenation should show a lower energy Br-Au contribution, as Br-C bonds are cleaved from the ferrocene moiety. As more Br-C bonds are cleaved a larger Br-Au peak should form, with a peak area reaching that of the original Br-C peak. However, desorption would lead to lower than expected peak areas as Br leaves the surface, which is observed in Figure 33b

5.3.2.2 STM

DBF on Au(111) produces triangular structures of varying type and size. One structure was triangular lines with single depressed vertices (Fig. 34 a) and may have been influenced by the herring bone structure of Au(111) or perhaps are found along the step edges of the substrate. These structures were always found to be long chains and no single alone triangles were observed. The other observed structures appeared to come in various shapes and sizes with dark edges and bright centres (Fig. 34 b,c). Although image quality around these triangles varied greatly, some of vertices of the larger structures were clearly imaged (Fig. 34 c) and appeared to contain a triangular group of 6-7 features. These more varied structures could be found alone or connected to others by brighter vertices creating larger fractal-like structures. The groups of 6-7 features have been observed outside of vertices (Fig. 34 d), they are ~2 nm in size and appear very similar in structure to triangulenes on Au(111)[25].

All attempts to capture STM images of the darker sections of the triangular structures were unsuccessful. STM imagery of this surface was in general found to be quite a challenge. The images in Fig. 34 were produced immediately after deposition without any X-ray incidence as to maximise surface coverage. This is because as mentioned previously X-rays and extended periods after deposition were found to reduce the amount of surface coverage, making the triangular structures much harder to find. Molecular resolution images of ferrocene moieties on Au(111) were unable to be produced in this work, as such the cause and makeup of the triangular structures is still unknown. Ferrocenes on this surface may also be mobile and not ordered which would explain the difficulty in imaging the molecules.
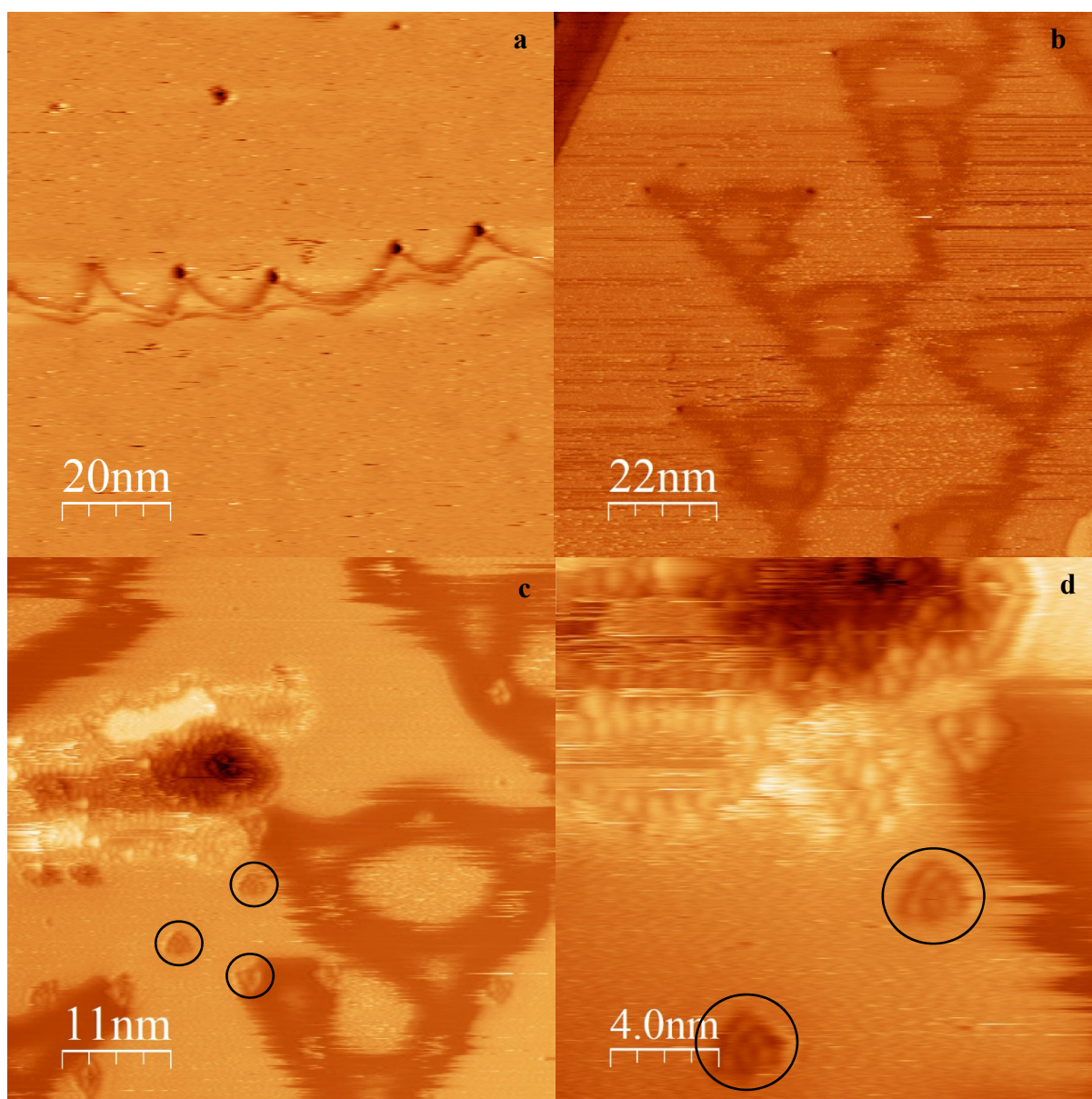
Figure 40 STM of DBF immediately after 30 minute deposition onto Au(111), no XPS was performed before the microscopy was performed. a) triangular lines with single depressed vertices, b,c) unknown fractal like structures, d) groups of 6-7 features (circled) that appear to be found in vertices of the larger structures seen in 'c'. Bias voltages and tunnelling currents a) -0.7 V, 0.005 nA. b) -1.5 V, 0.01 nA, c) -1 V, 0.002 nA, d) -0.35 V, 0.002 nA.

5.3.2.3 NEXAFS
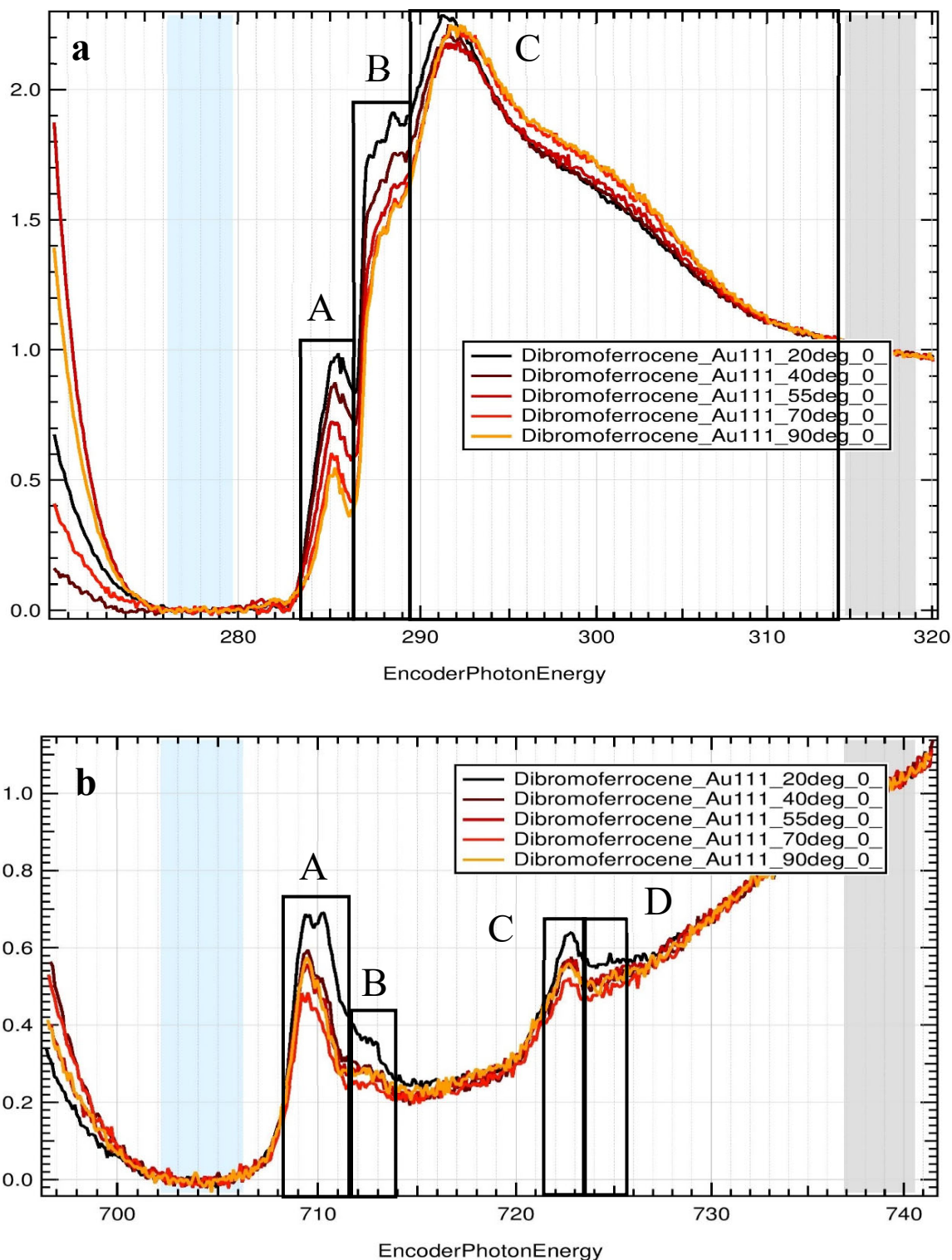
Figure 41 NEXAFS spectra of the carbon K-edge (**a**) and iron L-edge (**b**) gathered at varying beam incidence from 20-90°. Orbital transitions are shown and the resonance intensity dependence on incidence angle is observed. Peaks are labelled and assigned transitions (Table 5,6)

Table 5: NEXAFS Carbon K-edge spectra (Fig. 35 a) peak assignment[20]

Label	Carbon K-edge
A	C 1s→ Fe $3d_{(xz,yz)}$ /Cp π*
B	C 1s→ Fe 3d /Cp π*
C	C 1s→ Fe 3d /Cp σ*

Table 6: NEXAFS Iron L-edge spectra (Fig. 35 b) peak assignment[20]

Label	Iron L-edge
A	Fe $2p_{3/2}$→ Fe 3d /Cp π*
B	Unidentified
C	Fe $2p_{3/2}$→ Fe 3d /Cp π*
D	Unidentified

NEXAFS Carbon K-edge results show the highest resonance peak intensities when the x-rays were incident at 20° to the surface. The peak intensities then dropped sharply to 40 with the lowest intensities at 70 and 90° (Fig. 35 a). This indicates that the adsorbed ferrocene moieties are almost vertical, because the transitions to the Cp π*'s are more numerous, and remain in this orientation on the Au(111) surface. In the iron L-edge there is an intensity change between each spectrum where from grazing incidences at 20° up to the magic angle ~55-degrees the intensity decreases before increasing again between 55 and 90° and appears to occur throughout the spectra suggesting that this may be due to poor normalisation. The same two unidentified peaks that appeared on the silver sample also appear on this gold sample; this supports that there may be oxygen contamination as both samples had been air transferred.

Using equation 6, the angle α was found to be 46.4±0.6° using the spectral feature at 288 eV (Fig. 35 a,B). While this is indicative of more upright molecule than that of the Ag(111) surface, it's suggestive of a mix of horizontally and vertically adsorbed or semi-vertical ferrocene and also perhaps adventitious carbon contamination.

5.4 Conclusion

It was found that DBF was highly volatile under UHV conditions leading to the use of room temperature dosing line sublimation vapor deposition for the experiments. Dosing line sublimation vapor deposition of DBF in UHV at room temperature onto Ag(111) and Au(111) was successful. Ullmann dehalogenation occurred on both surfaces, forming organometallic bonds between ferrocene and silver adatoms on Ag(111). This work was unable to produce robust controllable molecular rotors using room temperature vapor deposition and Ullmann dehalogenation. However significant progress has been made into evaluating the issue present in, and methods for, achieving this goal. The XPS fits presented in this work are speculative based on the expected Ullmann dehalogenation process.

Following deposition onto Ag(111), DBF formed large (>40 nm) well-ordered structures of doubly dehalogenated dibromoferrocene ("ferrocene") molecules. XPS analysis showed that the initial deposition led to a single dehalogenation event with the second bromine cleaving off around 30-minutes later. The orientation of the adsorbed ferrocene was not well defined through STM and XPS because arguments can be made for both horizontally and vertically adsorbed ferrocene. NEXAFS resonance angle is indicative of a mix of vertical and horizontal adsorptions or a semi-vertical adsorption of ferrocene. The 30-minute period between dehalogenation events is possibly due to the high level of order in the formed structures, hindering the Ullmann dehalogenation reaction. There-in lies a possibility of vertical or semi-vertical ferrocene moieties if this single event can be isolated. Cooling the sample down may trap this structure leaving it unable to dehalogenate a second time.

While the molecular structures formed in this work are unusable as molecular rotors, they have potential use in spintronics materials. Their potential is due to the large well-ordered structures with minimal defects, that are required for stable wave propagation. A significant finding in the context of spintronics was that, fully dehalogenated DBF on Ag(111) at room temperature only forms one type of uniform structure following the 3 high-symmetry directions of the 111 plane. As previously mentioned, ferrocene has a strong spin coupling between the iron core and 36 electrons.

Further attempts to make a ferrocene based molecular rotor on Ag(111) could potentially be achieved through cold surface deposition. This is because the dibromoferrocene only singularly dehalogenates on adsorption, with the second halogen being cleaved off at least 30 minutes later. A chilled surface may stop the second dehalogenation reaction, or perhaps

repeating these experiments with other singularly halogenated ferrocenes may yield the desired result.

Deposition of DBF onto Au(111) resulted in the formation of triangular structures that were not explained with certainty in this work and require further study. XPS showed that there may only be a single dehalogenation of adsorbed DBF, however full dehalogenation of half of the adsorbed DBF would also produce similar XPS results. NEXAFS describes that the orientation of the adsorbed DBF is almost vertical. The molecule orientation and potential dehalogenation stage are promising results for future attempts at the production of surface bound ferrocene rotors on Au(111). The challenge of stabilisation is still an issue we were unable to address. However, it may be possible to stabilise the molecule with alternative functionalisation of ferrocene, or by cooling the sample down and paying special attention to the structural phases.

5.5 References

1   Lackinger, M. Surface-assisted Ullmann coupling. *Chem Commun (Camb)* **53**, 7872-7885, doi:10.1039/c7cc03402d (2017).

2   Horcas, I. *et al.* WSXM: a software for scanning probe microscopy and a tool for nanotechnology. *Rev Sci Instrum* **78**, 013705, doi:10.1063/1.2432410 (2007).

3   Schneider, C. A., Rasband, W. S. & Eliceiri, K. W. NIH Image to ImageJ: 25 years of image analysis. *Nat Methods* **9**, 671-675, doi:10.1038/nmeth.2089 (2012).

4   Gann, E., McNeill, C. R., Tadich, A., Cowie, B. C. & Thomsen, L. Quick AS NEXAFS Tool (QANT): a program for NEXAFS loading and analysis developed at the Australian Synchrotron. *J Synchrotron Radiat* **23**, 374-380, doi:10.1107/S1600577515018688 (2016).

5   Bjork, J., Hanke, F. & Stafstrom, S. Mechanisms of halogen-based covalent self-assembly on metal surfaces. *J Am Chem Soc* **135**, 5768-5775, doi:10.1021/ja400304b (2013).

6   Chua, C. K. & Pumera, M. Renewal of sp2 bonds in graphene oxides via dehydrobromination. *J Mater Chem* **22**, doi:10.1039/c2jm34358d (2012).

7   Tran, B. V., Pham, T. A., Grunst, M., Kivala, M. & Stohr, M. Surface-confined [2 + 2] cycloaddition towards one-dimensional polymers featuring cyclobutadiene units. *Nanoscale* **9**, 18305-18310, doi:10.1039/c7nr06187k (2017).

8   Strydom, C. A., Van Staden, J. F. & Strydom, H. J. An XPS investigation of silver bromide-coated ion-selective electrodes. *Electroanalysis* **3**, 815-821, doi:10.1002/elan.1140030815 (1991).

9   Grosvenor, A. P., Kobe, B. A., Biesinger, M. C. & McIntyre, N. S. Investigation of multiplet splitting of Fe 2p XPS spectra and bonding in iron compounds. *Surf Interface Anal* **36**, 1564-1574, doi:10.1002/sia.1984 (2004).

10   Ormaza, M. *et al.* Assembly of Ferrocene Molecules on Metal Surfaces Revisited. *J Phys Chem Lett* **6**, 395-400, doi:10.1021/jz5026118 (2015).

11   Berger, J. *et al.* Study of Ferrocene Dicarboxylic Acid on Substrates of Varying Chemical Activity. *J Phys Chem C* **120**, 21955-21961, doi:10.1021/acs.jpcc.6b05978 (2016).

12   Wasio, N. A. *et al.* Self-assembly of hydrogen-bonded two-dimensional quasicrystals. *Nature* **507**, 86-89, doi:10.1038/nature12993 (2014).

13   Cirera, B. *et al.* Efficient Lanthanide Catalyzed Debromination and Oligomeric Length-Controlled Ullmann Coupling of Aryl Halides. *J Phys Chem C* **121**, 8033-8041, doi:10.1021/acs.jpcc.7b02172 (2017).

14   Fan, Q. *et al.* Surface Adatom Mediated Structural Transformation in Bromoarene Monolayers: Precursor Phases in Surface Ullmann Reaction. *ACS Nano* **12**, 2267-2274, doi:10.1021/acsnano.7b06787 (2018).

15   Lovat, G. *et al.* Determination of the structure and geometry of N-heterocyclic carbenes on Au(111) using high-resolution spectroscopy. *Chem Sci* **10**, 930-935, doi:10.1039/c8sc03502d (2019).

16   Monig, H. *et al.* Understanding scanning tunneling microscopy contrast mechanisms on metal oxides: a case study. *ACS Nano* **7**, 10233-10244, doi:10.1021/nn4045358 (2013).

17   Eichhorn, J. *et al.* On-surface Ullmann polymerization via intermediate organometallic networks on Ag(111). *Chem Commun (Camb)* **50**, 7680-7682, doi:10.1039/c4cc02757d (2014).

18   Cao, C. Determination of Carbon 1s Core Ionization Energies in Saturated Molecules. *Mol. Inform.* **27**, 147-156, doi:10.1002/qsar.200610116 (2008).

19   Bagus, P. S. *et al.* Identification of transitions into Rydberg states in the X-ray absorption spectra of condensed long-chain alkanes. *Chem Phys Lett* **248**, 129-135, doi:10.1016/0009-2614(95)01315-6 (1996).

20   Otero, E. *et al.* Substituent effects in the iron 2p and carbon 1s edge near-edge X-ray absorption fine structure (NEXAFS) spectroscopy of ferrocene compounds. *J Phys Chem A* **112**, 624-634, doi:10.1021/jp074625w (2008).

21   Püttner, R. *et al.* The C 1s NEXAFS spectrum of benzene below threshold: Rydberg or valence character of the unoccupied σ-type orbitals. *Chem Phys Lett* **393**, 361-366, doi:10.1016/j.cplett.2004.06.053 (2004).

22   Lenhart, J. L. *et al.* X-ray absorption spectroscopy to probe surface composition and surface deprotection in photoresist films. *Langmuir* **21**, 4007-4015, doi:10.1021/la047160z (2005).

23   Heymann, K., Lehmann, J., Solomon, D., Schmidt, M. W. I. & Regier, T. C 1s K-edge near edge X-ray absorption fine structure (NEXAFS) spectroscopy for characterizing functional group chemistry of black carbon. *Org Geochem* **42**, 1055-1064, doi:10.1016/j.orggeochem.2011.06.021 (2011).

24   Stöhr, J. *NEXAFS Spectroscopy*. (1992).

25   Mishra, S. *et al.* Topological frustration induces unconventional magnetism in a nanographene. *Nat Nanotechnol* **15**, 22-28, doi:10.1038/s41565-019-0577-9 (2020).

Chapter 6: Research Conclusions

6.1 Conclusions

In this thesis, I have investigated the mapping of the rotational barriers of ferrocene and dibromoferrocene using DFT. Two maps were calculated with 3-21G and 6-31G(d,p) basis sets in Gaussian 09 using the B3LYP functional for both ferrocene and dibromoferrocene. The shape of the mapped potential for ferrocene matched with the expected isomer stable states. The ferrocene staggered state was the global minimum, and the eclipsed state was the global maximum for calculations with both basis sets. However, the resulting rotational barriers found using both basis sets were less than the published value for ferrocene's rotational barrier. This was not entirely explained but was assumed to be due to ferrocenes uniquely stable organometallic structure.

While the shape of the mapped rotational potential barrier for ferrocene was unsurprising, the shape of the potential for dibromoferrocene was surprising. The lowest energy position was found in the symmetrically eclipsed conformation as opposed to expectation of being most stable with the two bromines positioned diametrically opposite to one another. Increasing basis set appeared to make the result more accurate and pull out two more large minima in the potential map.

The DFT of Ag(111) surface adsorbed ferrocene interestingly shows that there is little energetic difference between horizontally adsorbed and vertically adsorbed ferrocene, therefore vertically adsorbed ferrocene would likely remain vertical. The adsorbed ferrocene formed 3 geometrically identical adsorption geometries on Ag(111). No further insight about the adsorption geometry or energetics of ferrocene on surface were gained from these optimisations.

More DFT calculations for potential barrier and surface geometry optimisations, with varied initial position and functionalisation are highly desirable. These should include the calculation of a singularly dehalogenated DBF (BF) rotational barrier and the surface adsorption geometries of Fc, DBF and BF on Au(111) and Ag(111). These DFT calculations were originally intended but ultimately set aside, due to time constraints, as aims for future works.

I have investigated the potential of dibromoferrocene Ullmann dehalogenation on Ag(111) and Au(111) substrates for the formation of surface confined nanorotors. Dibromoferrocene

was successfully deposited via vapor deposition at room temperature under UHV conditions and dehalogenated on initial contact with Ag(111). Approximately 30 minutes later bromoferrocene dehalogenated a second time forming large (>40 nm) well-ordered corn-rows of ferrocene, aligning with the three high-symmetry directions of Ag(111), observed in STM images. The ferrocene in these structures were found to be either a mix of vertically and horizontally adsorbed or semi-vertically adsorbed molecule confirmed by NEXAFS analysis.

These structures of ferrocene could have the potential for use in spintronics as they are large and well-ordered, and ferrocene has strong spin interactions ideal for spin wave propagation.

Unfortunately this means I was unable to achieve the formation of vertically oriented ferrocene organometallic-oligomers on Ag(111). However, the 30 minutes between bromoferrocene dehalogenation into ferrocene structures may provide an opportunity to form vertical structures if the surface is cooled down. The orientation in the surface plane for individual molecules is still yet to be determined as this issue appeared more challenging than expected. Steric hinderance and π-π stacking are thought to play a role in the ordering and the structures are identical in the three [111] high-symmetry directions, the same as what was observed in the surface adsorption DFT. However, there is still considerable ambiguity in interpretation of the observed structures.

Some dibromoferrocene dehalogenates on Au(111) based on XPS but only a relatively small quantity. A majority of adsorbed dibromoferrocene remained halogenated and over time desorbed from the surface leaving behind a mix of singularly and doubly dehalogenated dibromoferrocene. NEXAFS describes the majority of adsorbed molecule to be vertically oriented suggesting future potential for surface confined rotors. STM images were exceptionally hard to produce and made harder by the relatively small amount of adsorbed molecule that desorbed relatively quickly. STM and XPS confirmed that incident x-rays significantly increase desorption speed of the molecule therefore most images were produced immediately after deposition. While molecular resolution STM images were not produced, there were two distinct forms of artefact that dibromoferrocene seems to produce. The first are lines of connected triangles with vertices that appear as indents but may appear different under other tunnelling parameters. The second are triangular indents in various sizes that form fractal-like patterns with vertices containing protrusions. Due to the difficulty of STM imaging DBF on Au(111) the structure of ferrocene moieties on the surface is unknown and needs further measurement and imagery.

6.2 Outlook

There are many questions left to answer that were not covered in this work, as the focus was on the vertical orientation of the ferrocene moiety, rotational barrier, and Ullmann dehalogenation process. Such questions include: What is the adsorption geometry of the ferrocene moiety on Ag(111) and Au(111) surfaces? Can we determine the assembly process

and the effect of chilling after deposition on Ag(111)? Can similar structures be formed using a different halogen to functionalise ferrocene? What would the deposition of extra metallic atoms onto these structures look like? Can we gather molecular resolution imagery following deposition on Au(111)? Why is ferrocene causing these triangular depressions if ferrocene is indeed the cause? If vertical surface-confined ferrocene is achieved, then what effect does that have on the rotational barrier, considering that bromines had such a significant effect? These are significant questions for the focus of future work. The structures formed from dibromoferrocene on Ag(111) are large and uniform with a small amount of defects no more than a couple of atoms in size. With ferrocene's strong and multiple electron interactions with the iron core and ferrocene being JTE inactive, the structures formed on Ag(111) from the work done in this thesis should be desirable for spintronics applications. These questions and potential applications are interesting pathways for the focus of future research.